2013

Earth occultation imaging of the low energy gamma-ray sky with the Fermi/Gamma-ray Burst Monitor

James Craig Rodi
Louisiana State University and Agricultural and Mechanical College

EARTH OCCULTATION IMAGING OF THE LOW ENERGY GAMMA-RAY SKY WITH THE *FERMI*/GAMMA-RAY BURST MONITOR

A Dissertation

Submitted to the Graduate Faculty of the
Louisiana State University and
Agricultural and Mechanical College
in partial fulfillment of the
requirements for the degree of
Doctor of Philosophy
in
The Department of Physics & Astronomy

by
James Rodi
B.S., Louisiana State University, 2006
May 2013

To RnR

Acknowledgments

Firstly, I'd like to thanks my parents, Ron and Renee, and my brother, Matthew, for their love and support during my life and especially during my time in graduate school. Without them, this wouldn't have been possible. I also want to thank my grandparents, James and Margaret Mohr, for their constant encouragement; hopefully this dissertation answers all of your questions about my research. To my fellow graduate students, I appreciate your friendship and camaraderie as we worked seemingly endless homework assignments. To my fellow lab mates, from Chris and Chrissie Welch, who taught me that work be could be fun, to Brent Budden and Yuan Zhang, who helped me through research difficulties, "Thank you." I would be remiss if I didn't thank Gary Case for tolerating my frequent questions as well as his guidance and instruction during my time at LSU. And I would like to thank Ashley Pagnotta for her help in preparing me for my defense.

Also, I have to thank my friends for their countless contributions to my life during this time: to Hillary Addison Duncan, Parker Maness, and Caitlin Craig for pulling me out of the water that day in August; to Arrielle Opotowsky for being the reason why my research took so long to complete; to Adam Kealoha Causey for his personal guidance and friendship; to Adam and Bryan Gerace, Anthony Zehyoue, Jonathan Causey, Josh Johnson, and Ryan Harris for your constant friendship and silliness; to Timothy and Christopher Kwan and Chris Edwards for helping me have a modicum of a social life and meeting people I otherwise would have never know; and to Kimberly Simone Kwan for encouraging me to stay fit by reminding me of my "husky"-ness.

And, of course, I want to thank my advisor, Michael Cherry for allowing me to be a part of his research group during my time at LSU and for his patience during my never-ending questions and interruptions.

This work has been supported by the NASA Fermi Guest Investigator program, NASA/Louisiana Board of Regents Cooperative Agreement NNX07AT62A (LSU), the Louisiana Board of Regents Graduate Fellowship Program, and the LONI Graduate Fellowship Program. This material is based upon work supported by HPC@LSU computing resources as well as the Louisiana Optical Network Institute (LONI).

Table of Contents

List of Tables

List of Figures

Abstract

The hard X-ray/soft γ-ray sky is highly variable as source intensities can vary on timescales from fractions of a second to years. The type of sources emitting at these energies often include compact objects such as white dwarfs, neutron stars, and black holes interacting with the surrounding environment, which enables the study of the properties and characteristics of these exotic objects. Because the interactions with the environment is often through accretion, most of the emission is in X-rays and γ-rays (Frank, King, & Raine, 1992) making this energy range critical to understanding the relevant physical processes and mechanisms.

Hard X-ray/soft γ-ray (10 keV - 1 MeV) photons are difficult to focus requiring alternative observing techniques to monitor sources in this energy range. One method is the Earth Occultation Technique (EOT) that uses the rapid change in count rate ($\sim$ 10 sec) due to a source passing behind (or out from behind) the Earth to measure source intensity. The EOT has been applied to the Gamma-ray Burst Monitor (GBM) on board the NASA *Fermi* satellite since its launch in 2008 and has been performing all-sky monitoring of a predetermined catalog of $\sim$ 200 hard X-ray/soft γ-ray sources.

Because the EOT requires prior knowledge of a source's position for monitoring, I have developed a tomographic imaging method Imaging with a Differential filter using the Earth Occultation Method (IDEOM) to generate all-sky images in search of sources absent from the input catalog to construct a catalog as complete as possible. A complete catalog is important for reducing a source of systematic error as the flux from an unaccounted-for source can be attributed to a known source thus biasing its flux measurement. Approximately 4 years of

GBM data have been analyzed to produce all-sky images covering the 12-50 keV, 50-100 keV, and 100-300 keV energy bands with 16 sources being added to the GBM catalog. All-sky images are shown for each energy range along with a table listing the sources detected by IDEOM. Also, the list of sources detected by IDEOM has been compared to those detected by EOT in each energy band.

In addition, spectral analysis was performed in the four persistent sources detected by GBM and the *Fermi*/Large Area Telescope (LAT) (NGC 1275, 3C 273, Cen A, and the Crab) thus providing energy coverage from $\sim$ 10 keV to $\sim$ 100 GeV to study the high energy emission processes of these sources. Spectral results from GBM and LAT are presented and shown to be in agreement with previously proposed models in the literature.

Finally, I have also developed a transient search algorithm to search for flares and outbursts in the light curves of GBM sources. This algorithm was applied to the $\sim$ 200 sources in the GBM catalog to search for transient events during the first four years of the mission in four energy bands covering 12-500 keV. The search resulted in 168 transient events found from 65 sources with 7 events detected above 50 keV and 1 event detected above 100 keV (XTE J1752-223). A table of start and stop times are listed for each event and energy band, and example light curves are shown for GK Per, GX 339-4, and XTE J1752-223.

Chapter 1
Introduction

1.1 Scientific Motivation

Some of the most dynamic astrophysical systems are strong emitters at hard X-ray/soft γ-ray energies. These sources include accreting binaries and active galactic nuclei (AGN). Thus observing in the keV to MeV range is critical to understanding the physical processes at work (Frank, King, & Raine, 1992). Black hole binaries (BHBs) have been observed in three distinct spectral states while in outburst: the thermal state, the hard state, and the steep power law state. In a thermal state, the spectrum is dominated by a thermal component due to a hot inner accretion disk with a characteristic temperature of ~ 1 keV and a weak nonthermal component. The hard state can often be fit to a relatively flat power law model and an exponential cutoff with little contribution from a thermal component. The emission is predominately due to inverse Compton scattering with questions concerning the physical processes involved as well as the connection between the accretion disk and the radio jets that are often observed (Cadolle Bel et al., 2011). The steep power law state consists of a strong thermal component and a strong power law component, often extending above 1 MeV (Remillard & McClintock, 2006).

With high sensitivity and time resolution, the *Rossi X-ray Timing Explorer* (*RXTE*) was able to make significant progress in the characterization of BHB states and the understanding of the thermal state. But significant features in the hard state and the steep power law state extend beyond the *RXTE* upper energy limit near ~ 200 keV, and require an instrument

with good sensitivity past 200 keV in order to understand the physical mechanisms at work as well as distinguish between source models.

When the compact object in the binary system is a neutron star (NS), the interaction between the accretion disk and the compact object exhibit different behavior than BHBs. The magnitude of the magnetic field of the NS also has an impact on the production of X-rays. Thus such systems can be broadly grouped as accreting NS (weak magnetic field) and accreting pulsars (strong magnetic field). Accreting NS are characterized by thermonuclear bursts called Type I bursts that usually last on the order of seconds to minutes and are followed by emission powered by accretion which lasts for hours or days (Linares et al., 2012). As more instruments with larger fields of view have been launched (e.g. *RXTE*/ASM, *Swift*/BAT, *CGRO*/BAT, *Fermi*/GBM), more complete monitoring of these systems has been made. These observations have shown the existence of two other types of Type I bursts: "long" bursts ($\sim$ 10 mins) and "superbursts" ($\sim$ hrs to $\sim$ days). These newly observed types have led to questions about their relation to the normal short bursts.

Also, improved instrument capabilities have revealed the presence of millisecond oscillations from sources during most Type I bursts. By observing burst oscillations, one can measure the NS spin in order to do a population study as part of different NS classes (Watts, 2012). Spin measurements can also help determine the maximum possible spin rate for a NS which can help determine the equation of state of NS.

The large field of view and long mission lifetime of *CGRO*/BATSE have proven instrumental in the understanding of accreting pulsars. Previous missions were unable to provide the long baseline of observations that BATSE (1991-2000) provided. This coverage enables the study of the long-term spin evolution and has revealed that torque transitions between spin-up and spin-down are not unusual (Bildsten et al., 1997). Accreting pulsars exhibit pulsed emission as material is funneled in the magnetic poles due to a strong magnetic field causing "hot spots". For persistent sources this behavior allows for accurate timing and measurement of orbital parameters as well as studying the behavior of the accreting mate-

rial in the presence of a strong magnetic field. Like with accreting NS, measuring the spin rate in these systems gives insight for population studies and for studying the evolution of NS binary systems (Bildsten et al., 1997).

AGN are powered by matter accreting onto a supermassive black hole, likely from an accretion disk plus a wind (Ulrich, Maraschi, & Urry, 1997). While there are multiple classes of AGN, it has been proposed that the differences are due to the orientation of the AGN with respect to the observer. Quasars and Seyfert 1 galaxies are viewed with the disk face on; Seyfert 2 galaxies are seen edge on through the disk; and BL Lac galaxies are viewed down the AGN jet (Schönfelder, 1994). Hard X-ray/soft γ-ray observations of AGN avoid the heavy absorption that makes studying these sources difficult at other wavelengths (Tueller et al., 2008). Thus monitoring at these energies presents the opportunity to perform an unbiased search for these sources, especially highly obscured Seyfert 2 galaxies (Grindlay et al., 1998), as proposed with the EXIST mission to develop a luminosity function. Also monitoring AGN variability and the corresponding spectra can result in constraints on models of the emission mechanisms at work. Coordinating multiwavelength observations allows searches for correlation across bands giving information about the environment near the black hole (Parsons et al., 1998).

After BATSE's success monitoring in the hard X-rays and soft γ-rays using the Earth Occultation Technique (EOT), GBM was developed as an instrument on board the *Fermi* satellite. GBM has a large field of view that enables monitoring of numerous sources on a daily basis to look for long-term variability from sources, such as accreting pulsars, and to search for the quick rise and rapid variations of transient events like those from BHBs and AGN flares. GBM also covers a broad energy range (8 keV to $\sim$ 40 MeV). GBM is currently the only wide field-of-view X-ray mission able to observe at energies above $\sim$ 200 keV. This allows GBM to study BHBs in the hard state and steep power law state to better understand the physical processes at work. Also simultaneous observations of AGN across a range of wavelengths are possible to look for correlations.

The EOT has been applied to GBM since launch in 2008 and has produced a number of noteworthy results during the first four years of the mission. One such result is the public availability of the daily lightcurves of the ~ 200 sources in the GBM source catalog. These data are posted online[1] for use by the scientific community. Another important product of this analysis is a published catalog of high energy (> 100 keV) sources (Case et al., 2011). This work presents the eight GBM sources detected with a significance greater than 7σ after two years of observations. Six of the sources are persistent sources: the Crab, Cyg X-1, SWIFT J1735.5-0127, 1E 1740-29, Cen A, and GRS 1915+105. Two of them are transient sources: XTE J1752-223 and GX 339-4. Also, the Crab and Cyg X-1 were significantly detected about 300 keV.

A catalog of results from the first three years of occultation analysis has been published (Wilson-Hodge et al., 2012). Through three years, GBM significantly detected 99 sources. Nine of these were detected above 100 keV, with GRS 1758-258 as the additional source not in the high energy catalog paper. In the Wilson-Hodge et al. (2012) paper, fluxes and errors for 209 sources and source coordinates are reported in four broad energy bands (12-25, 25-50, 50-100, and 100-300 keV) as well as the 12-50 keV significance and the 12-300 keV significance.

The most important result to date was the detected variability of the Crab in the 15-100 keV energy range (Wilson-Hodge et al., 2011). The flux from this source was long thought to be constant in the hard X-ray/soft γ-ray regime. Consequently it could be used as a calibration source (e.g. Kirsch et al. 2005; Jourdain & Roques 2009; Weisskopf et al. 2010; Meyer et al. 2010). Wilson-Hodge et al. (2011) demonstrated correlated variability between *Fermi*/GBM, *Swift*/BAT, *RXTE*/PCA, *INTEGRAL*/ISGRI, and *INTEGRAL*/JEM-X2 over the lifetime of GBM, with a 7% decline in the 15-50 keV band over the first ~ 1 year of the GBM mission. The pulsed flux measured by PCA is consistent with the predicted pulsar spin-down flux and thus is not responsible for the flux variability. Consequently the

[1]http://heastro.phys.lsu.edu

variation is due to changes in either the magnetic field strength or relativistic electron density in the nebula.

1.2 Plan of the Dissertation

The motivation of this dissertation is to demonstrate that the Earth Occultation Technique (EOT) with GBM is a viable method for monitoring a predetermined catalog of sources of hard X-rays and soft γ-rays, and this method can benefit from an imaging technique that can generate all-sky images to search for additional sources. This added capability allows GBM to search for transients as well as faint sources absent from the standard predetermined source catalog. The importance of finding and monitoring transient sources has been described above. The need to construct a source catalog that is as complete as possible is necessary in measuring accurate source fluxes and to reduce a source of systematic error in the EOT method. The ability to image the sky at high energies (> 100 keV) presents the opportunity to investigate a potential cause of the discrepancies between the Marshall Space Flight Center (MSFC) (Harmon et al., 2004) and Jet Propulsion Laboratory (JPL) (Ling et al., 2000) analyses of BATSE occultation data.

In Chap. 2 the Earth Occultation Technique (EOT) will be presented along with a history of past occultation observations, including lunar occultations and use of EOT with the BATSE experiment. A description of the *Fermi* satellite and the GBM instrument will also be included. Chap. 3 explores imaging with Earth occultations and discusses previous work done in this area. Also, the imaging algorithm that has been developed for GBM, Imaging with a Differential filter using the Earth Occultation Method (IDEOM), will be described that allows for performing blind searches for source sources. The results of analysis with IDEOM applied to ~ 4 years of GBM data in three energy ranges (12-50 keV, 50-100 keV, and 100-300 keV) will be presented and discussed in Chap. 4. Chap. 5 covers the analysis of those sources significantly detected by both GBM and the *Fermi*/LAT. Chap. 6 presents a

flare search algorithm developed for analysis of GBM occultation data to search for transient events from sources in the GBM catalog, and Chap. 7 discusses results from analysis with IDEOM, spectra of sources detected by GBM and LAT, and flares found by the flare search algorithm.

Chapter 2
GBM and the Earth Occultation Technique

2.1 History of Occultation Measurement

The use of occultation with celestial bodies to measure the X-ray flux from astrophysical sources is not a new technique. Occultation techniques work by comparing the count rate from a location on the sky due to the source and the background shortly before the source goes into occultation to the count rate after occultation. Because the transition from full transmission to full attenuation is fast, the change in count rate results in a step-like feature in the count rate data. After the occultation step, the count rate is due to the background. The amplitude of the step above the background is a measure of the source intensity at the time of the occultation.

The first use of occultation in X-rays was by Bowyer et al. (1964) using lunar occultation to measure the Crab nebula. This experiment involved a rocket launch timed to observe the Crab while the central region of the nebula went into occultation. The goal of the mission was to search for a point source at the center of the nebula or an extended source, with a point source expected to be a neutron star. A similar experiment was conducted by Palmieri et al. (1975) with the intent to measure the X-ray size of the Crab nebula and its brightness variability. Also, the position of the low mass X-ray binary GX 9+1 was measured using lunar occultation with the *Copernicus* satellite (Davison & Morrison, 1977), and a motivation

for the 90 hour orbit of the *EXOSAT* mission was to increase the number of observable lunar occultations (White & Peacock, 1988).

During the development of the Burst and Transient Source Experiment (BATSE), Fishman et al. (1984) proposed that Earth occultations could also be used to monitor point sources. By using the Earth, more of the sky is occulted allowing for more sources to be observed than is possible with the moon. Two independent methods were developed to analyze BATSE occultation data: the Earth Occultation Technique (EOT) at MSFC (Harmon et al., 2002, 2004) and the Enhanced BATSE Occultation Package (EBOP) at JPL (Ling et al., 2000). Both approaches used a predetermined catalog of sources to calculate occultation times. The EOT fit a 4-minute window of count rate data to a quadratic background plus an occultation step model for each source that occults during that period, while EBOP fit all the data for a day at once using a semi-physical background model. The EBOP background model is calculated from a complex multi-component model in order to account for such contributions as the local position in low Earth orbit and cosmic-ray interaction with the satellite (Ling et al., 2000). The expectation of the EBOP approach was that greater sensitivity could be achieved than was possible with the EOT.

These differing methods resulted in significant differences in flux measurements for some sources, especially above 100 keV (Harmon et al., 2004). In addition, the high energy flux observed from some sources (e.g. Cyg X-1 and GRS 1915+105) is dependent on the orbital phase of the satellite. A possible cause of such variability could be high energy sources not included in the source catalog. Generating images in the 100-300 keV energy range presents an opportunity to test this hypothesis by searching for unaccounted-for high-energy sources. If no additional sources are detected, that suggests the discrepancies are likely not due to unaccounted-for sources. A more likely cause in that case is inaccuracies in the EBOP background model.

2.2 The Gamma-ray Burst Monitor

The Gamma-ray Burst Monitor (GBM) is one of two instruments on board NASA's *Fermi* satellite, which was launched in June 2008 to an orbit of 555 km with an orbital inclination of 25.6° (Wilson-Hodge et al., 2012). The other instrument is the Large Area Telescope (LAT), which covers energies from 20 MeV to 300 GeV (Atwood et al., 2009). GBM is comprised of 12 Sodium Iodide (NaI) detectors with 12.7 cm diameter and 1.27 cm thickness and two Bismuth Germanate (BGO) detectors with 12.7 cm diameter and 12.7 cm thickness. The NaI detectors cover energies from 8 keV to 1 MeV, and the BGO detectors cover $\sim$ 200 keV to $\sim$ 40 MeV. The 12 NaI detectors are arranged on the corners of the spacecraft with six pointing perpendicular to the z-axis, four pointing at 45° from the $+z$-axis, and two pointing at 20° from the $+z$-axis. The BGO detectors are located on opposite sides of the spacecraft. None of the detectors have direct imaging capabilities. GBM has two data types, CTIME and CSPEC. The CTIME data have 0.256-sec time resolution and 8 broad energy channels, while CSPEC has 4.096-sec time resolution and 128 narrow energy channels. All of the work done in this dissertation uses CTIME data.

At *Fermi*'s altitude, Earth's diameter is $\sim$ 140°. Thus $\sim$ 30% of the sky is blocked by the Earth at any given time. Over 85% of the sky is occulted by the Earth over the course of a single orbit, and the entire sky is occulted in $\sim$ 26 days (half of the *Fermi* orbital precession period), though the exposure is not uniform.

Fermi operates in a scanning mode by pointing 35° north of the zenith for one orbit and then pointing 35° south of the zenith for the next orbit. In October of 2009, the rocking angle was changed to 50°. The spacecraft also rolls about the z-axis to keep the solar panels facing the Sun. *Fermi* also occasionally enters a pointed mode.

2.3 Earth Occultation with GBM

As stated earlier, Earth occultation uses the step-like features in count rate data due to a source passing behind (or out from behind) the Earth to measure the flux from the source. This gives two occultation measurements per orbit and ~ 30 measurements per day for a satellite in low Earth orbit. Occultation times can be predicted using the position of the source, the position history of the satellite, and an accurate model of the Earth that accounts for the oblateness. The occultation time has been defined to be when the transmission through the atmosphere for a 100 keV photon is 50%. The transmission through the Earth's atmosphere is modeled by

$$T(E_{\rm ph}, t) = \exp[-\mu(E_{\rm ph})A(h(t))], \tag{2.1}$$

where $\mu(E_{\rm ph})$ is the mass attenuation of γ-rays of energy $E_{\rm ph}$ in air (NIST, 1989) and $A(h(t))$ is the air mass along a line of sight for an altitude $h(t)$ using the U.S. Standard Atmosphere (1976). Atmospheric variations were shown to have negligible effects in daily flux measurements of the Crab and thus have been ignored in this transmission model (Wilson-Hodge et al., 2012). Fig. 2.1 shows an occultation step of Sco X-1 in the 12-25 keV band from April 29, 2012 as an example occultation step.

The EOT as used by MSFC has been implemented with GBM. This method was selected instead of EBOP because of the difference between pointing schemes between *CGRO* and *Fermi*. *CGRO* maintained fixed pointing for extended periods of time (days to weeks), which allowed the detector response for a location on the sky to remain fixed. This simplified EBOP's calculations when fitting all the data for a single day at once. *Fermi* scans the sky with rapid slewing after every orbit, leading to large changes in detector response making the EBOP approach much more difficult to implement. The EOT fit significantly shorter time intervals (4 minutes) making a change in response easier to take into account. Also,

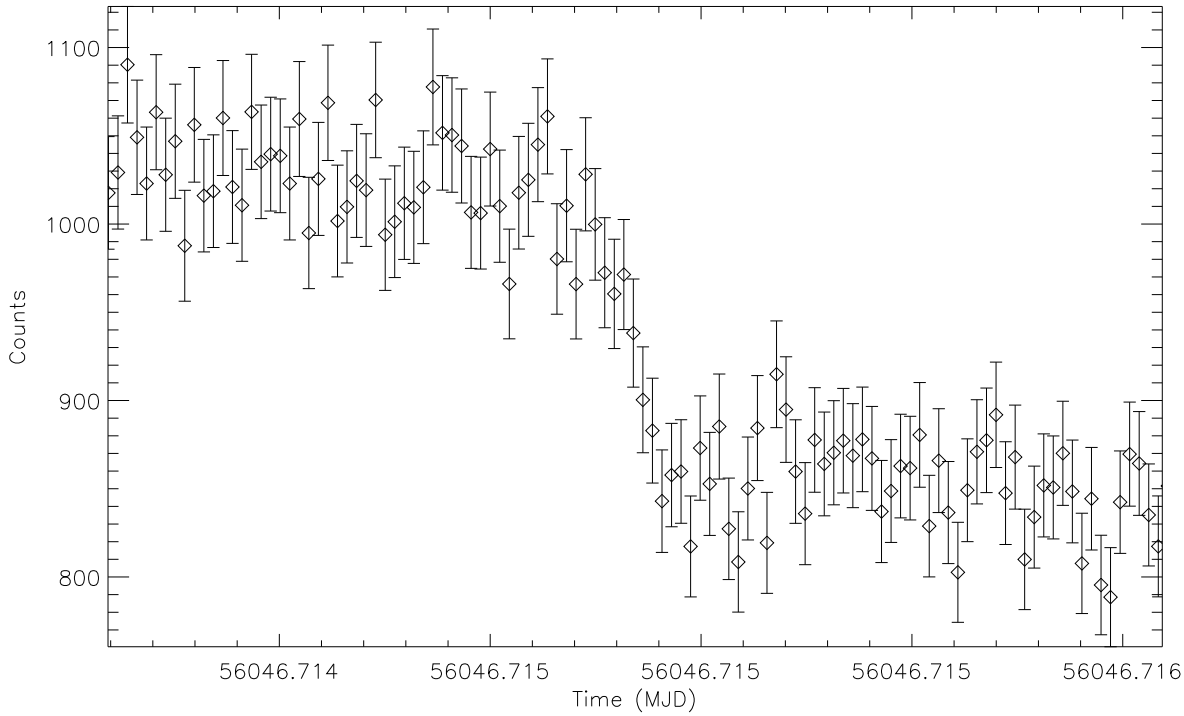

Figure 2.1: Example Occultation Step of Sco X-1 in 12-25 keV Energy Band

EBOP observed high-energy fluxes from faint sources that Ling et al. (2000) cautioned may be attributed to systematic effects as well as showing discrepancies between *CGRO*/OSSE above 200 keV for GX 339-4 (Ling et al., 2000).

2.3.1 Step Fitting

In the EOT, an occultation window model is fit to a 4-minute window of count rate data with the window centered on the occultation time of the source of interest. The model is composed of a quadratic background model plus source models for each source that occults during that time period. Typically the background is smooth and slowly varying and thus is well fit to a quadratic polynomial. A source model consists of an assumed source spectrum

combined with an atmospheric transmission model given by Eqn. 2.1 that is convolved with the time-dependent detector response. A scale factor is calculated for each detector that views the source of interest within 60° of the detector normal for each energy band by fitting the occultation window model to the data. The weighted average of the scale factors for the source of interest is calculated for each energy band and then multiplied by the predicted flux to determine the measured flux.

In practice, not all occulting sources are fit in an occultation window. Faint persistent sources ($<$ 50 mCrab) and inactive transient sources are included in fits only when they are the source of interest. For persistent sources, a source classification system has been developed based on the average flux in the 12-50 keV energy band. Class 1 sources are $>$ 500 mCrab, class 2 sources are between 150 and 500 mCrab, class 3 sources are between 50 and 150 mCrab, and class 4 sources are $<$ 50 mCrab. Sources class 3 and higher are included in fits when not the source of interest, or as "interfering sources." These classifications are also used to determine how far away from the detector normal a source will be included as an interfering source. Class 1 are included out to 90°, class 2 out to 60°, and class 3 out to 40°. For transient sources, a flare database has been compiled using public *Swift*/BAT data to denote times when a source is flaring. A similar classification is used to mark the appropriate class with the same flux intervals used as for persistent sources.

At energies below 50 keV, the Sun can also act as an interfering source during solar flares. A solar flare database has been compiled based on *Geostationary Operational Environmental Satellite* (*GOES*) data from the National Oceanic and Atmospheric Administration (NOAA) Space Weather Prediction Center. Classifications for the solar flare database are based on the peak flux detected by *GOES* during that time period. Class M flares and class X flares are included out to 90°, class C flares out to 60°, and class B flares to 40°. Data with class M and class X flares are often filtered out of the good time intervals (GTIs) before step fitting occurs. Thus only class C and class B flares are included as interfering steps.

2.3.2 Systematic Errors

Six systematic effects have been seen to affect the EOT flux measurements with GBM: 1) the accuracy of the assumed source spectrum, 2) large variations in the background during the occultation window, 3) duration of the occultation transition, 4) inaccuracies in the detector response matrices, 5) occultation limb geometry, and 6) nearby sources. This section explains these effects and how they are mitigated, accounted for, or quantified.

Assumed Source Spectrum

An important part of the source model used in deriving the source flux is the assumed source spectrum. The effects of selecting an incorrect source model were studied by calculating the source fluxes due to incorrect models compared to the correct model. Five source models were used with the Crab. The models were: 1) the canonical Crab spectrum with a power law of $\Gamma = 2.1$ (Toor & Seward, 1974), 2) an exponential cutoff spectrum with a cut-off energy of 30 keV and an e-folding energy of 13.6 keV, 3) an exponential cut-off spectrum plus a 1 mCrab power law with $\Gamma = 2$, 4) a power law spectrum with $\Gamma = 3$ and 5) a hard power law spectrum with $\Gamma = 1$. Using these models for the Crab, the measured count rates from the occultation steps were found to be consistent within the errors; thus the measured count rate is not heavily dependent on the assumed source spectrum. The statistical significance of the average flux in each energy band was found to be consistent among the source models as well.

Flux values between the different models did show some systematic effects though. Models 3 and 4 were consistent with the canonical Crab spectrum to within 5-10%. Models 2 and 5, on the other hand, showed large flux differences from the canonical Crab model. This test was repeated for Vela X-1 using models 2-5. The results were similar to those for the Crab with the measured count rates and significances being consistent, and large flux deviations depending on the model. Fluxes from models 3 and 4 were consistent with model 2, which

is based on BATSE results from Bildsten et al. (1997). Model 5 showed large flux deviations as with the Crab. Thus the measured count rate and significance are not strongly dependent on the assumed source spectrum, but the measured flux values can be largely affected by the assumed source spectrum. In order to have the most accurate flux values, a literature search was performed to find relevant models for each source in the GBM input catalog. For sources where a model was not found in the GBM energy range, model 4 (power law spectrum with $\Gamma = 3$) was used as that model was able to approximate a hard source spectrum like the Crab and a soft spectrum like Vela X-1.

Background Variations

Occultation window models fit the background simultaneously with the source models. Thus if the background is not adequately fit by a quadratic function, the background is absorbed by the source terms effecting the flux measurements. Outlying flux measurements in the 12-25 keV band for multiple sources were often seen to correspond to times of large variations in the background due to South Atlantic Anomaly (SAA) entrance or exit, bright solar flares, or rapid slews by *Fermi*. Fig. 2.2 shows an example of a SAA pass in the 12-25 keV band. While this effect does not occur in every detector or every SAA pass, the measured flux during such an event is heavily biased by the increased background. Effects from SAA passes and bright solar flares have been mitigated by filtering the 12-25 keV count rate data: the count rate data are fit with a spline function model and times of large variations from the model have been removed from the GTIs and thus excluded from occultation window fits.

The spin rate of *Fermi* is given by

$$(wsj_1^2 + wsj_2^2 + wsj_3^2)^{1/2}, \tag{2.2}$$

where wsj_i are the instantaneous angular velocity components of the spacecraft around three

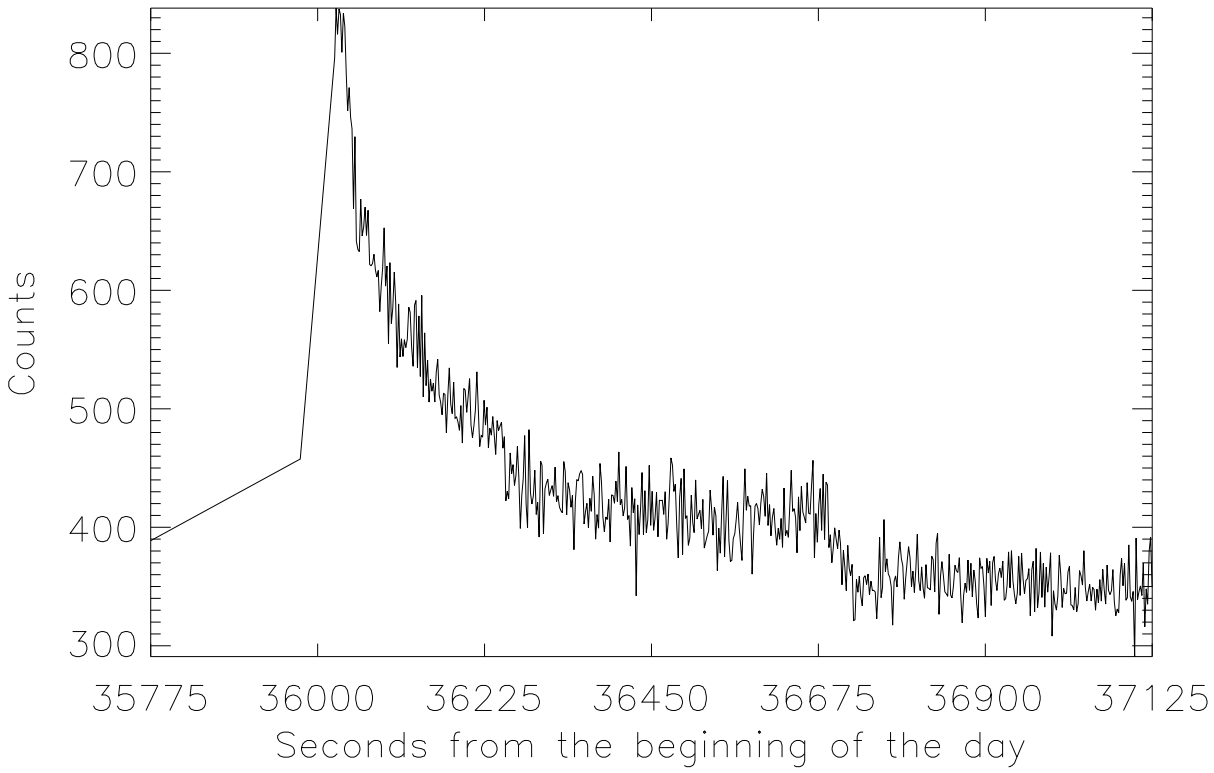

Figure 2.2: Example of a Pass through the South Atlantic Anomaly

axes. Times of high spin rate, or rapid slews, often result in a quick changing background during the fit window, which is not well fit by the quadratic background model. Occultation windows with spin rates $> 4 \times 10^{-3}$ rad/s have been flagged and removed from further analysis.

Occultation Transition Duration

Because of the Earth's atmosphere, an occultation step has a finite duration. The duration of a step depends on the satellite orbital period and the angle between the source and the orbital plane of the satellite, β, such that

$$\Delta t \approx (\frac{P_{orb}}{2\pi})(\frac{\Delta h}{r_{sc}\cos(\theta_{occ})})(\frac{\sin(\theta_{occ})}{\sqrt{\cos^2(\beta) - \cos^2(\theta_{occ})}}), \tag{2.3}$$

where P_{orb} is the orbital period of the satellite, Δh is the altitude difference between 90% transmission and 10% transmission, r_{sc} is the distance of the spacecraft from the center of the Earth, and θ_{occ} is the angle between the source and the spacecraft at the time of the occultation (Harmon et al., 2002). The angle θ_{occ} is defined to be

$$\theta_{occ} = \sin^{-1}(\frac{r_E + h_{occ}}{r_{sc}}), \tag{2.4}$$

where r_E is the radius of the Earth and h_{occ} is the height above the atmosphere corresponding to 50% transmission. For GBM $r_{sc} = 7433.1$ km, $h_{occ} = 70$ km, and $r_E = 6878.1$ km, resulting in $\theta_{occ} = 69.2°$. Using this value of θ_{occ} with $P_{orb} = 96$ min, and $\Delta h = 25$ km, results in

$$\Delta t \approx \frac{8.1}{\sqrt{cos^2(\beta) - 0.126}} \text{ s} \sim \frac{8}{\cos\beta} \text{ s}. \tag{2.5}$$

GBM analysis has shown that flux measurements for occultation steps lasting longer than 20 sec are often inaccurate as the occultation duration begins to last on the order of background variations and thus have been excluded from analysis.

Detector Response Matrices

Results from the *Fermi* source survey were shown to agree with mass model simulations to $< 5\%$ rms for detectors for source angles $< 90°$ (Meegan et al., 2009). This confirms that the detector response matricies for large structures of the spacecraft are accurate. There are smaller scale structures though that were not adaquetly taken into account in the detector response. The most obvious being the solar panels. The mass model for *Fermi* that was used to generate the detector responses included the solar panels in a fixed orientation, but the orientation of the solar panels are not fixed, which can lead to unexpected source occultations. These steps are particularly noticable at low energies. To account for solar panel blockages, blockage regions have been defined in spacecraft coordinates so that if an interfering source or the source of interest passes into that region that detector is removed

from the occultation fit. Also, two small regions have been defined as blockage regions for NaI 11 due to some small structures other than solar panels.

Occultation Limb Geometry

The *Fermi* satellite orbital precession period is ~ 53 days, meaning that the Earth occultation limb geometry (i.e. the projection of the Earth's limb on the sky) repeats at this period. For a given geometry, the EOT flux measurement may be inaccurate due to unmodeled sources or extended sources. Known unmodeled point sources have been mitigated in a couple of ways. *Swift*/BAT data has been used to create a flare database of times and intensities for transient sources. Newly discovered sources are added when needed. Also an imaging method Imaging with a Differential filter using the Earth Occultation Method (IDEOM) (Rodi et al., 2011) has been developed to search for unmodeled sources. So far 16 sources with statistical significance $> 10\sigma$ have been added to the GBM catalog through this method. More discussion of IDEOM can be found in Sec. 3.3

Nearby Sources

Nearby sources can often complicate Earth occultation measurements if they occult close in time to the source of interest. Sources not nearby on the sky can occult close in time as well, though this occurs less frequently during the course of an orbital precession period. When two sources occult within 8 s of each other, the occultation fitting is unable to appropriately assign fluxes to the sources. Thus when the source of interest was involved, the flux measurements have been flagged and removed from further analysis. The angular resolution of occultation techniques is approximately $360^\circ \times \frac{\Delta t}{P}$, where Δt is the occultation transition duration and P is the orbital period of the satellite. As stated earlier, for Earth occultation $\Delta t \sim 8/\cos\beta$ and $P \sim 96$ mins for *Fermi*. Consequently the angular resolution ranges from $\sim 0.5^\circ$ at $\beta = 0$ to $\sim 1.25^\circ$ at $\beta = 66^\circ$, at which point occultations no longer occur. Some nearby source effects are easy to identify, for example the effects on measurements of the Crab due

to the December 2009 very bright outburst of A0535+262 ($\sim 4.5^\circ$ away). But crowded regions such as the Galactic Center are difficult for GBM to observe and can result in a flux measurement that is the sum of multiple sources within $\sim 1^\circ$.

2.3.3 "Ghost" Source Analysis

To measure systematic effects from those effects not listen in the sections above, $\sim$ 500 "ghost" sources were run through the EOT analysis for 3 years of data to determine fluxes and errors for those locations on the sky. These "ghost" sources are points on the sky with no source thus the measured flux is expected to be consistent with zero. The list was filtered to remove "ghost" sources within $\pm 10^\circ$ of the Galactic Center and any "ghost" sources within 2° of a source in the GBM catalog. The remaining $\sim$ 200 sources are distributed over the sky. Using the fluxes and statistical errors from the EOT analysis, histograms of the flux and statistical significance for the 12-25 keV, 25-50 keV, 50-100 keV, 100-300 keV, and 300-500 keV energy bands were found to be Gaussian distributed with mean values consistent with zero as expected. For the statistical significance histograms, the Gaussian widths are expected to be $\sigma = 1$ if systematic effects are negligible. The significance histograms were fit to a Gaussian, and the widths peaked with $\sigma_{sig} \approx 2.5$ in the 12-25 keV band and decreased to $\sigma_{sig} \approx 1$ by the 300-500 keV band indicating the significance of the systematic errors decreases with increasing energy. The flux histograms were also fit with a Gaussian with widths increasing with increasing energy. The Gaussian widths of the flux histograms (σ_{flux}) were taken to be a measure of the total error in the energy band. The statistical error was estimated to be the width of the flux distribution divided by the width of the significance distribution such that

$$\sigma_{stat} = \frac{\sigma_{flux}}{\sigma_{sig}}. \tag{2.6}$$

Table 2.1: Gaussian Widths for Significance, Flux, "Corrected" Significance, and Systematic Errors for 12- 500 keV Energy Bands

Energy Band keV	Sig. Width σ_{sig}	Flux Width σ_{flux} (mCrab)	"Corrected" Sig. width σ	Sys. Error (mCrab)
12-25	2.56	3.23	1.04	2.9
25-50	1.45	2.87	0.98	2.1
50-100	1.19	3.58	1.00	1.9
100-300	1.11	6.00	1.00	2.6
300-500	1.01	43.07	1.00	8.1

The systematic error then is given by

$$\sigma_{sys} = \sqrt{\sigma_{total}^2 - \sigma_{stat}^2} = \sqrt{\sigma_{total}^2 - \left(\frac{\sigma_{flux}}{\sigma_{sig}}\right)^2} \tag{2.7}$$

Fig. 2.3 shows the significance histograms for the five energy bands from 12-500 keV. Fig. 2.4 shows the flux histograms over the same energy range. Fig. 2.5 shows the "corrected" significance histograms with the systematic errors added in quadrature to have a total significance. Table 2.1 shows the widths of the initial significance histograms, the flux histograms, the "corrected" histograms using the total error, and the systematic error for each energy band.

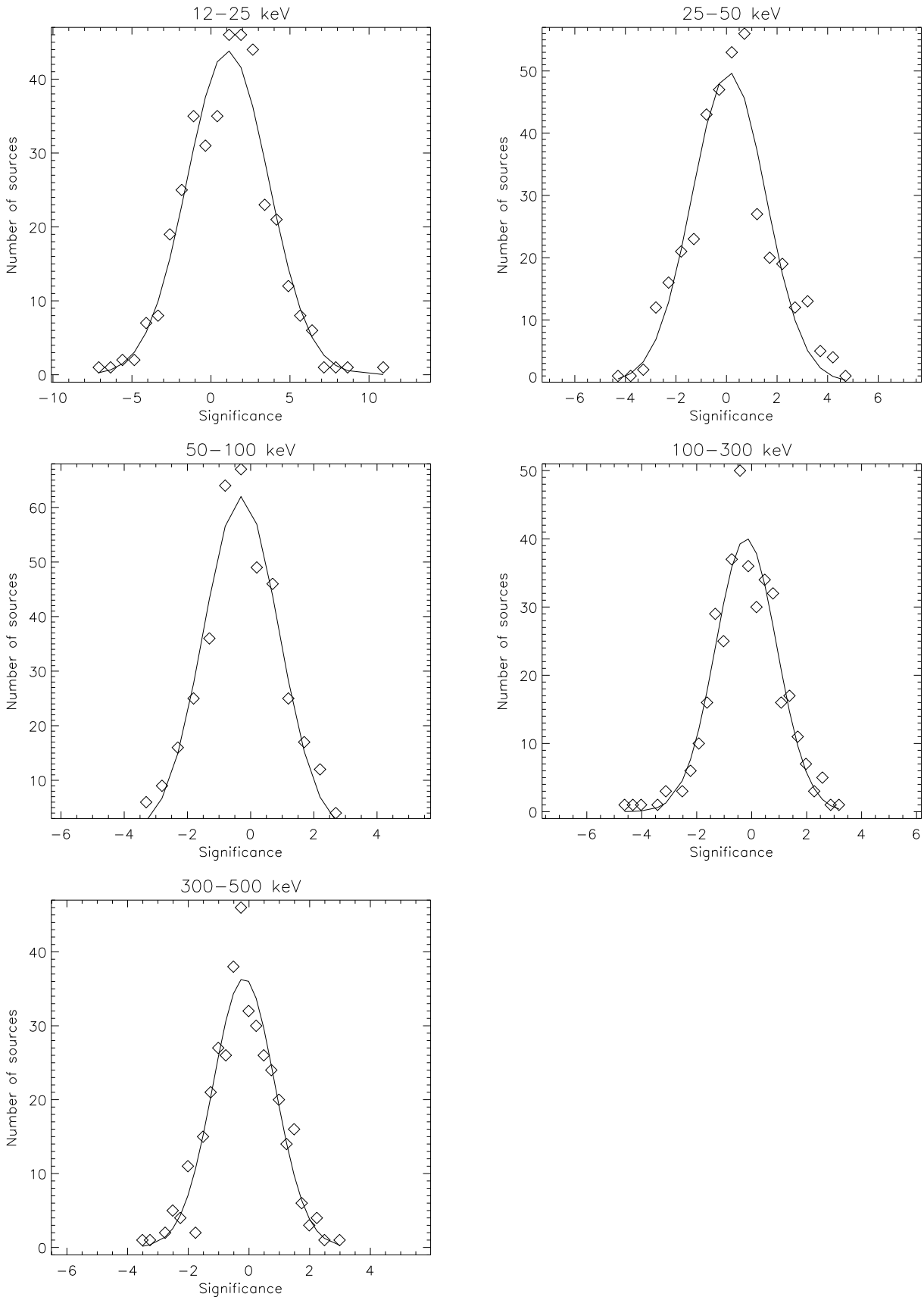

Figure 2.3: Histograms of Significance for 5 Energy Bands from 12-500 keV

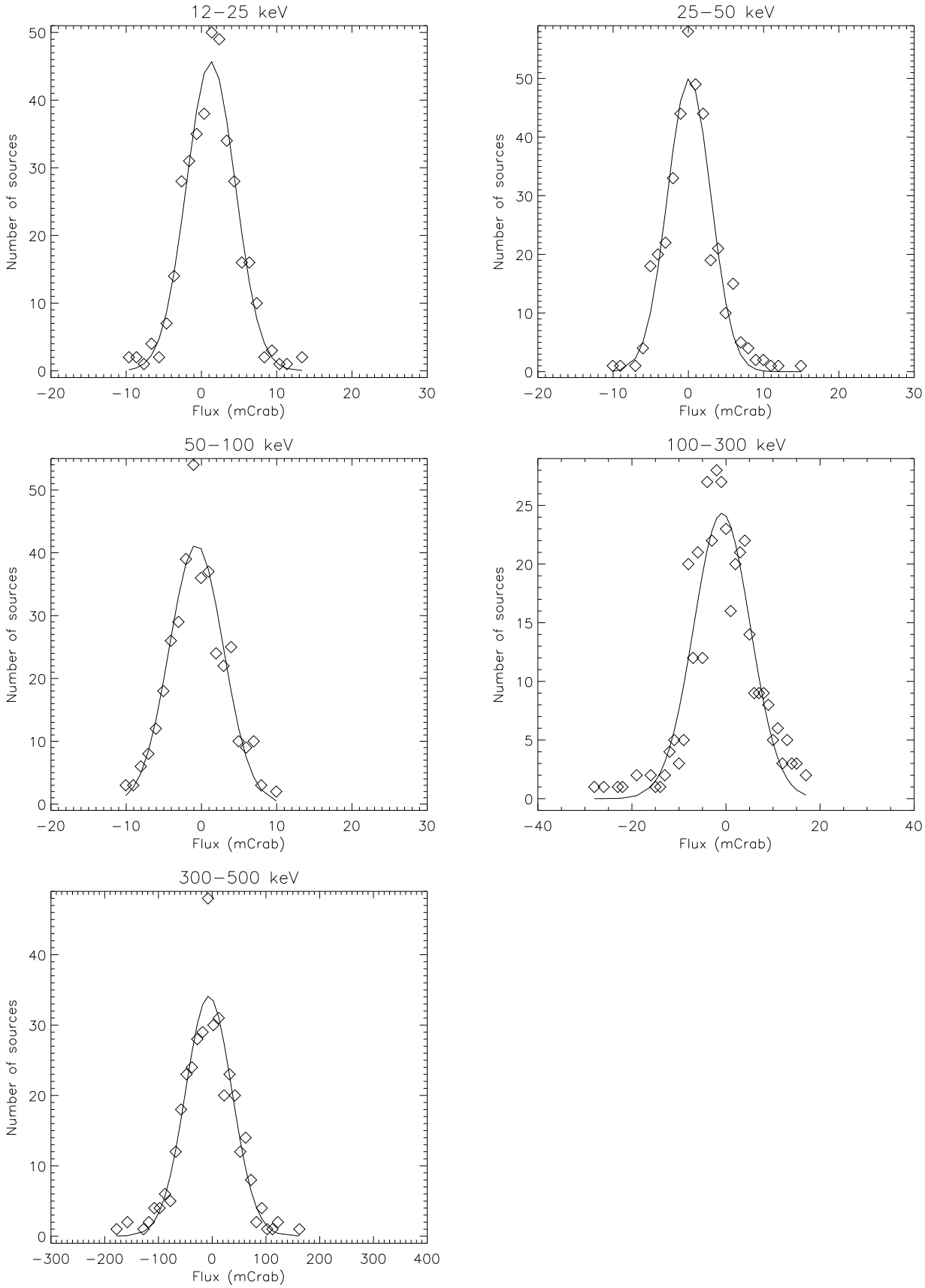

Figure 2.4: Histograms of Flux for 5 Energy Bands from 12-500 keV

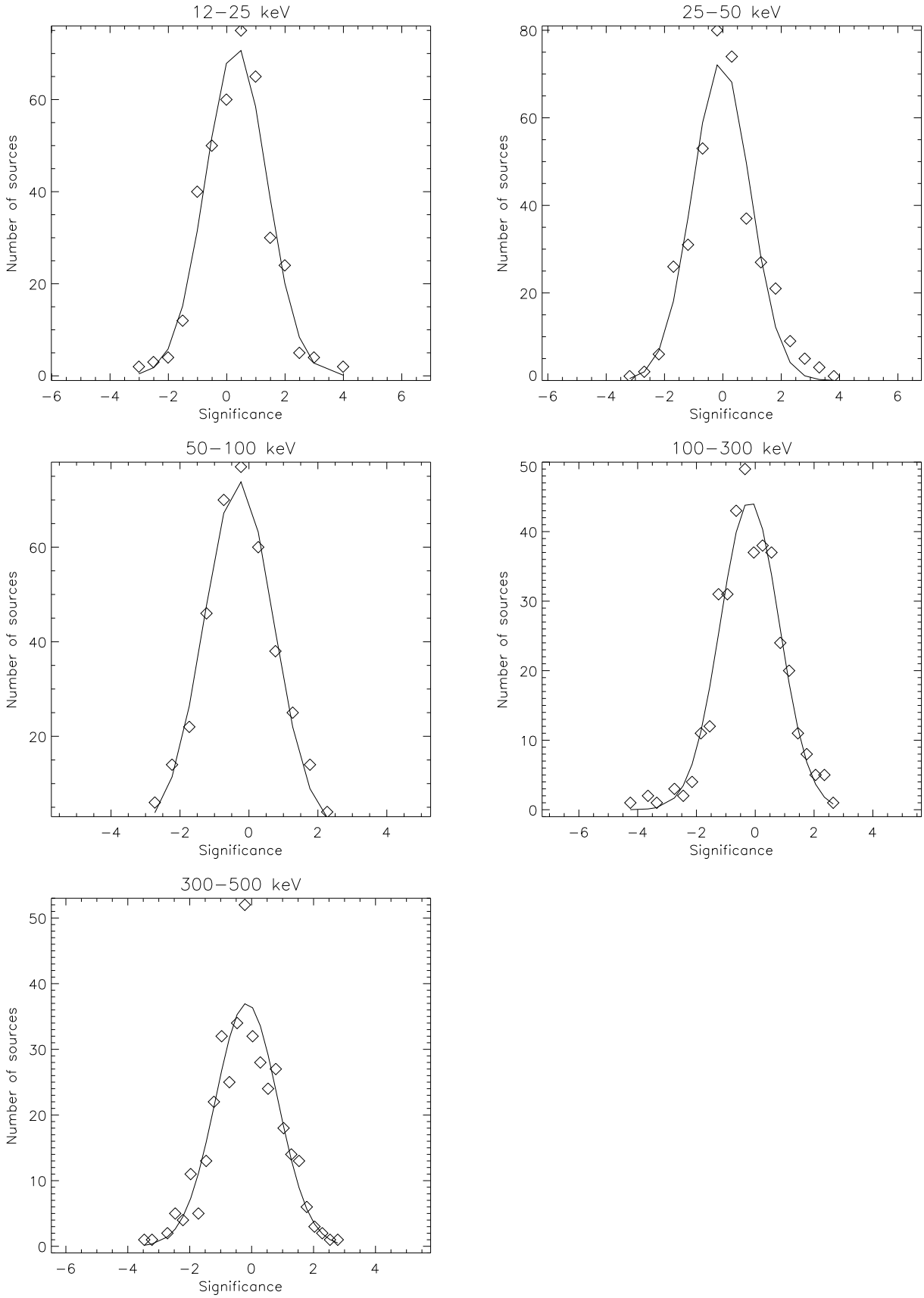

Figure 2.5: Histograms of "Corrected" Significance for 5 Energy Bands from 12-500 keV

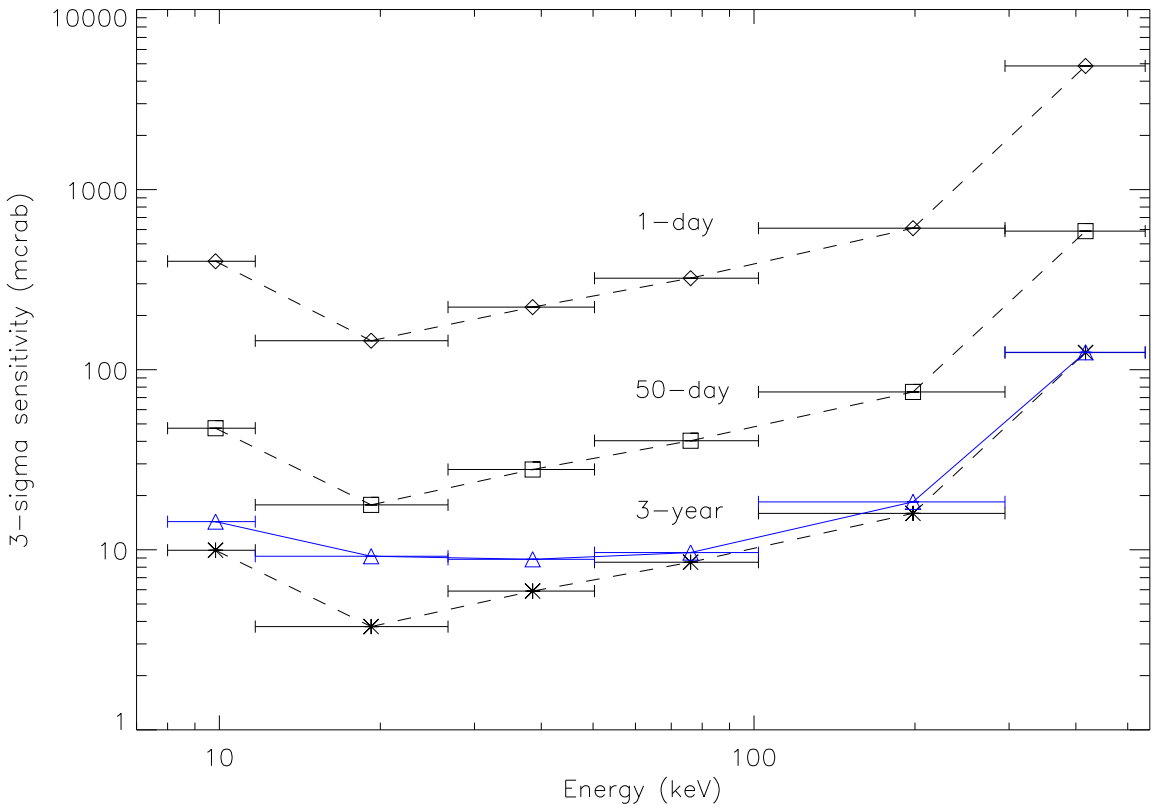

Figure 2.6: Sensitivity plot for 5 Energy Bands from 12-500 keV.

2.3.4 Sensitivity

The statistical sensitivity of the EOT with GBM was estimated using four detected sources from various locations on the sky. The sources are GRS 1915+105 (a persistent BHB relatively close to the Galactic Center), the Crab (an isolated source near the galactic anti-center), NGC 4151 (an AGN at a moderate declination), Cen A (an AGN at an extreme declination that is occasionally not occulted during a precession period). The 1-day, 50-day, and 3-year fluxes and errors were calculated for each source. The average error was computed for the source for each energy channel for the three time periods. The approximate statistical sensitivities for each source for each time period were taken to be three times the average error and converted to mCrab units. The sensitivities for each source were averaged to get

an average 1-day, 50-day, and 3-year 3σ sensitivity. Fig. 2.6[1] (Wilson-Hodge et al., 2012) shows the estimated 3σ sensitivities for the 12-500 keV energy bands for 1 day (diamonds), 50 days (squares), 3 years (asterisks), and 3 years with systematic errors included (triangles).

2.3.5 Source Catalog

The sources selected for the GBM EOT catalog have been compiled from numerous other instrument catalogs in similar energy ranges, such as BATSE, *Swift*/BAT, *RXTE*/ASM, and MAXI. Persistent sources in the BAT catalog with fluxes above ~ 10 mCrab and persistent ASM and *MAXI* sources with fluxes above ~ 20 mCrab were added. Cataclysmic variables (CVs) and Supergiant Fast X-ray Transients (SFXTs) detected by *INTEGRAL* or BAT were added as well. AGN detected by *CGRO*/OSSE were selected along with pulsar wind nebulae and gamma-ray binaries from the LAT catalog (Nolan et al., 2012). Additional LAT AGN were selected based on the criteria that they were $> 10^{\circ}$ from the galactic plane and classified as a BL Lac object with a high synchrotron peak or a flat-spectrum radio quasar (FSRQ) source with a low synchrotron peak. For BL Lac objects, the fall off from the synchrotron peak in the spectral energy distribution is in the GBM energy range while the LAT observes the inverse Compton (IC) peak. For the FSRQs, the rise of the IC peak is at GBM energies and the fall of the IC peak at LAT energies. For the 3-year catalog there were 209 sources: 71 AGN, 52 low-mass X-ray binary/ neutron star systems, 40 high-mass X-ray binary/ neutron star systems (including 5 SFXTs), 19 black hole candidates, 8 pulsars/pulsar wind nebulae/supernova remnants, 6 CVs, 4 gamma-ray binaries, 2 galaxy clusters, 3 stars including the Sun, 2 soft gamma repeaters, 1 globular cluster, and 1 tidal disruption event (Wilson-Hodge et al., 2012).

[1]Reproduced by permission of the AAS

Chapter 3
Imaging with Earth Occultation

3.1 Introduction

The EOT requires an input catalog of source positions to predict occultation times and thus measure source fluxes. This requirement means that an imaging method is needed to locate sources not in the input catalog. Hard X-ray imaging presents challenges not faced at lower energies. Imaging at optical wavelengths uses the traditional methods of refractive lenses and mirrors oriented normally to the incoming photons producing a direct image on a focal plane. Higher energy photons are more difficult to focus. At soft X-ray energies ($\sim 0.1 - 10$ keV), photons can be focused using parabolic mirrors shaped so that photons enter at grazing angles which allows for total reflection down to the focal plane (Giacconi & Rossi, 1960). Such an optical design was employed with the *Chandra* soft X-ray satellite. This designed has been modified for the *NuSTAR* mission (5-80 keV) for the first direct imaging satellite in the hard X-rays (Harrison et al., 2010).

A common design for imaging at hard X-rays and soft γ-rays energies (10 keV - 1 MeV) is in an indirect imaging method using a coded aperture (e.g. *Swift*/BAT and *INTEGRAL*/SPI). This technique spatially modulates incident photons through a "coded mask" onto a detector plane below, resulting in a shadow pattern (Caroli et al., 1987). Using the known mask pattern, the shadow pattern can be deconvolved to form an image.

Several indirect imaging methods have been developed using Earth occultation. Occultation transform imaging (Zhang et al., 1993, 1994, 1995) and the Likelihood Imaging

Method for BATSE Occultation data (LIMBO) (Shaw et al., 2004) were developed for use with BATSE, and Imaging with a Differential filter using the Earth Occultation Method (IDEOM) (Rodi et al., 2011) was developed for GBM. Earth occultation imaging methods have been able to use the wide field of view of BATSE and GBM to image large parts of the sky, which is not practical with *NuSTAR*'s field of view $\sim 10'$. They also use simple, uncollimated, non-imaging detectors ($\sim$ 10 detectors) unlike coded aperture imaging that requires a heavy mask of lead or tungsten and a read out channel for each detector pixel ($> 32,000$ for BAT (Barthelmy et al., 2005)).

Earth occultation imaging methods are tomographic methods that build images of the sky using projections of the Earth's limb on the sky. Because the detectors are uncollimated, the detector count-rate gives a measure of the brightness of the visible sky. Thus for a detector facing the Earth, the time derivative of the count rate is proportional to the line integral of the flux along the Earth's limb (Shaw et al., 2004). For a point on the sky, the flux (line integral) is measured along different angles with respect to the Earth's limb for rise and set steps giving different projections on the sky. During the orbital precession period of the satellite, a source's elevation angle β changes thus sampling all the available projection angles for that point on the sky. Figs. 3.1 - 3.6 show sampled projections from a single orbit for the Crab (declination of 22.01°) at $\sim$ 10 day intervals during the precession period from August 12, 2008 to October 4, 2008. The solid line marks the rise limb, and the dotted line marks the set limb. As the β angle changes, the rise/set limb projections cross the Crab's position at different angles. Fig. 3.7 overplots the sampled projections from the previous six figures to demonstrate how Earth occultation imaging samples a range of projections during an orbital precession period. The projections do not completely sample the entire region around the Crab, missing areas at roughly the same declination. The range of projection angles sampled is declination dependent with a wider range of projection angles sampled as declination increases, as shown in Fig. 3.8 and Fig. 3.9 which show 3C 273 (declination of 2.05°) and NGC 4151 (declination of 39.42°), respectively. Fig. 3.8 for 3C 273 shows a

Table 3.1: Example of systematic error due to uncatalogued sources

Energy Band	GX 1+4 Stand. Dev. (σ)	1E 1740-29 with GX 1+4 Stand. Dev. (σ)	1E 1740-29 without GX 1+4 Stand. Dev. (σ)
12-25 keV	21.7	8.6	10.0
25-50 keV	21.1	2.5	7.9
50-100 keV	9.4	3.1	4.5

larger unsampled region than both the Crab and NGC 4151, while Fig.3.9 shows a more completely sampled region around NGC 4151. Figs. 3.10 - 3.12 show the entire range of projection angles sampled over an entire precession period by plotting rise and set limbs for 2 orbits a day from August 12, 2008 to October 4, 2008 for the Crab, 3C 273, and NGC 4151, respectively.

A main motivation of IDEOM is to make the input source catalog as complete as possible to reduce systematic error in the EOT analysis caused by attributing flux from an unaccounted-for source to a source in the catalog. This problem can be seen for example with 1E 1740-29 and GX 1+4 (separated by $\sim 5.5^{\circ}$), which occasionally goes into outburst. If GX 1+4 is absent from the catalog, its transient flux is attributed to nearby sources (e.g. 1E 1740-29). The first two columns of Table 3.1 show the significance of 1E 1740-29 and GX 1+4 during a flare spanning MJD 55708 to 55774. The third column shows the significance for 1E 1740-29 during the same period when GX 1+4 is omitted from the catalog. The table shows an increase of $\sim 1.5\sigma$ in the first and third energy band and a $\sim 5\sigma$ increase in the second energy band for 1E 1740-29 when GX 1+4 is not taken into account. Fluxes are given in terms of standard deviations above background for the period MJD 55708-55744 when GX 1+4 is flaring. Thus having a catalog that is as complete as possible is necessary for accurate flux measurements.

3.2 Previous Work in Earth Occultation Imaging

Occultation transform imaging was the first technique to create images using Earth occultation. This method images a region of the sky by performing an inverse Radon transform on the differentiated count-rate data that corresponds to projections for that area of the sky. Then the image is deconvolved using a maximum entropy method (MEM) to locate sources in the image. With this method Zhang et al. (1993, 1994, 1995) generated images for time periods covering days to weeks and energies 20-300 keV. Image sizes ranged from $5^\circ \times 5^\circ$ to $40^\circ \times 40^\circ$. Regular analysis consisted of imaging the galactic plane with 27 sections of $30^\circ \times 30^\circ$ images (Zhang et al., 1994). Occultation transform imaging was able to discover a number of transient sources (Zhang et al., 1995), but it had several limitations. Because the Earth's limb is an arc, the linear approximation used restricts the effective image size to $\sim 20^\circ \times 20^\circ$ (Shaw et al., 2004). For images larger than this, distortion effects can result in difficulty calculating the correct source position. Also, this technique does not account for bright sources outside the field of view biasing the background. Projections from sources such as the Crab, Sco X-1, and Cyg X-1 can extend for 10s of degrees. MEM is a non-linear iterative process, which can make comparing images (Narayan & Nityananda, 1986) and combining images (Westmore, 2002) difficult.

LIMBO (Shaw et al., 2004) generated all-sky images using a likelihood statistic for a grid of predefined source positions on the sky. In this method, the data were background subtracted using the BATSE Mass Model (BAMM) to account for cosmic ray interactions with the spacecraft, atmospheric albedo from Earth, and cosmic diffuse γ-rays, and was able to reduce the background flux by a factor of ~ 10. The background subtracted data were passed through a differential filter. A maximum likelihood statistic was calculated to determine the significance of a point on the grid of source positions based on the filtered data. All-sky images were generated using 489 days of BATSE data in a single energy range 25-160 keV. LIMBO showed improvements over occultation transform imaging with the ability to

generate all-sky images, account for bright sources, and easily sum images, but LIMBO's resolution was limited by the 2° separation of its sky grid points. Also, spectral information about the sources was lost by imaging only a single energy range.

3.3 Imaging with IDEOM

Like LIMBO, IDEOM uses a predefined grid of virtual sources. IDEOM though has finer resolution with 0.25° spacing, resulting in $\sim 660,000$ virtual sources. Energy-dependent occultation times are predicted for all the virtual sources. A 4-minute window of GBM CTIME data centered on the occultation time was selected for detectors that viewed the source at less than 75° from the detector normal. This cutoff angle was chosen because the detector response is poor past 75° as seen in Fig. 3.13[1] (Meegan et al., 2009). The plot shows the angular dependence of the effective area for the NaI detectors. Based on the 32 keV data (black circles), the effective area has dropped considerably at 75° to roughly 27% of the peak value, but the effective area is at roughly 60% of the peak based on the 273 keV data (blue squares). Thus 75° provides a suitable threshold for selecting detectors over the energy range from 12-300 keV.

A first order response correction is applied to the data by dividing by

$$\cos(\theta) \times (1 - e^{-\rho\sigma(E)d/\cos(\theta)}), \tag{3.1}$$

where θ is the source angle with respect to the detector normal, ρ is the density, σ is the energy-dependent detector absorption, and d is the detector thickness. For NaI, $\rho = 3.67$ g/cm^3 (International Programme on Chemical Safety, 2004), the detector thickness is 1.27 cm, and the photo electric absorptions are for 30.8 cm^2/g, 3.99 cm^2/g, and 0.408 cm^2/g (Berger et al., 1998) for the 12-50 keV, 50-100 keV, and 100-300 keV energy bands, respectively.

[1]Reproduced by permission of the AAS

To sample as many projection angles as possible, data from rise occultation steps and set occultation steps were combined by rotating data from rise occultation steps about the occultation time at the center of the window. The windows were stacked in 0.256-sec resolution, and the weighted average was calculated using the selected detectors from all the occultation steps. Poisson errors were calculated and propagated throughout the analysis. The average window was rebinned to 2.048-sec resolution before being passed through a differential filter of the form

$$o_i = \frac{\sum_{j=i+f_a}^{j=i+f_a+f_b} r_j - \sum_{j=i-f_a-f_b}^{j=i-f_a} r_j}{f_b}, \tag{3.2}$$

where f_a and f_b are the inner and outer time boundaries, respectively, r_j is the number of counts in bin j and o_i is the filtered value for bin i. This equation is based on the filter used by Shaw et al. (2004). The filter works by summing up f_b time bins of data, leaving a gap of $2f_a$ time bins, and summing up the next f_b time bins of data. Then the difference between the two f_b sums is calculated and divided by f_b. In other words, the filter calculated the sum f_b bins before the occultation time and f_b bins after the occultation time. Filtering the entire window produces a dip at the occultation time while smoothing background features as shown in Fig. 3.14, which shows data for 11 days for the position of the Crab. The top panel shows the averaged occultation window The virtual source intensity is calculated from the amplitude of the dip by fitting bins within $\pm(2f_a + f_b)$ of the occultation time at the center of the window to a polynomial, and the bins outside this region to a spline function joined by a straight line. The amplitude of the virtual source is found by taking the difference between the two fits at the occultation time. A region of $\pm(2f_a + f_b)$ is used to ensure that the dip is fully enclosed and thus the difference between the dip and the background is optimally sampled. The bottom panel of Figure 3.14 shows the filtered window with the polynomial fit in (green) stars and the spline fit in (red) triangles. The outer dashed lines are the boundaries for the polynomial fit, and the middle dashed line denotes the occultation

time.

Shaw et al. (2004) points out that the imaging resolution and sensitivity depend on the choice of the inner and outer time boundaries, f_a and f_b, respectively. To maximize the sensitivity the inner bound value should be large enough so that $2f_a$ is roughly equal to the occultation duration thus maximizing the difference between the total transmission and total attenuation. Increasing the value of f_b decreases the resolution, making the dip wider while decreasing f_b too much makes the average susceptible to background fluctuations. Fig. 3.15 shows a model occultation step with the filtered data overplotted using different combinations of f_a and f_b. The solid black line uses $f_a = 0, f_b = 10$, giving good position resolution of 0.7° half with at half maximum (HWHM), but relatively low sensitivity; the blue dot dash line uses $f_a = 5, f_b = 5$ has a flat top showing that $f_a = 5$ is too big of an inner bound and has poor resolution of 1.1° HWHM. The red dashed line has $f_a = 3, f_b = 8$, which peaks at $\sim 100\%$ thus having good sensitivity and a reasonable resolution of 0.83° HWHM. Thus values of $f_a = 3$ and $f_b = 8$ have been chosen as they result in good sensitivity with reasonably good resolution.

3.3.1 Systematic Effects

Besides the data cuts used by the EOT for SAA passes, high spacecraft spin rate, and bright solar flares, IDEOM takes two additional systematic effects into account in the processing: 1) source interference with bright sources and 2) windows in which the rise and set steps of a bright source dominate the spline background fit. The issue of source interference arises from the ambiguity of where along the Earth's limb the measured flux originates. Since the GBM detectors have no direct imaging capability, the flux for an occultation time can be attributed to any location on the sky along the Earth's limb. Consequently, bright sources (e.g. Crab, Cyg X-1, Sco X-1) produce a statistically significant characteristic "X" pattern that can extend for tens of degrees on the sky. These "arms" are the result of projections remaining in a similar orientation for a relatively long time as the source reaches

its maximum and minimum β angles during the *Fermi* precession period. These projections may overwhelm any flux that comes from possible faint sources lying on or near one of these arms or systematically over estimate the flux from a location. To mitigate the effects of source confusion, an algorithm has been developed to ignore occultation windows for virtual sources when bright sources occult close in time (< 11 seconds) but far away on the sky ($> 10^{\circ}$). Fig. 3.16 shows the extent of the "arms" in the 12-25 keV band from bright sources from a single precession period, especially the Crab ($\alpha = 83.63, \delta = 22.01$) and Sco X-1 ($\alpha = 244.98, \delta = -15.64$).

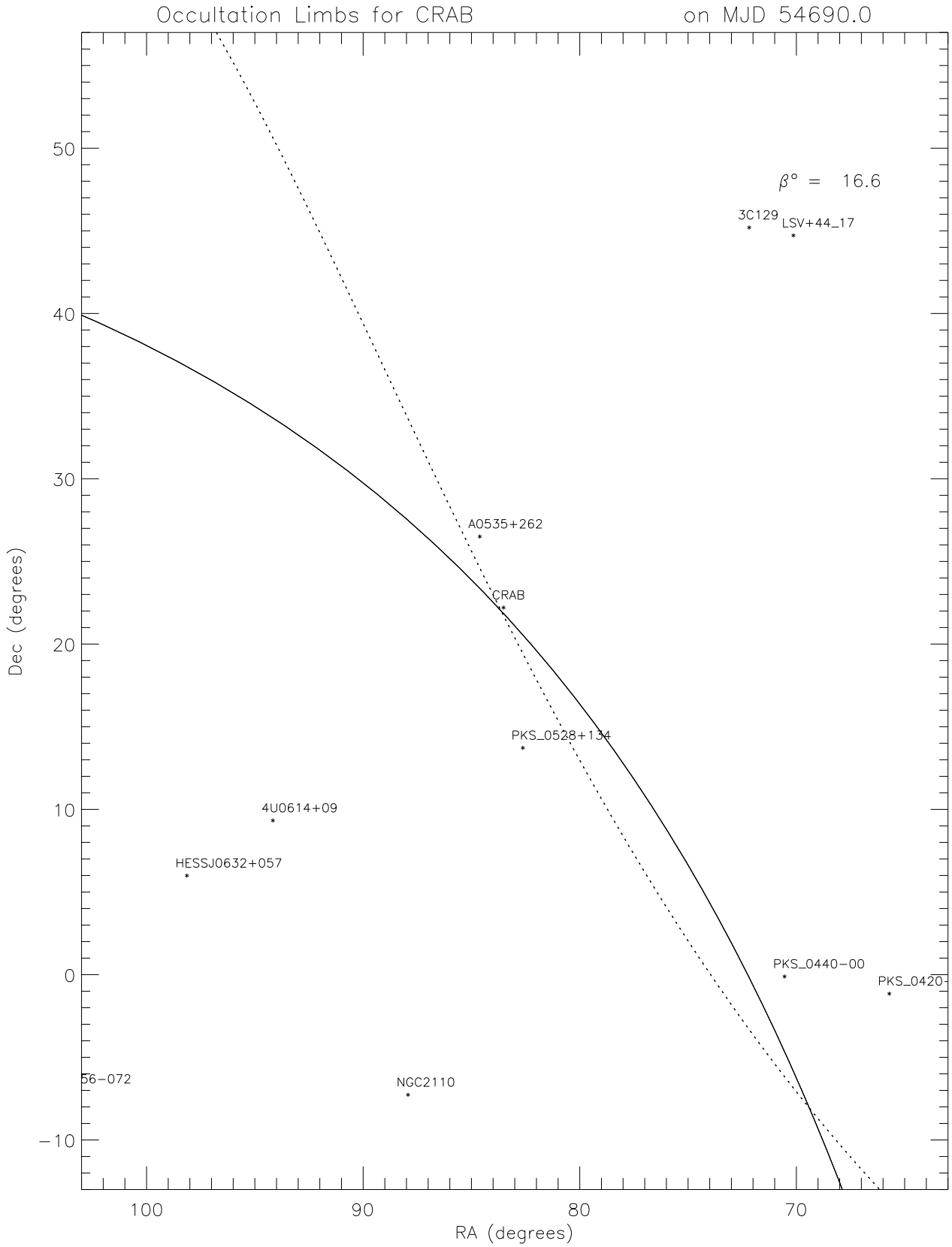

Figure 3.1: Limb Plot for the Crab on August 12, 2008 (MJD 54690). Solid line denotes "rise" step, and dotted line denotes "set" step.

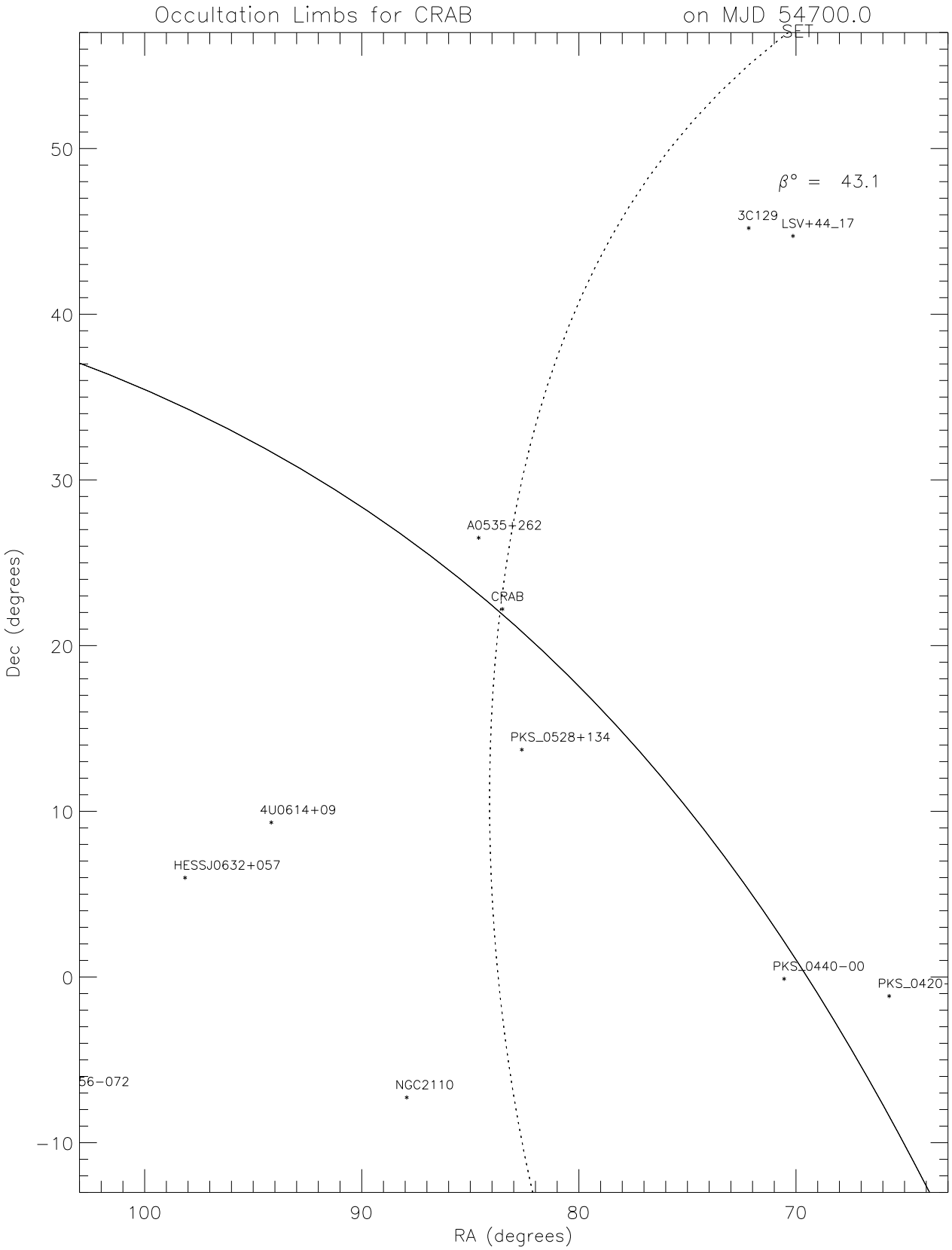

Figure 3.2: Limb Plot for the Crab on August 22, 2008 (MJD 54700). Solid line denotes "rise" step, and dotted line denotes "set" step.

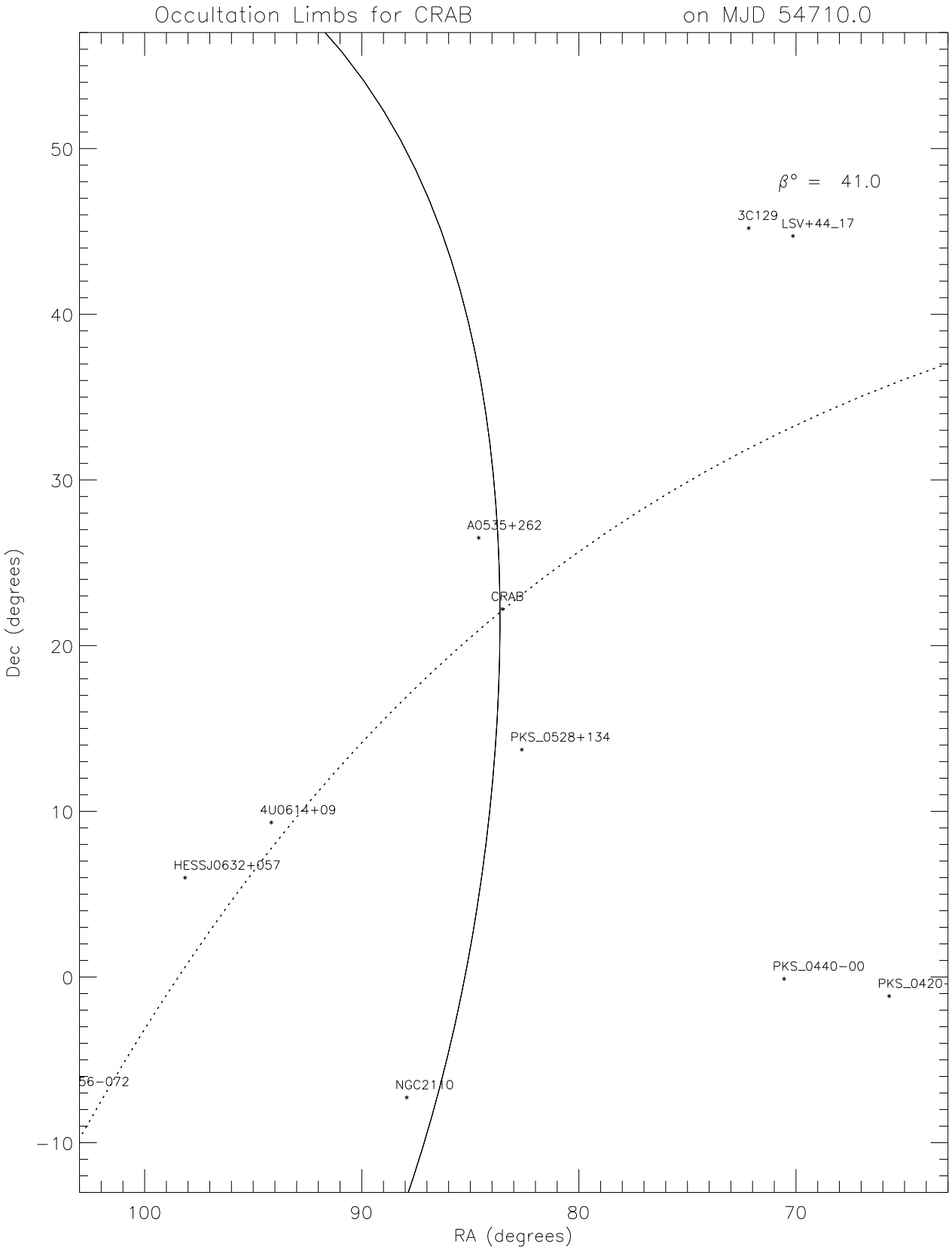

Figure 3.3: Limb Plot for the Crab on September 1, 2008 (MJD 54710). Solid line denotes "rise" step, and dotted line denotes "set" step.

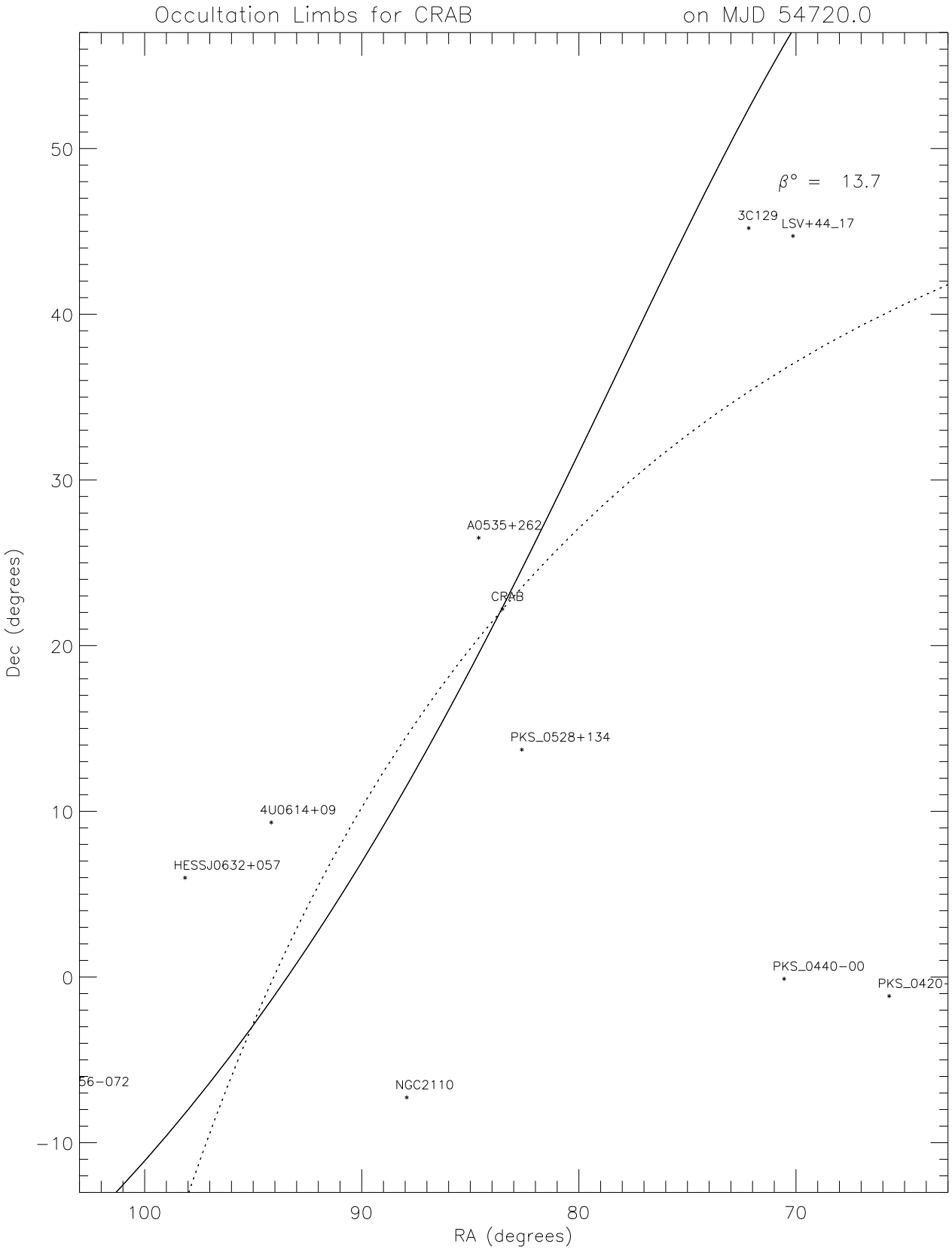

Figure 3.4: Limb Plot for the Crab on September 11, 2008 (MJD 54720). Solid line denotes "rise" step, and dotted line denotes "set" step.

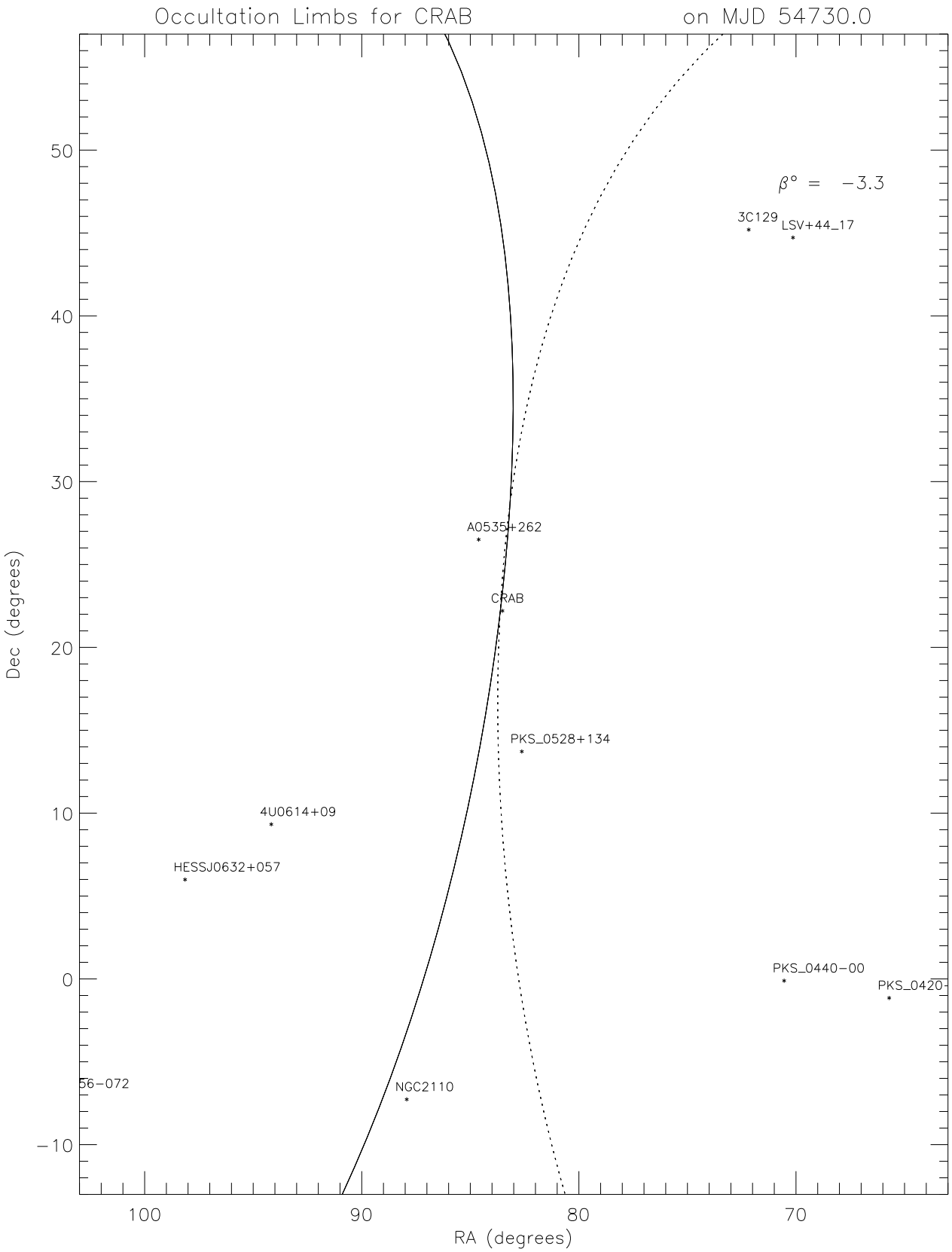

Figure 3.5: Limb Plot for the Crab on September 21, 2008 (MJD 54730). Solid line denotes "rise" step, and dotted line denotes "set" step.

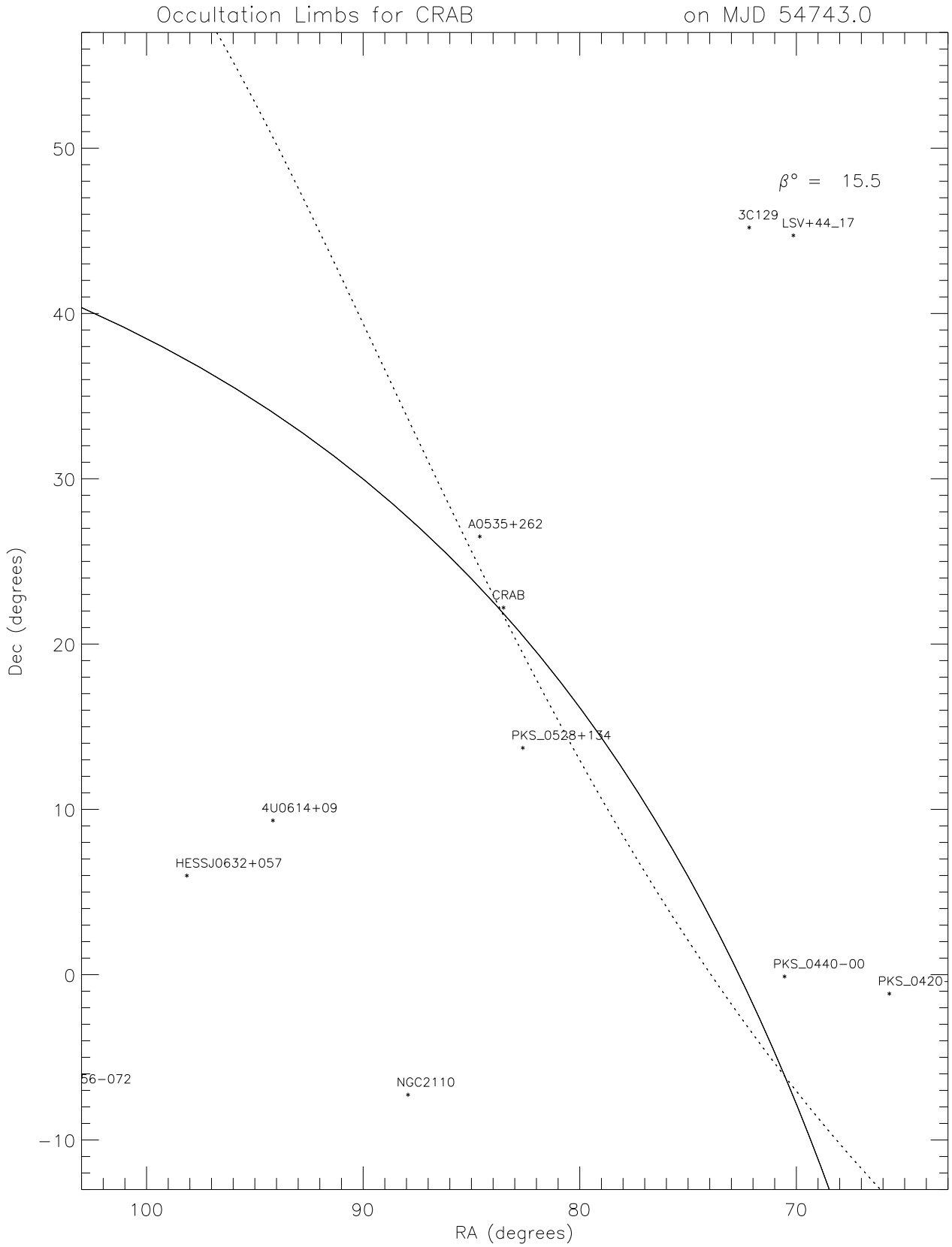

Figure 3.6: Limb Plot for the Crab on October 4, 2008 (MJD 54743). Solid line denotes "rise" step, and dotted line denotes "set" step.

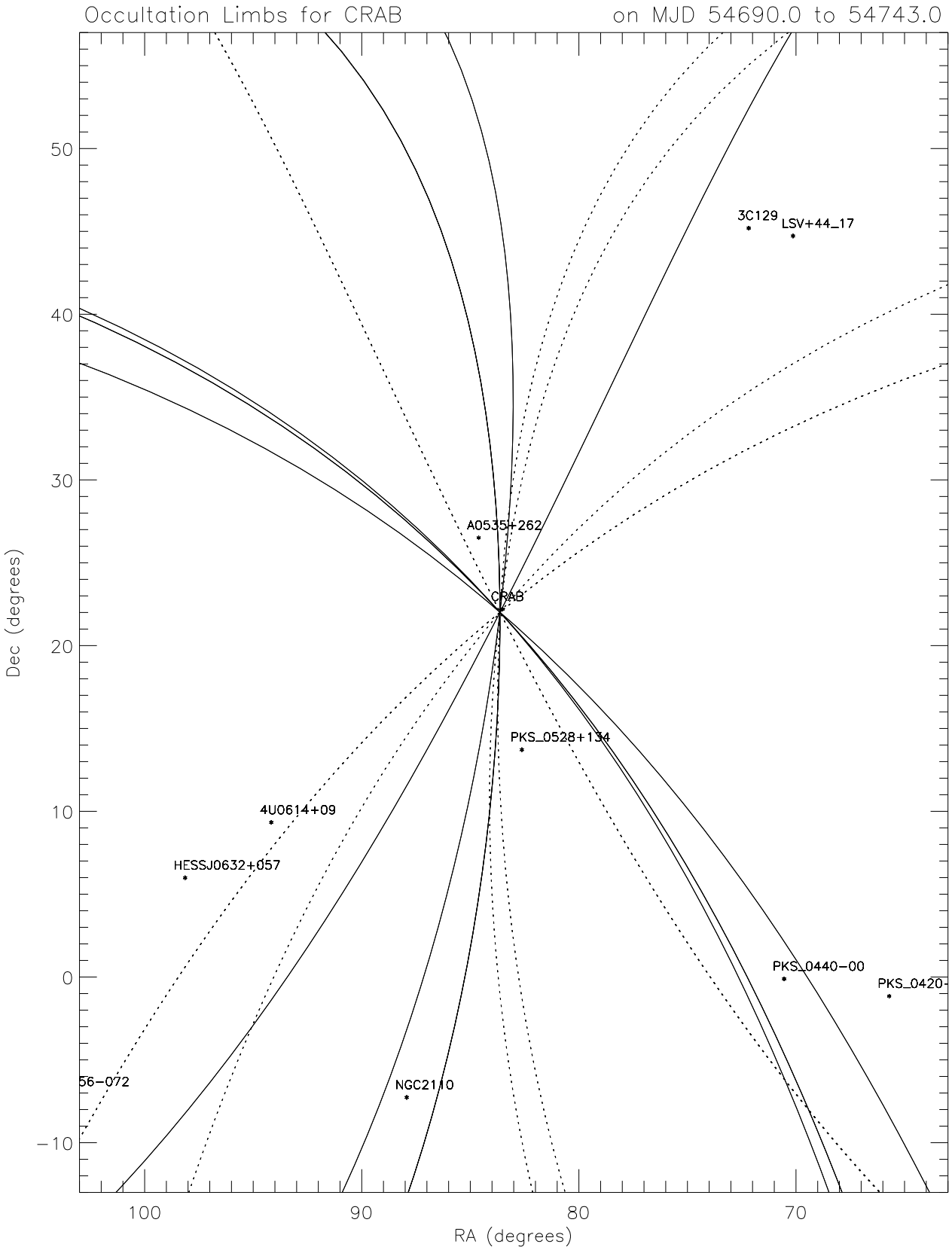

Figure 3.7: Limbs Overplotted for the Crab from Figs. 3.1 - 3.6. Solid lines denotes "rise" step, and dotted lines denotes "set" step.

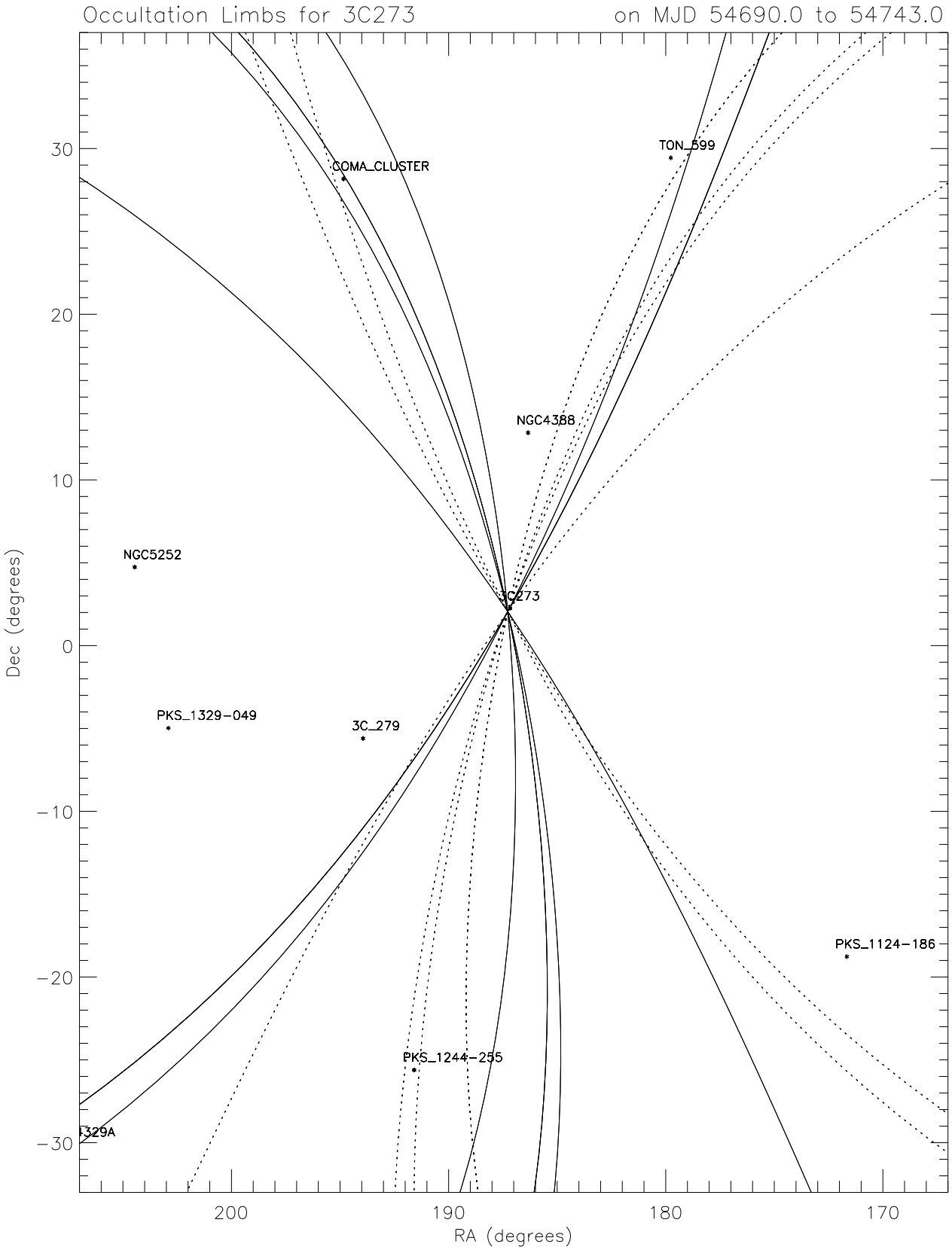

Figure 3.8: Limbs Overplotted for 3C 273 during precession period from Aug. 12, 2008 to Oct. 4, 2008. Solid lines denotes "rise" step, and dotted lines denotes "set" step.

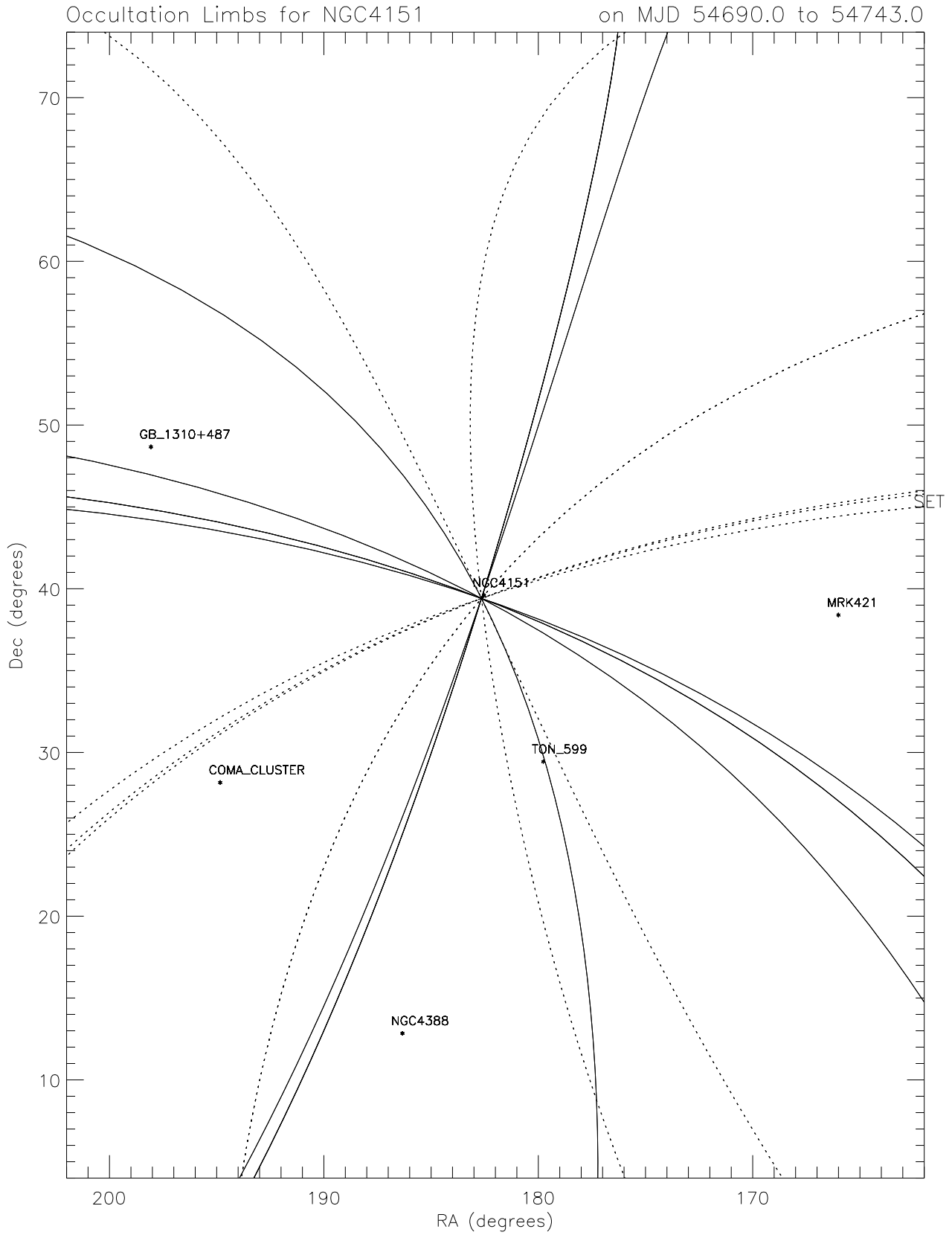

Figure 3.9: Limbs Overplotted for NGC 4151. Solid lines denotes "rise" step, and dotted lines denotes "set" step.

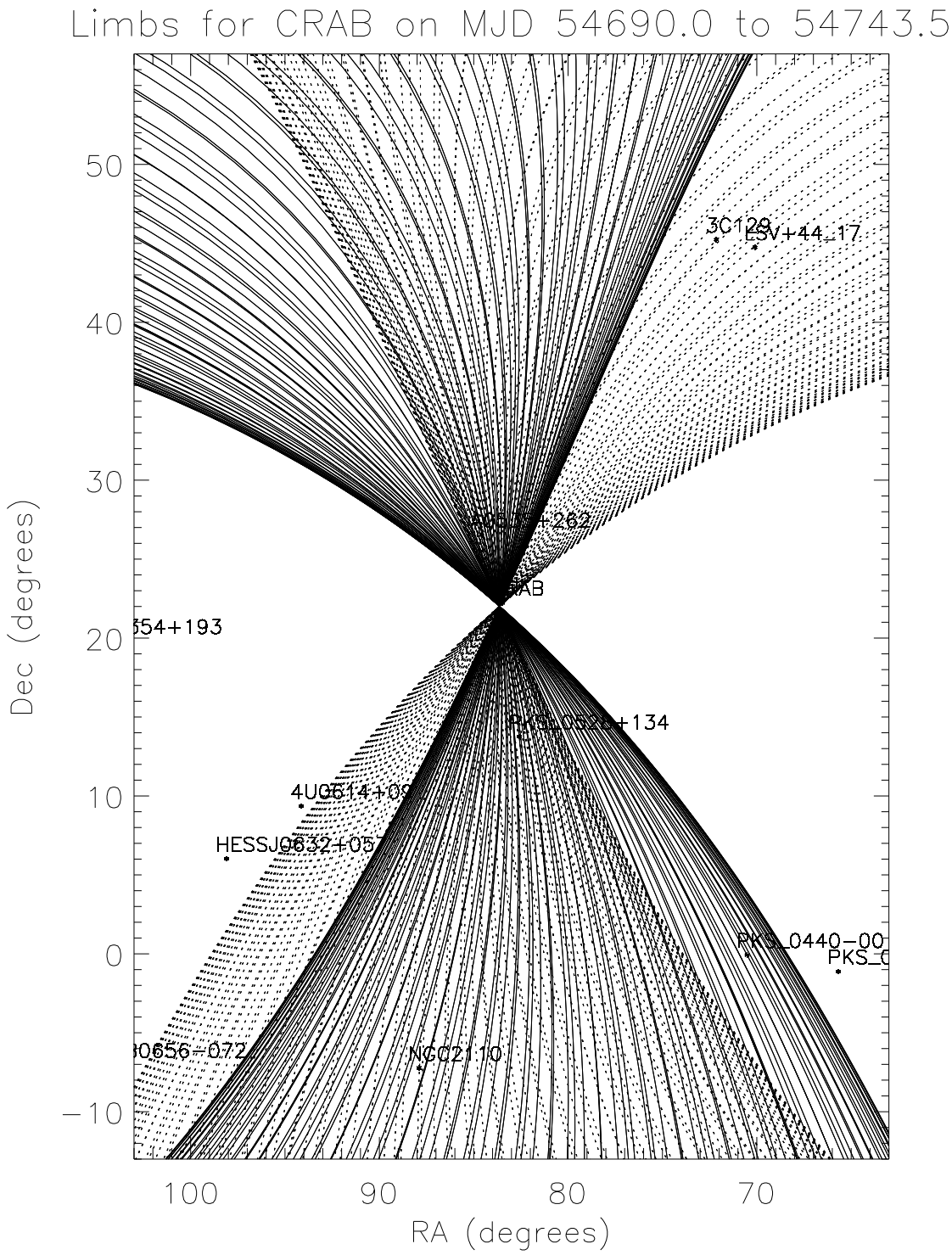

Figure 3.10: Limbs for Entire Precession Period Overplotted for the Crab. Solid lines denotes "rise" step, and dotted lines denotes "set" step.

SET

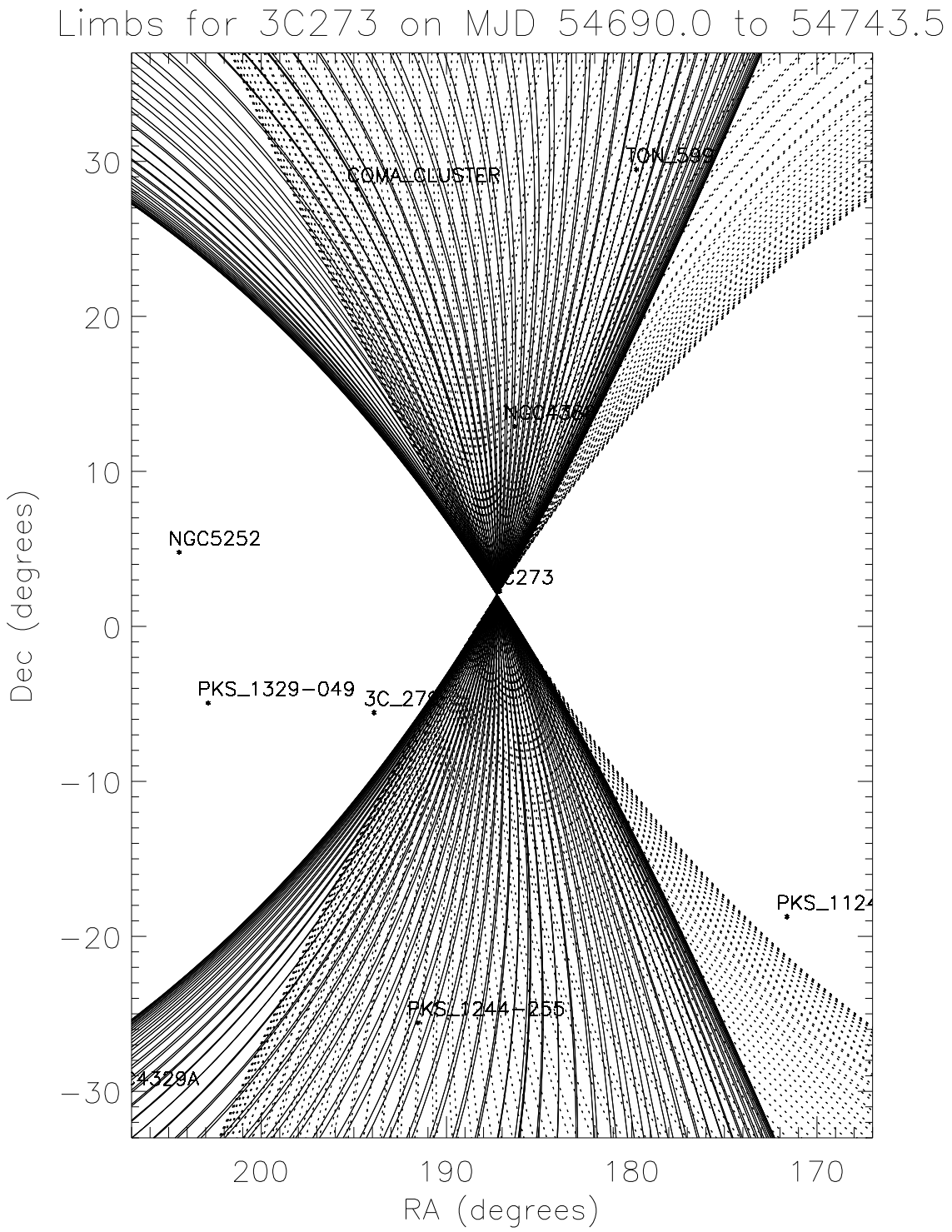

Figure 3.11: Limbs for Entire Precession Period Overplotted for 3C 273. Solid lines denotes "rise" step, and dotted lines denotes "set" step.

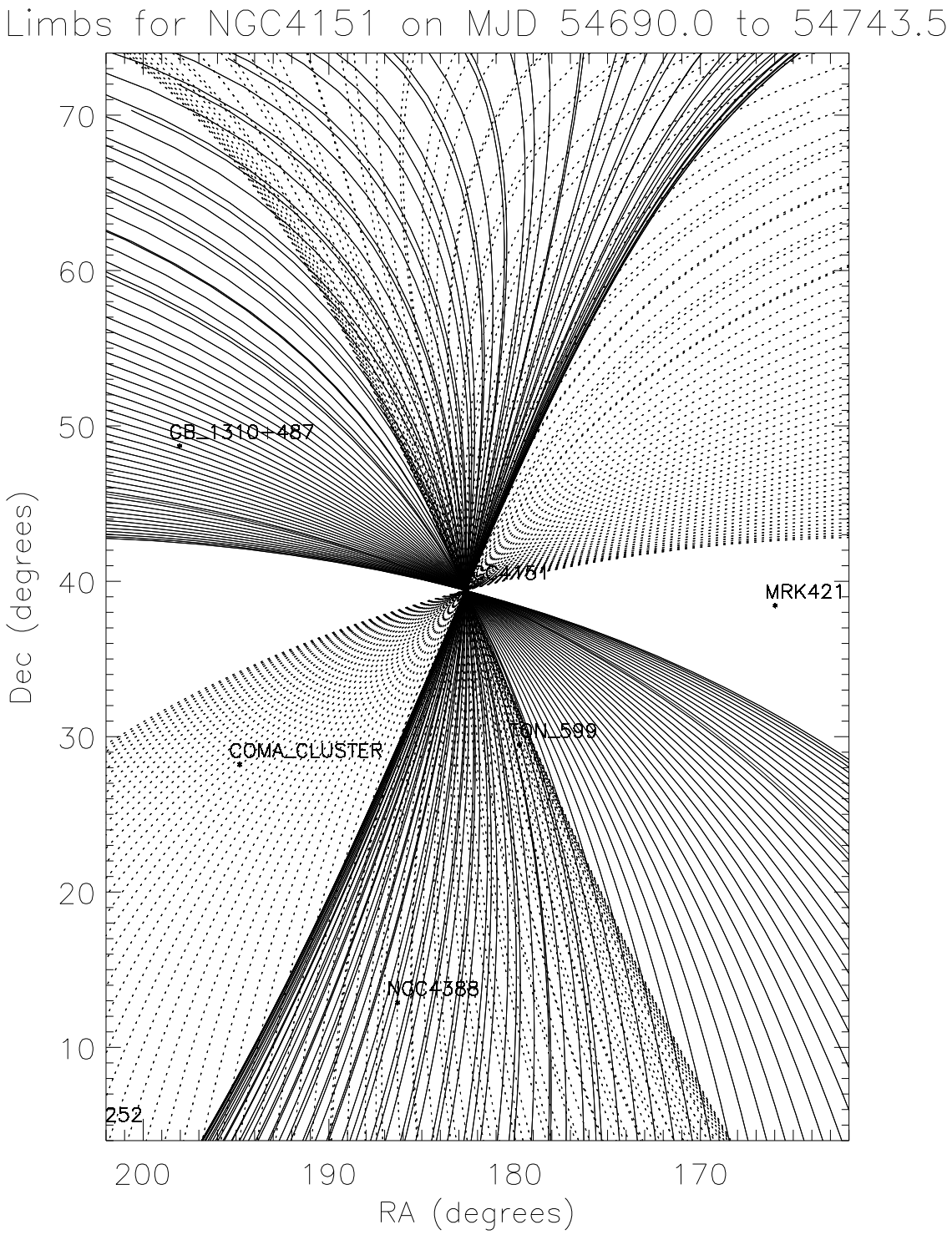

Figure 3.12: Limbs for Entire Precession Period Overplotted for NGC 4151. Solid lines denotes "rise" step, and dotted lines denotes "set" step.

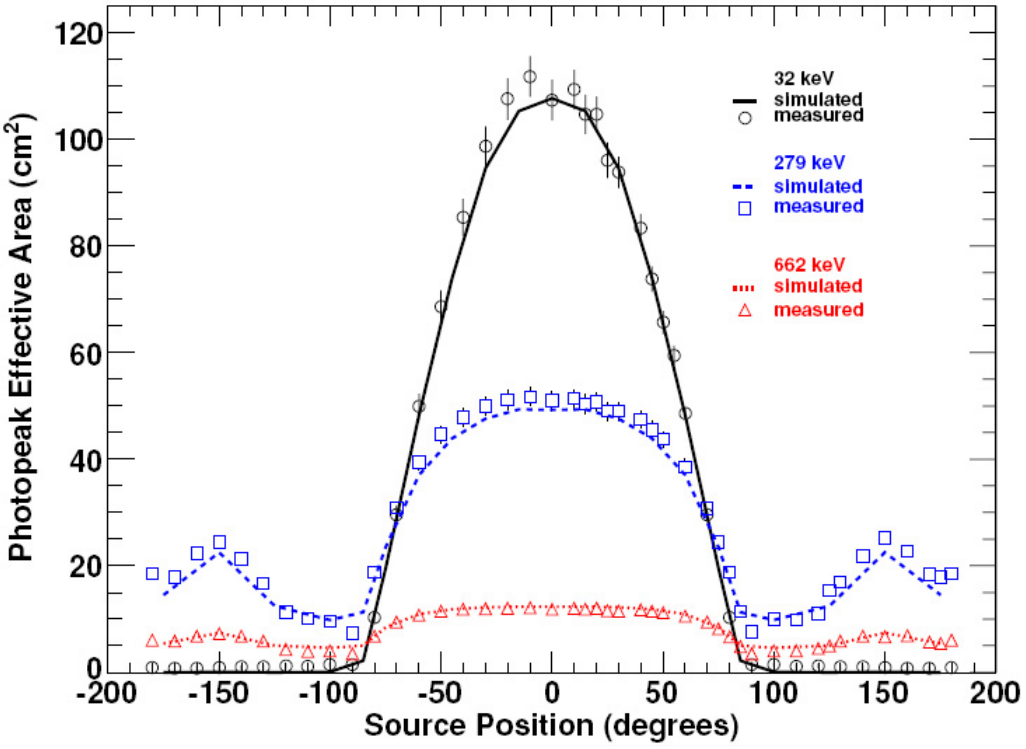

Figure 3.13: Angular Dependence of the NaI Detector Effective Area

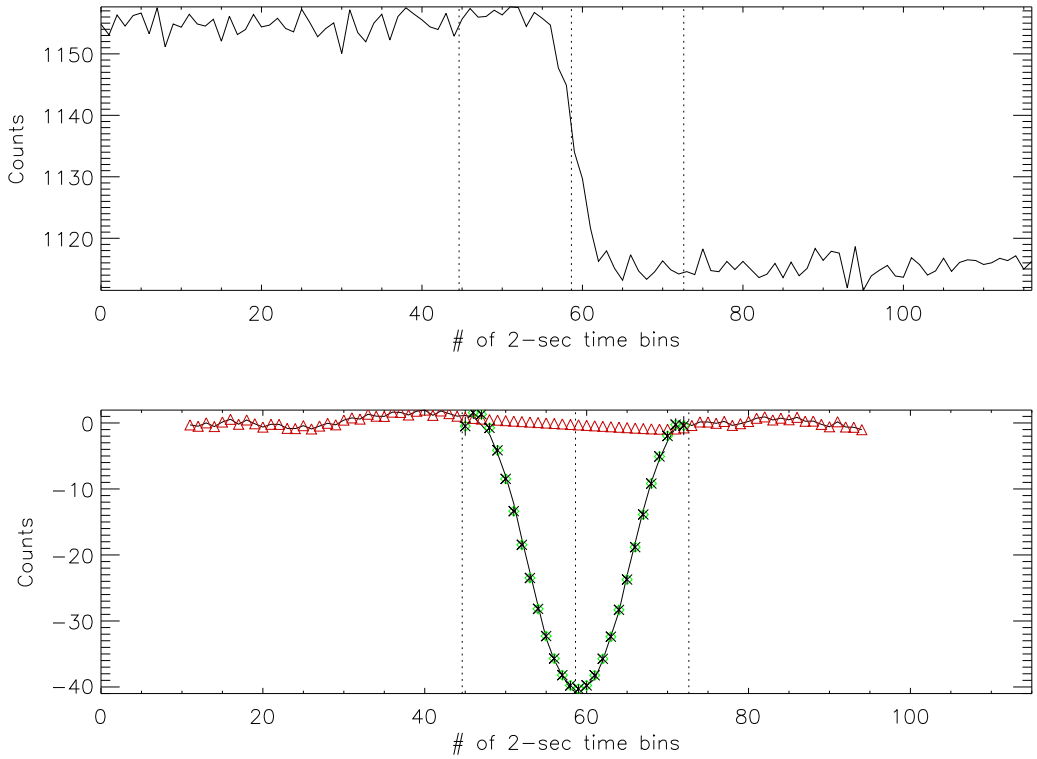

Figure 3.14: *Top*: Averaged window for 11 days for the Crab. *Bottom*: The filtered data with the central portion fit to a polynomial (green) stars, and the outer background portion fit to a spline function (red) triangles.

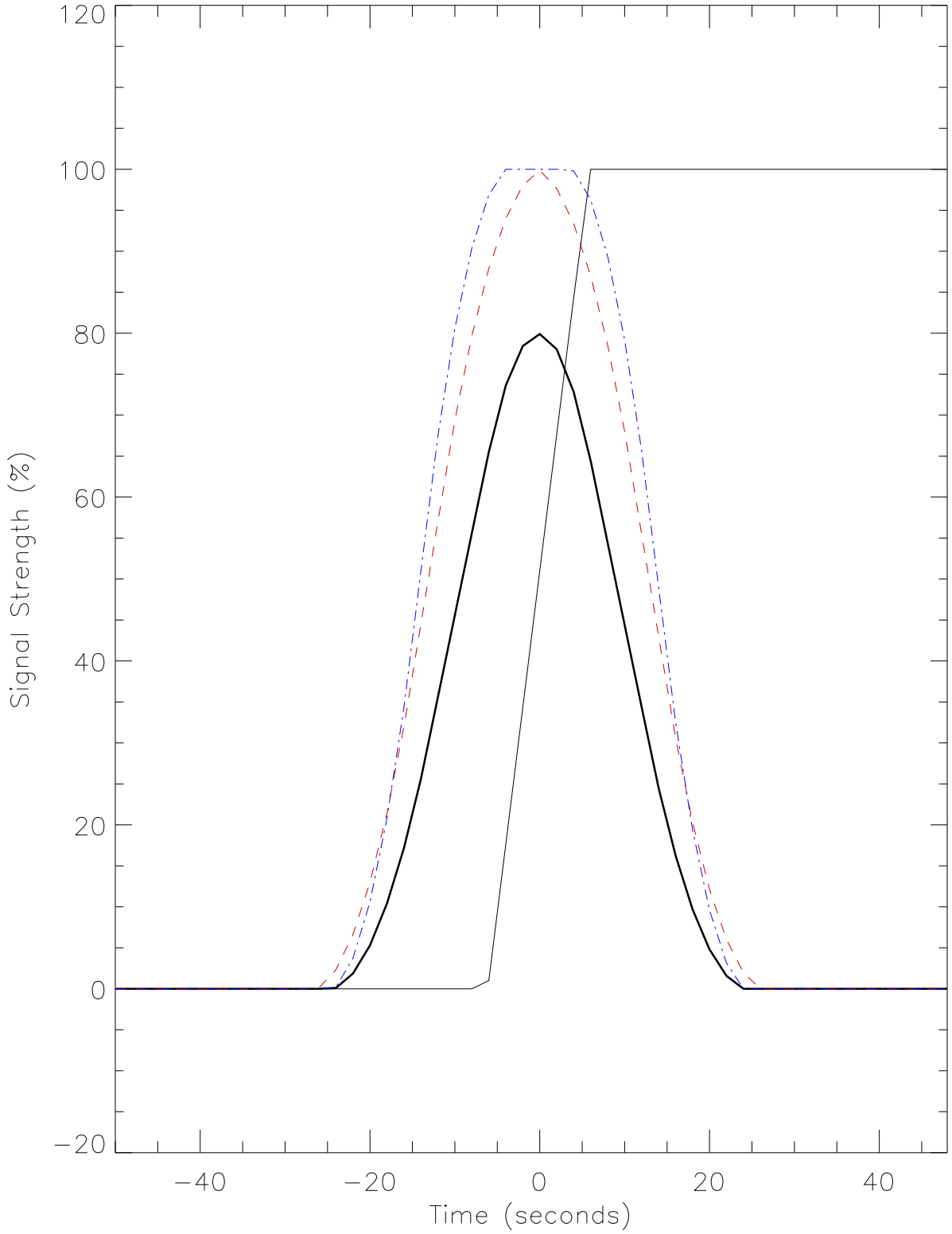

Figure 3.15: Comparison of Filtered data for Different Values Inner and Outer Bounds

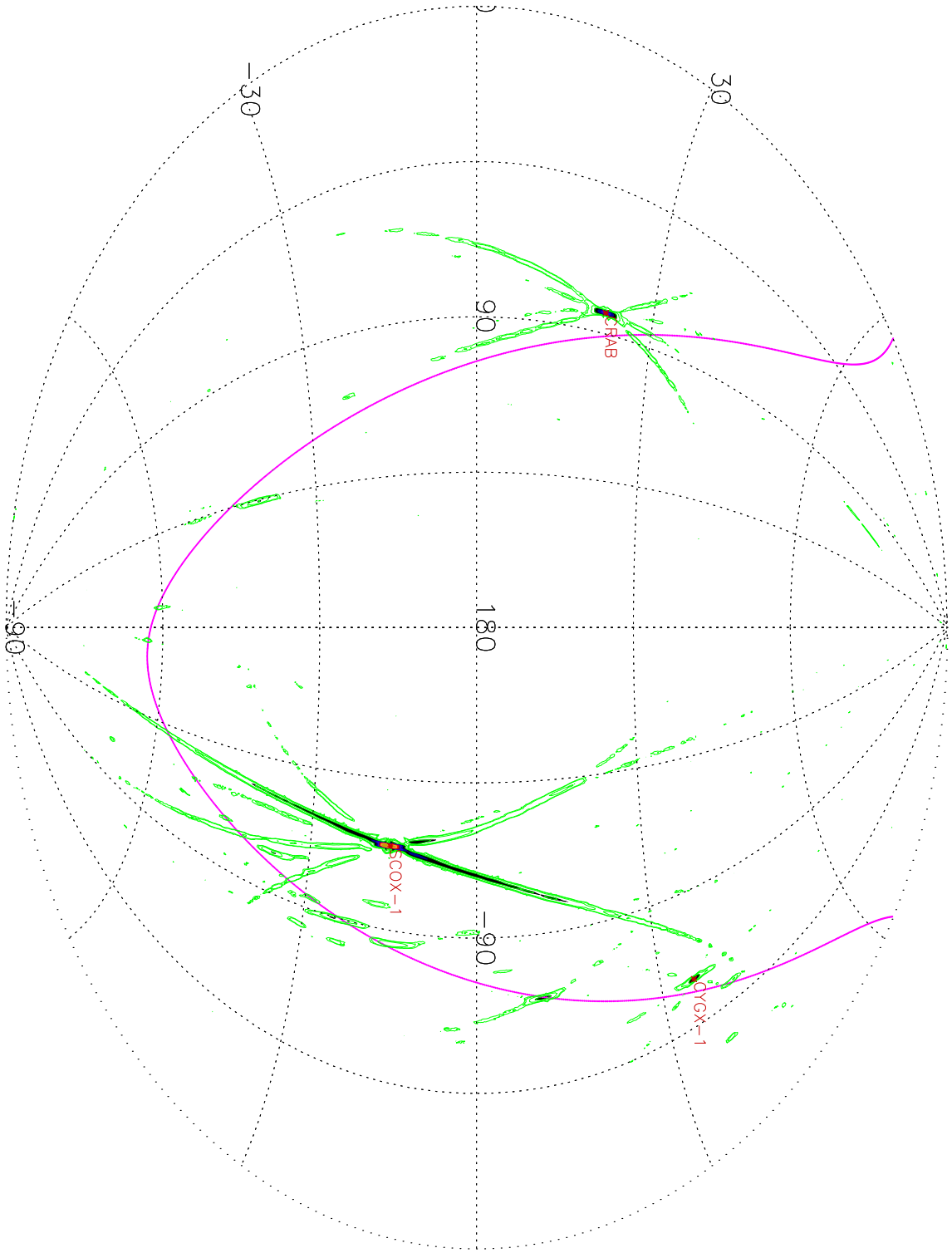

Figure 3.16: All-sky Significance Map in the 12-25 keV Band for One Precession Period without Accounting for Bright Sources

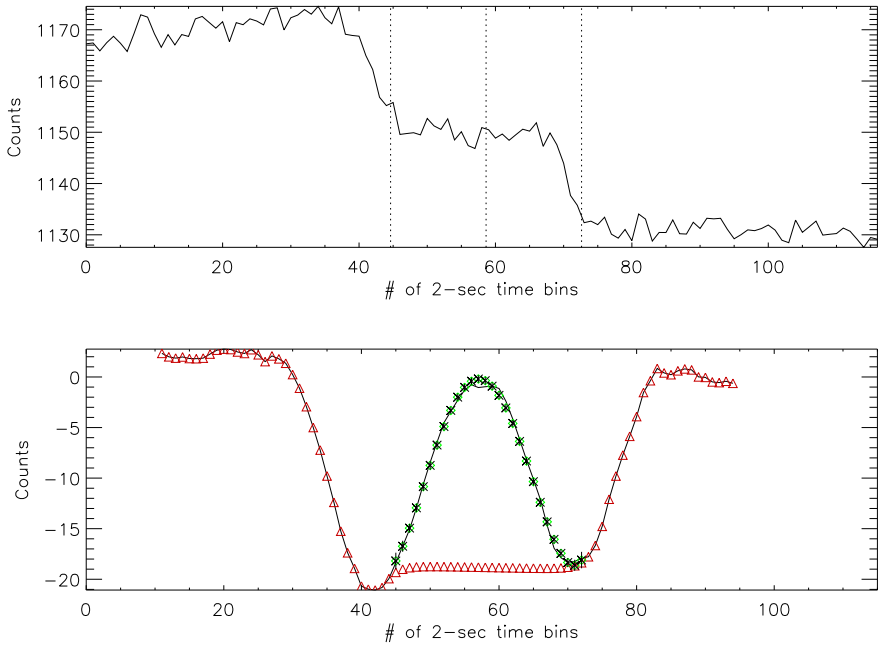

Figure 3.17: *Top*: Averaged window for 1 day for a virtual source near the Crab. Crab steps at about 40 bin and 75 bin. *Bottom*: The filtered data with the central portion fit to a polynomial (green), and the outer background portion fit to a spline function (red). Large dips from Crab steps cause calculated background level to be significantly lower than center of window, resulting in negative amplitude for virtual source.

The other systematic effect involves virtual sources at roughly the same declination as a bright source and a few degrees away in right ascension. The virtual source is close enough on the sky to the bright source so that both rise and set steps for the bright source occur inside the 4-minute window, but the virtual source and the bright source are far enough away such that when the window is filtered, the rise steps and the set steps for the bright source remain separated. Consequently, the steps from the bright source are treated as the background level. Since the background level may then be larger than the source at the occultation time, the calculated amplitude of the virtual source appears significantly negative. To reduce this effect, the polynomial fit boundaries are shifted towards the occultation time (i.e. the center of the window) to reduce the effect of the bright source on the background fit. Fig. 3.17

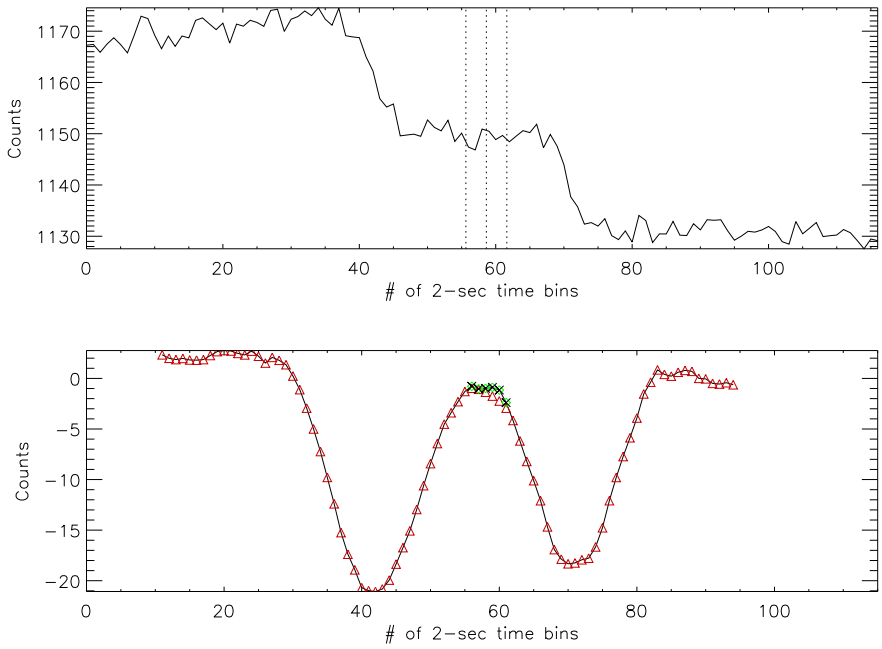

Figure 3.18: The same filtered data as previous figure, but the boundaries for the spline and polynomial fit have been changed so that the polynomial is fit over a smaller range.

demonstrates this problem by using a virtual source at $\alpha = 82.5°$, $\delta = 23.5°$, close to the Crab ($\alpha = 83.63°$, $\delta = 22.02°$). The top panel in Fig. 3.17 shows the rise and set occultation steps for the Crab for 11 days, roughly at bin 40 and bin 75. The bottom panel shows how the filtered Crab steps misrepresent the background and thus the calculated amplitude of the virtual source. Fig. 3.18 shows the how decreasing the range of the central region to $2f_a$ reduces the effect of the Crab on the fit amplitude.

3.3.2 Implementation

The EOT analysis code is written in Interactive Data Language (IDL) so initial IDEOM routines were also in IDL. The average time to process a source in IDL on the available desktops (e.g. calculating occultation times, stacking, filtering, and fitting windows) took $\sim$ 1 sec/day. At that rate, it would take $\sim$ 180 hours ($\sim$ 1 week) to process an image of the whole sky for a single day, making imaging long periods of time intractable. To reduce the processing time, the routines were translated to FORTRAN and Message Passing Interface (MPI) was incorporated so that analysis could be done using the Louisiana State University High Performance (HPC) machine Tezpur and the Louisiana Optical Network Institute (LONI) machine Queen Bee with parallel computing. Because each virtual source is independent, analysis can be done in parallel on separate processors and the results combined afterward. LSU HPC quotes Tezpur as running at 15.322 TFlops with 360 nodes with 2 dual-core 2.66 GHz Intel Xeon 64 bit processors running Red Hat Enterprise Linux (RHEL) with 4 GB of RAM (Louisiana State University High Performance Computing, 2012). LONI's Queen Bee runs at 50.7 TFlops with 680 nodes with 2 quad-core 2.33 GHz Intel Xeon 64 bit processors with RHEL and 8 GB of RAM (Louisiana Optical Network Institute, 2012). The virtual source catalog was separated into three roughly equal sections because of memory constrains. The first catalog covers declinations 0° to $+45^\circ$; the second -0.25° to -45°; and the third covers the polar caps. Analysis of an input catalog for a precession period used 80 nodes (320 processors in Tezpur or 640 processors on Queen Bee) and took $\sim$ 6 hours to complete. Thus a single precession period could be generated in $\sim$ 6 to $\sim$ 18 hours, depending on the queue time.

Chapter 4
IDEOM Results

4.1 Results

IDEOM has been applied to the first ~ 4 years of GBM CTIME data, covering August 12, 2008 to September 14, 2012, which corresponds to 28 *Fermi* orbital precession periods. An all-sky image has been generated for each precession period for three broad energy bands, 12-50 keV, 50-100 keV, and 100-300 keV. Table 4.1 shows the beginning and ending dates for each precession period in Modified Julian Date (MJD). Single precession period images for an energy band were combined by summing the intensities for a virtual source weighted by the number of occultation steps for the point during a precession period. Fig. 4.1 shows the combined all-sky significance map for the first ~ 4 years of the mission for the 12-50 keV. Fig. 4.2 shows the galactic center region in the same energy band. Contours have been over plotted at $3.5\sigma, 5\sigma, 10\sigma,$ and 20σ. The source names plotted in red with asterisks correspond to GBM sources detected $> 5\sigma$ by the EOT during the 28 precession periods while names in blue with triangles denote sources added to the GBM catalog based on imaging. Figs. 4.3-4.4 are the significance maps for the entire sky and galactic center region, respectively, for the 50-100 keV band. The source names in black with diamonds mark GBM sources found with IDEOM, but not detected by the EOT. The 100-300 keV images for the entire sky and galactic center are Figs. 4.3-4.4, respectively. Precession period 22 was excluded from the maps of the lowest energy band due to high significance fluctuations in the background. Also, time periods when the high mass X-ray binary A0535+262 was in an extremely bright

Table 4.1: *Fermi* Orbital Precession Periods

Precession Period	Beginning Day (MJD)	Ending Day (MJD)
1	54690	54743
2	54744	54796
3	54798	54851
4	54852	54905
5	54906	54958
6	54959	55012
7	55013	55066
8	55067	55120
9	55121	55174
10	55175	55227
11	55228	55281
12	55282	55335
13	55336	55389
14	55390	55442
15	55443	55496
16	55497	55550
17	55551	55604
18	55605	55650
19	55651	55704
20	55705	55757
21	55758	55811
22	55812	55864
23	55865	55917
24	55918	55971
25	55972	56024
26	56025	56077
27	56078	56130
28	56131	56184

outburst, during which it flickered, resulting in wave-like features contaminating the images were also removed. These times occurred during precession periods 9, 10, and 18. Fig. 4.7 is a significance map showing the effects of A0535+262 on the sky. The plotted contours are 2.5, 3.5, 5, 10, and 20σ. The wave-like features span over 60° in declination and roughly 90° in right ascension and would make identification of faint sources difficult. Fig. 4.8 shows the exposure all-sky map for the 12-50 keV energy band plotted in terms of the total number of detector-steps during the span of 28 precession periods, where a detector-step is the number of detectors that view a given occltation step. The minimum value is $\sim 62,000$, and the maximum value is $\sim 136,000$. The lighter colors denote regions of more detector-steps and darker regions fewer detector-steps. The plotted sources mark those sources considered "bright" and have been "boxed" as discussed 3.3.1, which has resulted in reduced exposure above and below those sources.

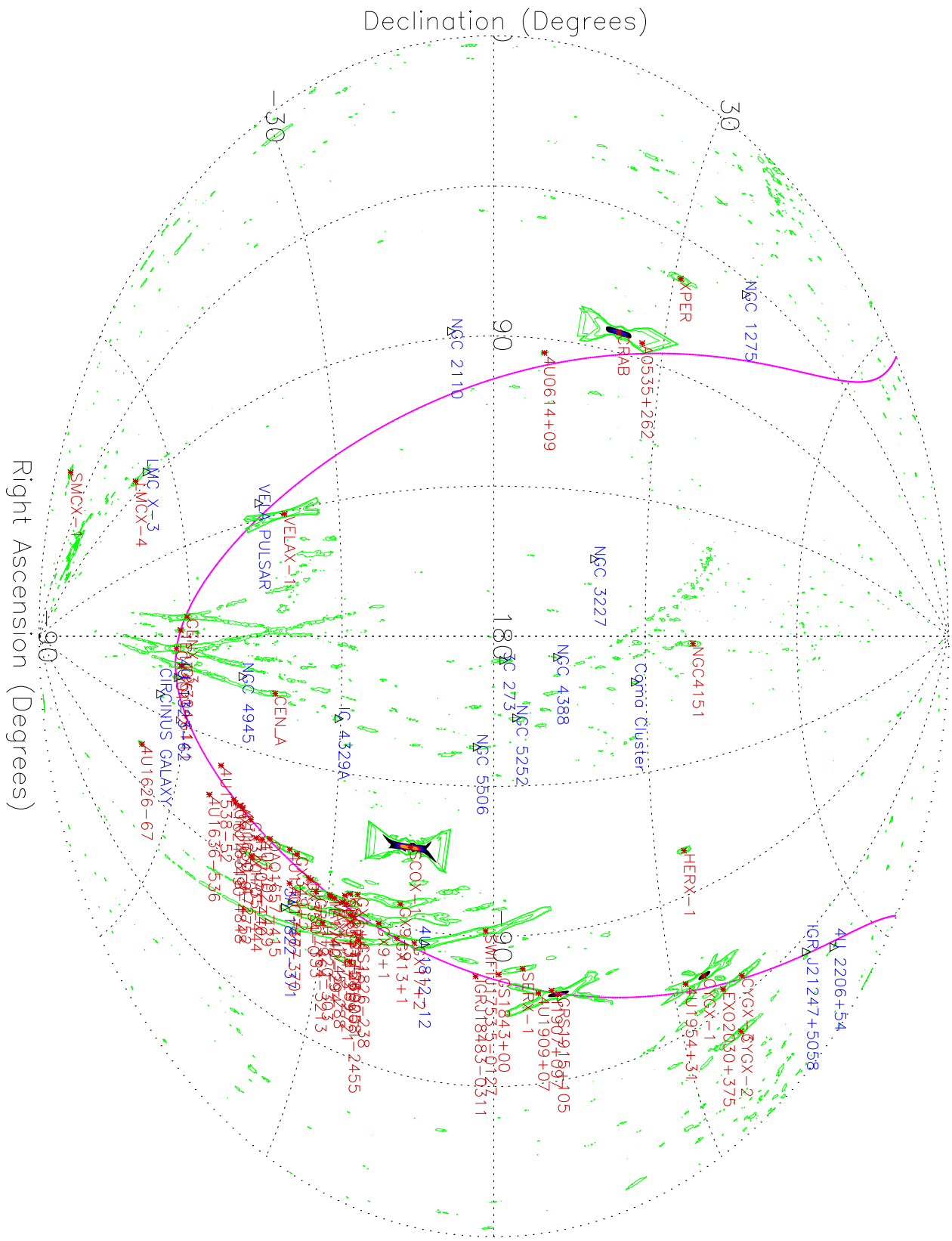

Figure 4.1: All-sky Significance Map for 12-50 keV for 28 precession periods

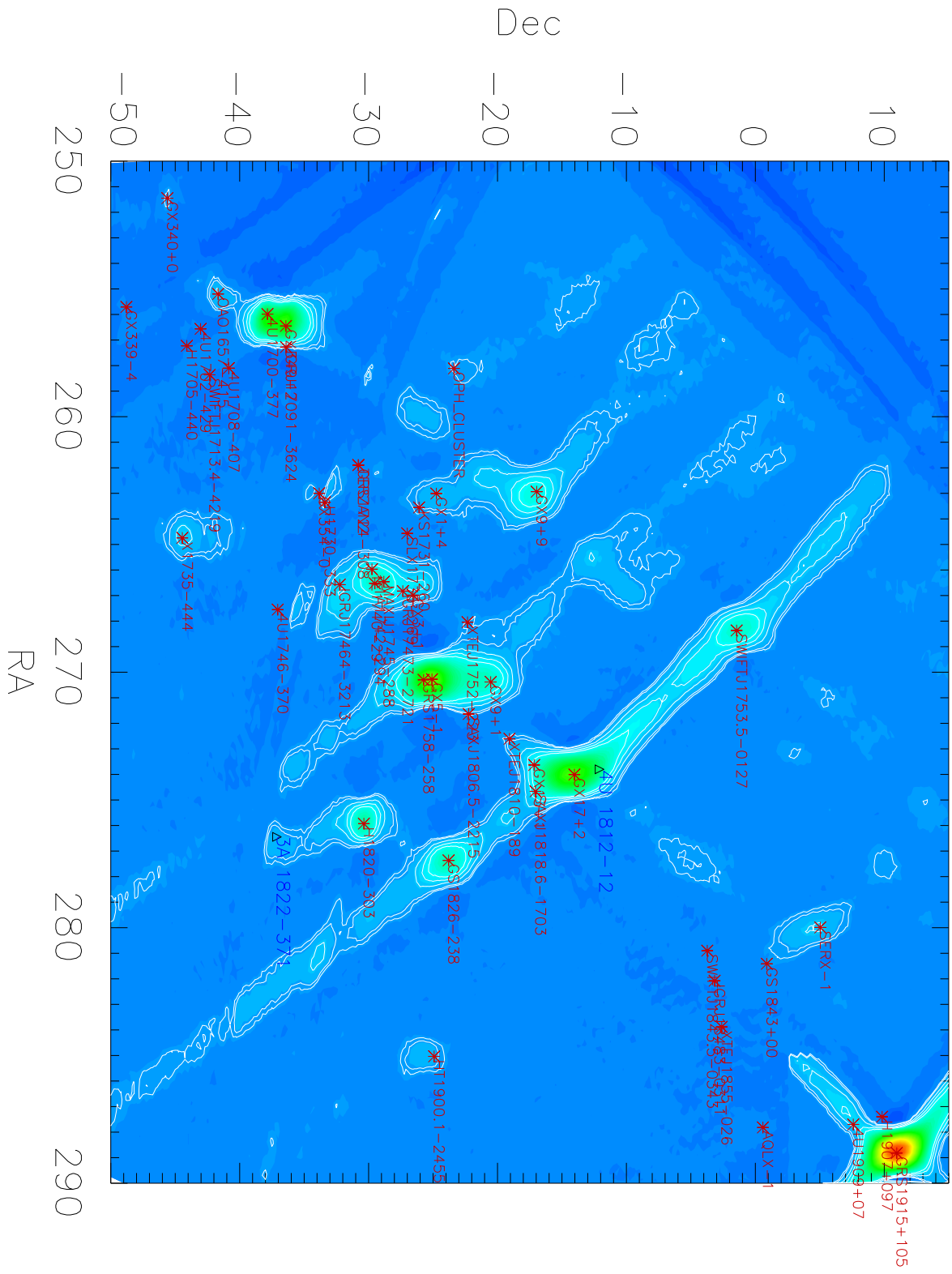

Figure 4.2: Galactic Center Region Significance Map for 12-50 keV for 28 precession periods

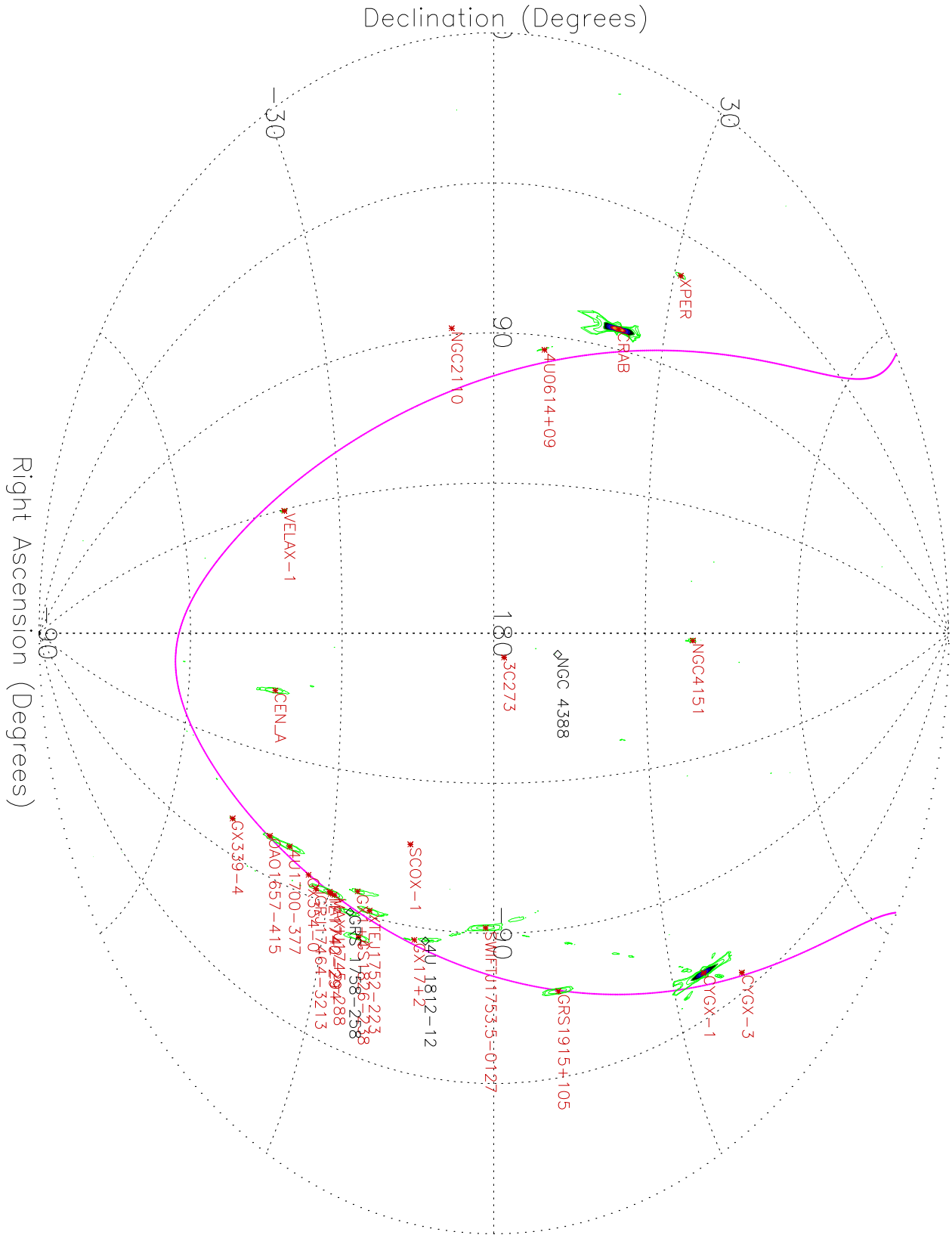

Figure 4.3: All-sky Significance Map for 50-100 keV for 28 precession periods

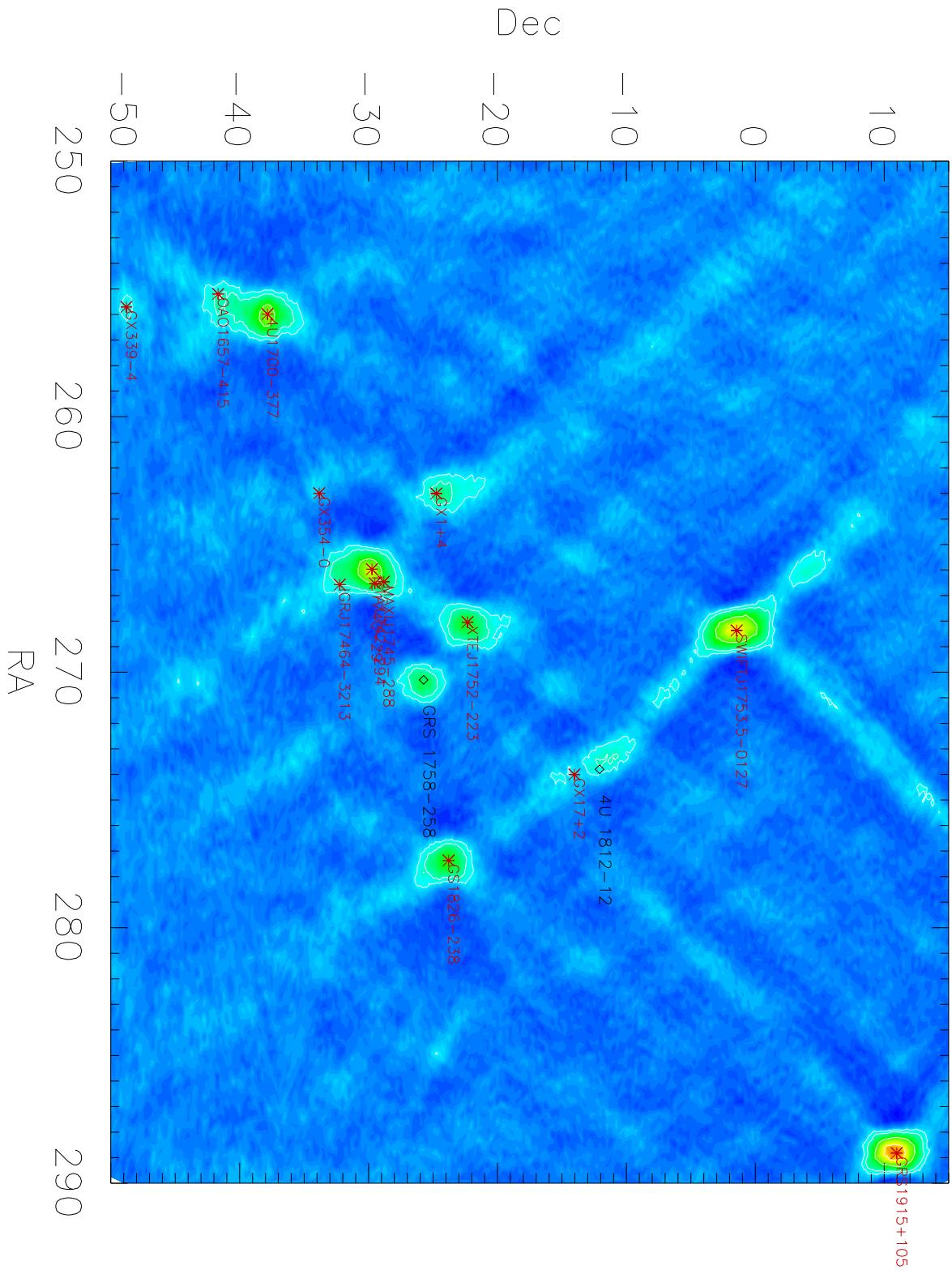

Figure 4.4: Galactic Center Region Significance Map for 50-100 keV for 28 precession periods

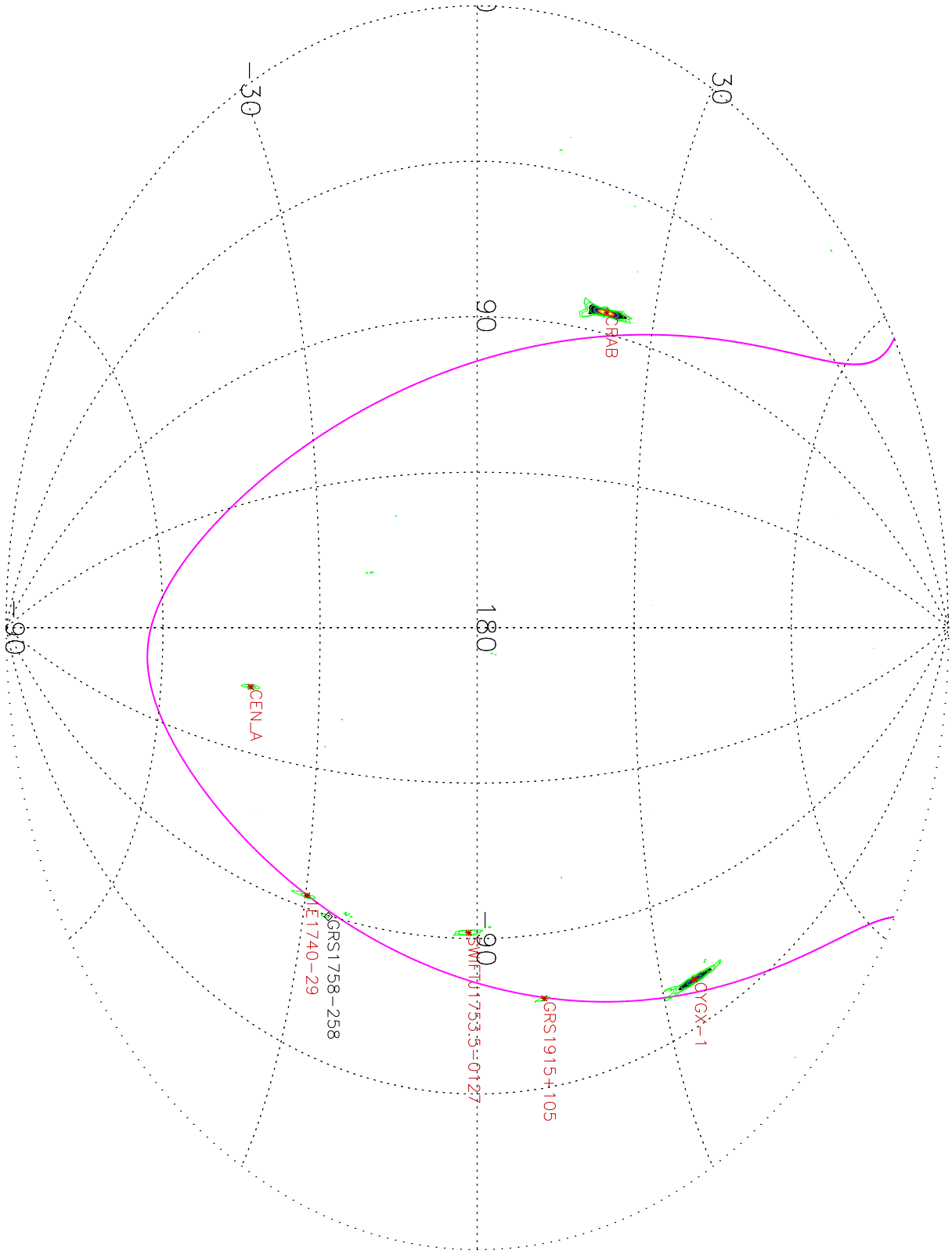

Figure 4.5: All-sky Significance Map for 100-300 keV for 28 precession periods

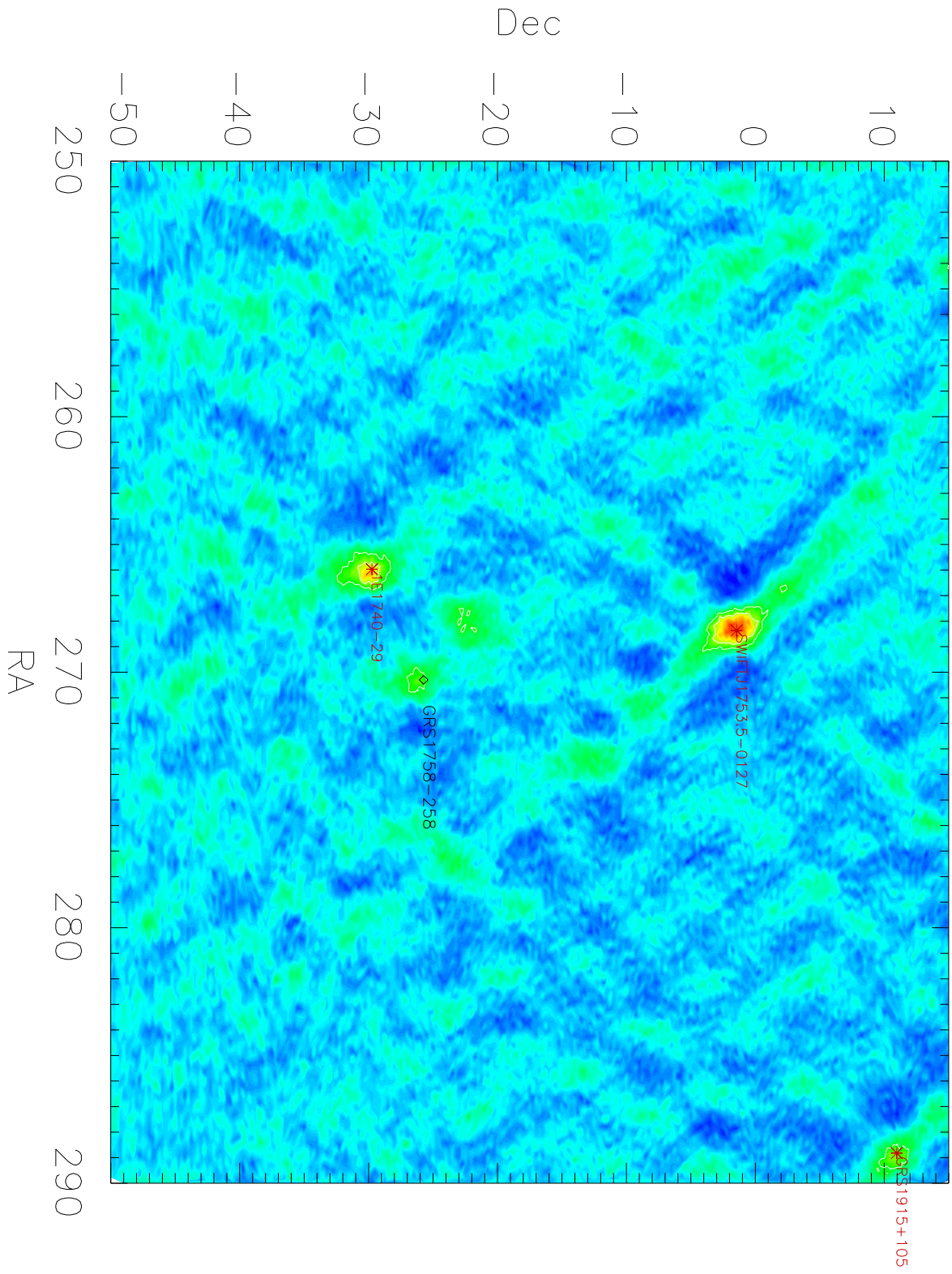

Figure 4.6: Galactic Center Region Significance Map for 100-300 keV for 28 precession periods

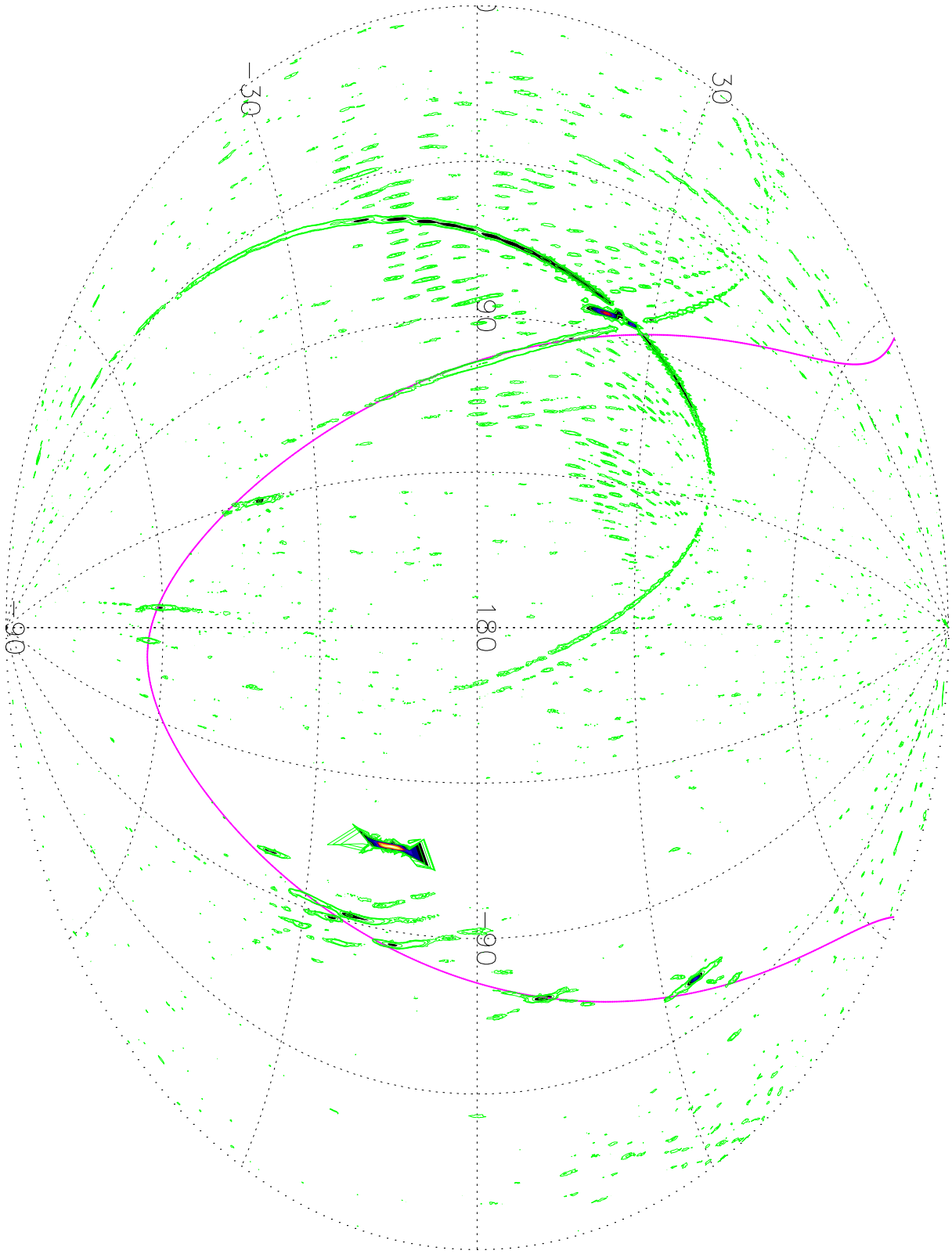

Figure 4.7: All-sky Significance Map for 12-25 keV of A0535+162 Outburst During Precession Period 10

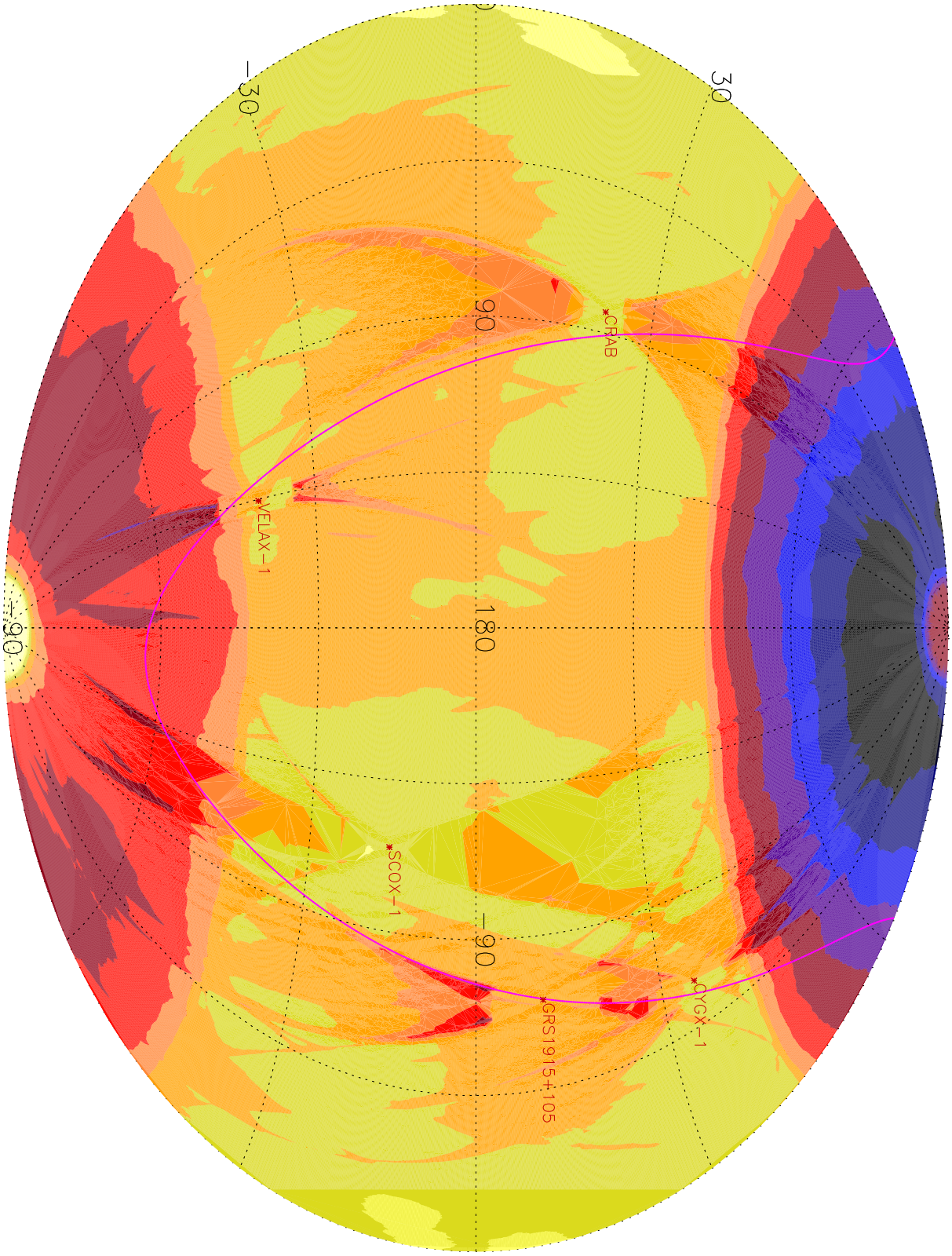

Figure 4.8: All-sky Exposure Map for 12-50 keV

Early IDEOM analysis consisted of cross-correlating features in images with *Swift*/BAT, *INTEGRAL*/SPI, and *Fermi*/LAT catalogs. A source was added when the 12-50 keV statistical significance was $> 10\sigma$. With this method, 16 sources were added to the GBM catalog. Those sources include: 3A 1822-371, NGC 2110, Circinus Galaxy, NGC 5506, LMC X-3, Vela Pulsar, 3C 273, IC 4329A, NGC 5252, NGC 3783, 4U 1812-12, 4U 2206+54, IGR J21247+5058, the Coma cluster, NGC 3227, and NGC 1275. Later analysis looked to be more systematic by searching for sources that may not be listed in those three catalogs. This process began by determining the positions for potential sources in the images through searching for points with intensities greater than 3.5σ above background. $5^\circ \times 5^\circ$ regions centered on each point were fit to a two-dimensional Gaussian. The maximum value of the fit in standard deviations above the background was taken as the source significance, and the centroid was taken to be the source position. Using the parameters of the fit, the integrated significance within a rectangle $\pm 2\sigma_{\alpha,\delta}$ of the source position was calculated, where σ_α and σ_δ are the calculated widths of the fitted Gaussian.

Candidate sources were selected from the list of potential sources by requiring that the product of the peak significance and the integrated significance divided by the statistical error for the virtual source be > 10. This statistic is to ensure that virtual source selection was not biased by individual "hot" pixels. The angular distance between potential sources was required to be $> 1.5^\circ$ from each other to reduce problems from source crowding. For bright sources (e.g. Crab, Sco X-1, and Vela X-1), potential sources from 0.5° to $\sim 5^\circ$ away from the known source location were removed to eliminate source crowding due to imaging artifacts, such as "arms". In the 12-50 keV band, potential sources were manually removed that lay along the "arms" of Cen X-3, GX 301-2, GX 304-1, and the long feature starting at SWIFT J1753.5-0127 and ending around $(280^\circ, -60^\circ)$. Candidate sources for an image are used in a temporary input catalog and analyzed using the EOT to determine fluxes and significances. The cumulative images for each energy band were searched to look for candidate sources. Tables 4.2 - 4.4 contain the list of sources identified by IDEOM and

verified by EOT.

Table 4.2: Sources Detected by IDEOM in the 12-50 keV Band

Measured Position (Degrees)	Source Name	Known Position (Degrees)	Position Error (Degrees)
(19.37, -73.50)	SMC X-1	(19.27, -73.43)	0.07
(58.92, 31.00)	X PER	(58.85, 31.05)	0.08
(83.59, 22.00)	CRAB	(83.63, 22.01)	0.05
(83.59, -66.00)	LMC X-4	(83.20, -66.36)	0.40
(94.16, 9.00)	4U 0614+09	(94.28, 9.13)	0.18
(135.63, -40.75)	VELA X-1	(135.52, -40.55)	0.21
(170.59, -60.50)	CEN X-3	(170.31, -60.62)	0.18
(176.79, -62.00)	1E 1145.1-6141	(176.86, -61.95)	0.06
(182.40, 39.25)	NGC 4151	(182.65, 39.41)	0.25
(186.68, -63.00)	GX 301-2	(186.65, -62.77)	0.23
(187.34, 1.75)	3C 273	(187.27, 2.05)	0.31
(195.43, -61.50)	GX 304-1	(195.32, -61.60)	0.11
(201.27, -43.50)	CEN A	(201.36, -43.01)	0.49
(244.99, -16.00)	SCO X-1	(244.98, -15.64)	0.36
(248.25, -67.50)	4U 1626-67	(248.07, -67.46)	0.08
(254.57, 35.50)	HER X-1	(254.45, 35.34)	0.18
(255.78, -40.50)	OAO 1657-415	(255.19, -41.67)	1.25
(256.06, -37.00)	GX 349+2	(256.45, -36.41)	0.66
(256.39, -39.00)	4U 1700-377	(255.98, -37.84)	1.20
(261.81, -30.75)	GRS 1724-308	(261.89, -30.80)	0.09
(262.88, -25.00)	GX 1+4	(263.00, -24.74)	0.28
(263.02, -17.75)	GX 9+9	(262.93, -16.96)	0.79
(263.36, -32.75)	GX 354-0	(263.35, -33.39)	0.64
(264.41, -43.75)	X1735-444	(264.74, -44.45)	0.74
(266.55, -28.50)	MAXI J1745-288	(266.46, -28.82)	0.33
(266.74, -30.00)	1E 1740-29	(265.97, -29.74)	0.72
(266.82, -31.50)	IGR J17464-3213	(266.57, -32.24)	0.77
(268.71, -2.25)	SWIFT J1753.5-0127	(268.36, -1.45)	0.87
(270.33, -25.00)	GX 5-1	(270.27, -25.08)	0.10
(270.57, -20.00)	GX 9+1	(270.38, -20.53)	0.56
(273.48, -12.25)	4U 1812-12	(273.80, -12.08)	0.35
(273.82, -17.25)	GX 13+1	(273.63, -17.15)	0.20

Continued on next page

Table – *Continued from previous page*

Measured Position (Degrees)	Source Name	Known Position (Degrees)	Position Error (Degrees)
(273.93, -14.25)	GX 17+2	(274.00, -14.03)	0.23
(275.93, -30.50)	H1820-303	(275.92, -30.36)	0.13
(276.83, -36.25)	3A 1822-371	(276.44, -37.10)	0.91
(277.29, -23.00)	GS 1826-238	(277.36, -23.79)	0.80
(280.02, 4.25)	SER X-1	(279.99, 5.03)	0.79
(285.06, -25.75)	HT 1900.1-2455	(285.03, -24.92)	0.83
(288.81, 11.00)	GRS 1915+105	(288.82, 10.97)	0.04
(299.70, 35.25)	CYG X-1	(299.59, 35.20)	0.10
(308.07, 41.00)	CYG X-3	(308.10, 40.95)	0.05
(308.19, 37.50)	EXO 2030+375	(308.06, 37.63)	0.17
(325.98, 38.25)	CYG X-2	(326.17, 38.32)	0.16

4.1.1 Comparison with GBM EOT Results

The sources detected by IDEOM in the 12-50 keV band are listed in Table 4.2. In this energy range, the EOT detects 67 sources while IDEOM finds 43, two of which are not detected by the EOT. Of the 26 sources not found by IDEOM, 11 were close to a brighter source (within a few degrees) and thus could not be separated, 12 did not show a feature above 3.5σ in the image, two did not meet the detection threshold of > 10 for the test statistic, and one (A0535+262) lacked image data during outburst and was not expected to be detected. A sensitivity limit for IDEOM in the 12-50 keV band can be estimated based on the EOT fluxes for the sources where no feature was seen in the image. There were 10 sources with an average flux < 25 mCrab detected by the EOT. Only three of those were found with IDEOM, placing the sensitivity limit at ~ 25 mCrab for isolated sources. For the 18 sources with average fluxes between 25 mCrab and 50 mCrab, six sources were missed by IDEOM. These sources are all located in low sensitivity regions. Two (4U 1702-429 and 4U 1705-472) lie close to a Sco X-1 arm thus decreasing the number of usable occultation steps. The other

Table 4.3: Sources Detected by IDEOM in the 50-100 keV Band

Measured Position (Degrees)	Source Name	Known Position (Degrees)	Position Error (Degrees)
(58.92, 31.00)	X PER	(58.85, 31.05)	0.08
(83.59, 22.00)	CRAB	(83.63, 22.01)	0.05
(94.42, 8.00)	4U 0614+09	(94.28, 9.13)	1.15
(135.30, -40.75)	VELA X-1	(135.52, -40.55)	0.26
(182.40, 39.25)	NGC 4151	(182.65, 39.41)	0.25
(185.86, 10.50)	NGC 4388	(186.45, 12.66)	2.24
(187.61, 2.00)	3C 273	(187.27, 2.05)	0.34
(201.48, -43.25)	CEN A	(201.36, -43.01)	0.25
(255.56, -48.75)	GX 339-4	(255.70, -48.78)	0.10
(255.88, -38.50)	4U 1700-377	(255.98, -37.84)	0.66
(262.90, -24.75)	GX 1+4	(263.00, -24.74)	0.10
(265.96, -30.25)	1E 1740-29	(265.96, -29.74)	0.51
(266.07, -31.75)	IGR J17464-3213	(266.57, -32.24)	0.65
(266.49, -28.25)	MAXI J1745-288	(266.46, -28.82)	0.57
(268.06, -23.00)	XTE J1752-223	(268.04, -22.32)	0.68
(268.34, -1.50)	SWIFT J1753.5-0127	(268.36, -1.45)	0.06
(270.36, -26.00)	GRS 1758-258	(270.30, -25.73)	0.27
(273.77, -13.00)	4U 1812-12	(273.80, -12.08)	0.92
(274.03, -14.75)	GX 17+2	(274.00, -14.03)	0.71
(277.49, -24.00)	GS 1826-238	(277.36, -23.79)	0.23
(288.82, 10.75)	GRS 1915+105	(288.82, 10.97)	0.22
(299.70, 35.00)	CYG X-1	(299.59, 35.20)	0.22
(307.89, 40.75)	CYG X-3	(308.10, 40.95)	0.26

Table 4.4: Sources Detected by IDEOM in the 100-300 keV Band

Measured Position (Degrees)	Source Name	Known Position (Degrees)	Position Error (Degrees)
(83.59, 22.00)	CRAB	(83.63, 22.01)	0.05
(201.34, -43.00)	CEN A	(201.36, -43.01)	0.03
(266.25, -30.25)	1E 1740-29	(265.96, -29.74)	0.57
(268.34, -1.50)	SWIFT J1753.5-0127	(268.36, -1.45)	0.06
(270.41, -26.50)	GRS 1758-258	(270.30, -25.73)	0.78
(288.81, 11.00)	GRS 1915+105	(288.82, 10.97)	0.04
(299.70, 35.00)	CYG X-1	(299.59, 35.20)	0.22

four sources are farther away from the Sco X-1 arm, but they are at lower declinations so are not occulted during part of a precession period and also lose some occultation steps due to interference from Sco X-1. Thus for sources that are not isolated, the sensitivity limit is closer to 50 mCrab For the two GBM sources found by IDEOM, 3C 273 and GRS 1724-308 have an EOT significances of 4.8σ and 4.7σ, respectively. The corresponding IDEOM significances are 5.0σ and 13.5σ. The EOT and IDEOM fluxes for 3C 273 are consistent within the errors. For GRS 1724-308, the IDEOM flux is 3.5 times larger than the EOT flux, likely due to contributions from source interference in the crowded galactic center region. Using the position error between the measured source position and the known source position, the positional accuracy in the 12-50 keV band is $\Delta\theta \sim 0.40^{\circ}$

Table 4.3 shows the sources detected by IDEOM in the 50-100 keV band. In this energy range GBM-EOT detects 25 sources while IDEOM detects 23 sources, three of which are in the GBM catalog but not detected. Three of the five sources not detected by IDEOM have no feature in the image (NGC 2110, Sco X-1, and GX 354-0). The other two sources were close to a detected source and unable to be separated by IDEOM (OAO 1657-415 and 1A 1742-294). The average flux of the three undetected sources without an image feature is less than 22 mCrab, suggesting that the sensitivity in the 50-100 keV energy band is roughly 22 mCrab. The three GBM sources detected by IDEOM, but not EOT were NGC 4388, GRS 1758-258, and 4U 1812-12. The EOT sensitivity is low for sources close together as the number of usable occultation steps for each source is reduced. IDEOM does not exclude occultation steps for sources close together on the sky when generating an image allowing GRS 1758-258 ($\sim 0.75^{\circ}$ away from GX 5-1) and 4U1812-12 ($\sim 1.9^{\circ}$ away from GX 17+2) to be detected by IDEOM and not by the EOT. *INTEGRAL* observations have shown spectra of GRS 1758-258 and 4U 1812-12 with significant flux out to 100 keV (Pottschmidt et al., 2008; Tarana et al., 2006) that the other two sources do not possess (Paizis et al., 2005; Mainardi, et al., 2010; Migliari, et al., 2007), which is in agreement with results from IDEOM. The third source, NGC 4388 is detected at 5.4σ by IDEOM and 4.7σ by the EOT and with

flux measurements consistent within the errors between the two methods. The calculated position accuracy in this energy band is $\Delta\theta \sim 0.47°$.

Table 4.4 shows the sources found by IDEOM in the 100-300 keV band. In this energy range EOT detected six sources. IDEOM found all six of these sources and also detected GRS 1758-258. The lowest average flux is $\sim$ 54 mCrab for GRS 1758-258 at 9.0σ. The EOT significance for this source is 1.6σ with a flux of 58 mCrab. The difference in significance is due to source crowding and thus fewer occultation measurements. There are two sources detected by IDEOM between 3.5σ and 5σ. The sources are 3C 273 with an average flux of $\sim$ 20 mCrab and a significance of 3.9σ and XTE J1752-223 with an average flux of $\sim$ 32 mCrab and a significance of 4.6σ. Using XTE J1752-223, the 4-year sensitivity can be estimated to be between 32 and 54 mCrab. The lack of unaccounted-for sources at these energies suggests that the catalog is complete down to roughly 20 mCrab in the 100-300 keV band and that the discrepancies between the EOT and EBOP analyses of BATSE occultation data are likely due to inaccuracies in the EBOP background model. The calculated position accuracy in the 100-300 keV band is $\Delta\theta \sim 0.25°$.

Chapter 5
Sources Detected by GBM and LAT

5.1 Introduction

With the GBM catalog complete, one can look at combined results from GBM and LAT analysis. This is the first such analysis using these combined data sets. By combining GBM and LAT monitoring, one can study roughly 7 decades of energy from ($\sim$ 10 keV to $\sim$ 100 GeV). This capability allows for studying source variability and spectral features in hard X-rays and high-energy γ-rays to better understand the emission mechanisms at work. After comparing the GBM catalog and the second LAT catalog, four persistent sources have been detected by both instruments: NGC 1275, 3C 273, Cen A, and the Crab. Spectra for each source have been generated using 4 years of broad band GBM CTIME data, 2 years of data from LAT 2FGL catalog (Nolan et al., 2012), 1.5 years *INTEGRAL* data for NGC 1275 (Eckert & Paltani, 2009), 5.5 years of *INTEGRAL* data for the Crab (Jourdain & Roques, 2009), and $\sim 5 years$ of data from *CGRO*/COMPTEL (0.75-30 MeV) (Schönfelder et al., 2000).

NGC 1275

NGC 1275 is an elliptical galaxy in the middle of the Perseus galaxy cluster. Observations from the first *High Energy Astronomy Observatory* (*HEAO 1*) satellite showed emission at energies from 10-93 keV with no obvious variability (Primini et al., 1981). Later observations with *CGRO*/OSSE failed to detect NGC 1275 in the 50-500 keV energy range with upper

limits significantly below the fluxes observed during earlier missions (Osako et al., 1994), indicating long-term variability. *INTEGRAL* has detected the source at 3-20 keV with JEM-X and at 20-120 keV with IBIS/ISGRI. The flux was seen to vary but found to be lower by roughly a factor of 3 when compared to the extrapolated power law model with a photon index of $\Gamma \sim 2$ from *Chandra* data (Sanders et al., 2005). Eckert & Paltani (2009) fit the *INTEGRAL* data from March 2003 to August 2004 with a model of a two-temperature plasma with a central temperature of $kT = 3$ keV plus an AGN contribution. The two-temperature model is required to model the effects of the cool Perseus cluster core and the hotter outer region of the cluster, and the AGN contribution is modeled by a power law with $\Gamma = 1.65$ to account for the nonthermal high energy flux from NGC 1275 at the center of the cluster (Churazov et al., 2003).

At higher energies, *CGRO*/EGRET observation resulted in only upper limits (Reimer et al., 2003) while the *Fermi*/LAT detects NGC 1275 with variations on monthly timescales with an average best fit power law spectral index of $\Gamma = 2.13$ (Kataoka et al., 2010). The LAT data have also been fit using a cut-off power law model resulting in a better χ^2 with $\Gamma = 2.07$ and $E_C = 42.2$ GeV. The presence of synchrotron emission at radio wavelengths suggests that relativistic electrons are present in the jet. The hard X-rays and γ-rays then are due to inverse Compton scattering of the electrons with the cosmic microwave background and the infrared photon flux (Abdo et al., 2009). Fig. 5.1(a) shows the LAT power law spectrum from Kataoka et al. (2010) extrapolated down to GBM energies. The LAT power-law spectrum extended down to 12-25 keV falls well below the *INTEGRAL* data points from Eckert & Paltani (2009) but fits the GBM data (which lie nearly an order of magnitude below the *INTEGRAL* points) reasonably well. The GBM data do not show any significant variability during the mission so far, based on the light curves published on the GBM Occultation Project website[1].

[1]http://heastro.phys.lsu.edu/gbm/

3C 273

The bright, close FSRQ 3C 273 has been a frequent target of X-ray and γ-ray observations since the 1970s. Observations with the the Cosmic X-ray Experiment (CXE) on board HEAO 1 in the 2-60 keV energy range are best fit with a power law of $\Gamma = 1.41$ (Worrall et al., 1979) while the Hard X-ray/Low Energy Gamma Ray Experiment measurements on HEAO 1 in the 13-180 keV energy range gave a slope of $\Gamma = 1.67$ (Primini et al., 1979). With *INTEGRAL*, Cournoiser et al. (2003) fit the 25-100 keV IBIS/ISGRI spectrum to a power law with $\Gamma = 1.95 \pm 0.2$ and the 20-200 keV SPI spectrum to a power law with $\Gamma = 1.66 \pm 0.28$. Later *INTEGRAL* and *XMM-Newton* (0.1-15 keV) observations (Chernyakova et al., 2007) confirmed a softening of the power law spectrum with time, reporting a photon index $\Gamma = 1.82 \pm 0.01$. Such a soft spectrum can be produced by inverse Compton emission from relativistic electrons, but the harder spectrum observed by earlier experiments cannot be produced that way (Lightman & Zdziarski, 1987) unless there is a significant density of protons in the γ-ray emission region Chernyakova et al. (2007).

COS B observations at γ-ray energies (50-800 MeV) showed a power law of $\Gamma = 2.5$ (Bignami et al., 1981). OSSE detected flux variability on the timescales of months from June 1991 to Jan 1993, and the data were well fit to a power law with $\Gamma = 1.71$ (Johnson et al., 1995). When these observations were combined with contemporaneous observations from COMPTEL and EGRET, the data were best fit with a broken power law model with a $\Gamma_1 = 1.7, \Gamma_2 = 1.4$, and a break energy $E_B \sim 1$ MeV. Additional COMPTEL and EGRET observations showed spectral hardening above a few MeV when the source brightened (von Montigny et al., 1997; Collmar et al., 2000) suggesting that the high-energy (above a few MeV) emission is predominately produced by a different mechanism, potentially caused by inverse Compton scattering with photons from the accretion disk while the lower energy emission produced from inverse Compton scattering from the jet. *Fermi*/LAT has observed variations in the photon index ranging from $\Gamma = 2.4$ to 3.3 and also shown a clear hardening of the spectrum at times when the flux increases (Soldi, Beckmann, & Turler, 2009). The

emission has been modeled by synchrotron self-Compton, external Compton, and proton-induced cascade models, and von Montigny et al. (1997) has fit the high-energy spectrum satisfactorily with an empirical model of the form

$$F(E) = N\frac{(E/E_B)^{-\Gamma_1}}{1+(E/E_B)^{\Gamma_2}}. \tag{5.1}$$

The synchrotron self-Compton model attempts to describe the X-ray and γ-ray spectrum through the Compton upscattering of synchrotron photons by the synchrotron emitting electrons (Jones et al., 1974). The external Compton model looks to explain the inverse Compton scattering with photons from outside the synchrotron region (e.g. the disk) (Pacciani et al., 2009), and the proton-induced cascade model seeks to explain the γ-rays as the result of cascades from ultrarelativistic protons colliding with synchrotron photons resulting in pair production and pion production (Mannheim & Biermann, 1992; von Montigny et al., 1997). Standard models can often fit broad band data equally well requiring short term variability correlations across wavelengths to differentiate between models (von Montigny et al., 1995). Also, the proton induced cascade model should produce neutrinos which are not expected from either of the synchrotron self-Compton or external Compton models (Mannheim, 1993).

The GBM light curves show distinct variability over the energy range 12-300 keV. Fig. 5.1(b) shows the 4-year average GBM spectrum together with the LAT and COMPTEL data and the von Montigny et al. (1997) model with $\Gamma_1 = 0.7, \Gamma_2 = 0.8$, and $E_B = 2.36$ MeV.

Cen A

Cen A is one of the brightest AGN detected from radio energies up to the TeV range (Aharonian et al., 2009) and ultra-high energy cosmic rays (> 60 EeV) by Auger (Abraham et al., 2009). Gamma-rays are produced by the jet in the central core and by Compton scattering of microwave and infrared-optical photons in the giant radio lobes. At hard X-ray energies,

Ginga and balloon-flight observations revealed a power law fit with a slope of $\Gamma \sim 1.8$ with a possible break at ~ 180 keV (Miyazaki et al., 1996). OSSE, COMPTEL, and EGRET observations during an intermediate emission state showed a three-segment broken power law with breaks at $E_1 = 150$ keV and $E_2 = 16.7$ MeV and slopes of $\Gamma_1 = 1.74, \Gamma_2 = 2.3$ and, $\Gamma_3 = 3.3$, while a fit during a low emission state showed breaks at $E_1 = 140$ keV and $E_2 = 590$ keV and slopes of $\Gamma_1 = 1.73, \Gamma_2 = 2.0$ and, $\Gamma_3 = 2.6$ (Steinle et al., 1998). BATSE Earth occultation data were fit with a slope of $\Gamma = 1.84$ and no evidence of a break out to 1 MeV (Wheaton et al., 1996). INTEGRAL observations by Beckmann et al. (2011) are well fit to an absorbed cut-off power-law model with $\Gamma = 1.73$ and $E_C = 434$ keV. The third EGRET catalog reports a power-law fit with $\Gamma = 2.58$ (Hartman et al., 1999). LAT measurements show a power-law fit with $\Gamma = 2.67$ (Abdo et al., 2010a), consistent with previous measurements at these energies. The observations from LAT energies through the radio can be fit with a synchrotron/synchrotron self-Compton model with a single emission region (Abdo et al., 2010a) or by a combined lepto-hadronic model in which the hard X-ray/soft γ-ray emission is produced by a combination of electron synchrotron radiation, proton synchrotron, and inverse Compton emission (Reynoso et al., 2011). In Fig. 5.1(c) the Reynoso et al. (2011) lepto-hadronic model fits well to the LAT, COMPTEL, and GBM data over the range from 12 keV to 100 GeV.

Crab

Although the Crab supernova remnant has long been considered a "standard candle" at X-rays up to 100 keV (Toor & Seward, 1974), BATSE (Ling & Wheaton, 2003) suggested flux and spectral variability in the 35-300 keV energy range on weekly timescales, but showed long-term average spectra consistent with a broken power law with $\Gamma \sim 2.1$ and $\Gamma \sim 2.4$ and a break at ~ 100 keV. GBM, *INTEGRAL*, *RXTE*, and *Swift* data have shown that the 15-100 keV flux varies by several percent per year on a timescale of ~ 3 years (Wilson-Hodge et al., 2011). GBM has presented an average spectrum best fit by a bro-

ken power law model with $\Gamma_1 = 2.057 \pm 0.01$, $\Gamma_2 = 2.36 \pm 0.05$ and a break energy at 98 ± 9 keV (Wilson-Hodge et al., 2012). *INTEGRAL* (Jourdain & Roques, 2009) fit ~ 5.5 years of SPI data to a broken power law spectrum covering 20 keV to 6 MeV with slopes $\Gamma_1 = 2.07$ and $\Gamma_2 = 2.23$ and a break energy fixed at 100 keV. When the break energy is left as a free parameter, $\Gamma_1 = 2.04$ and $\Gamma_2 = 2.18$ with a break energy at 62 keV.

COMPTEL and EGRET observed to the Crab to be variable over the 1-150 MeV energy range and showed that emission up to $\sim$ 100 MeV is due to synchrotron radiation with higher energy emission due to inverse Compton scattering (De Jager et al., 1996). The LAT detected no variability on monthly timescales during the beginning months of the mission (Abdo et al., 2010b), but reported two flares above 100 MeV during February 2009 and September 2010 with no correlated variability seen at other wavelengths (Abdo et al., 2011). Fig. 5.1(d) shows the *INTEGRAL* (red dashed) and GBM (solid black) models extended to 100 GeV together with results from COMPTEL and *Fermi*/LAT. The GBM broken power law spectrum provides excellent agreement up to 100 GeV.

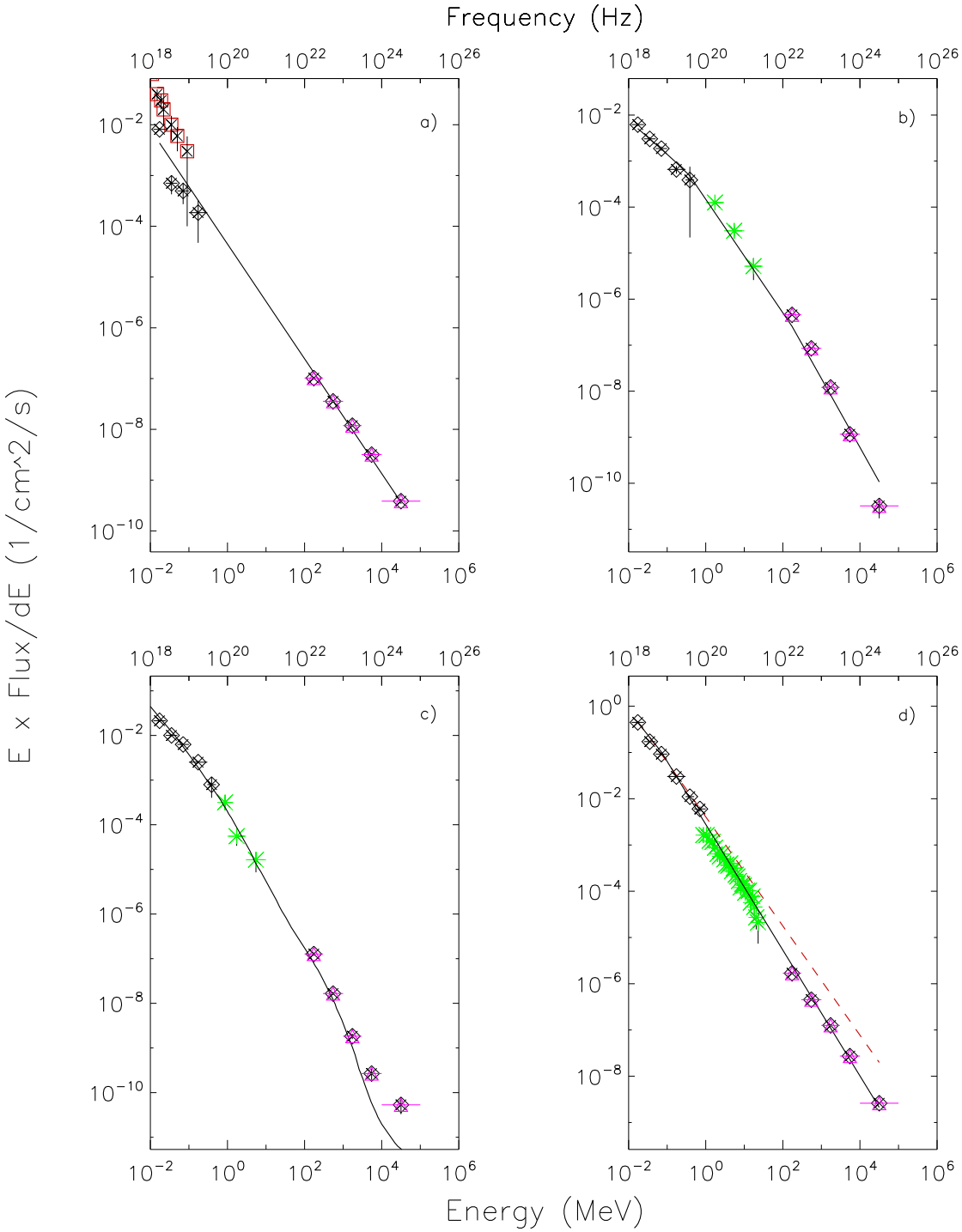

Figure 5.1: *INTEGRAL* (red squares), GBM (black diamonds), COMPTEL (green asterisks) LAT (magenta triangles) (a) NGC 1275 spectrum with *INTEGRAL*, GBM, and, LAT data and the Kataoka et al. (2010) power law spectrum extrapolated from LAT energies down to 12 keV. (b) 3C 273 spectrum with model of the form presented von Montigny et al. (1997) overplotted. (c) Cen A spectrum with lepto-hadronic model from Reynoso et al. (2011) shown. (d) Crab spectrum with GBM 3 year average spectrum (Wilson-Hodge et al., 2012) overplotted in (black) solid line, and *INTEGRAL*/SPI spectrum (Jourdain & Roques, 2009) in (red) dashed line.

Chapter 6
Transient Search

6.1 Introduction

The hard X-ray/soft γ-ray sky is extremely variable with source intensities varying on timescales of fractions of a second to years. As discussed in Chap. 2, the wide field of view of GBM allows the EOT to monitor numerous sources multiple times a day. With this capability, GBM can observe known sources for transient events throughout the duration of the event from outburst until return to quiescence, as well as monitor the other sources in the catalog. Also, once a source has been added to the input catalog, a light curve can be generated dating back to the beginning of the mission in order to search for previous transient events that may have been missed. An algorithm has been developed to systematically search through the GBM light curves for flares or transient events from known sources.

6.2 Transient Search Algorithm

The algorithm works by first calculating the sliding average for a light curve using 5-day, 9-day, and 19-day binning for the 12-50 keV, 50-100 keV, 100-300 keV, and 300-500 keV energy ranges. Based on the sensitivity plot in Fig. 2.6, the 1-day 3σ sensitivity in the 12-25 keV band is $\sim$ 150 mCrab so multiple days have been averaged together to improve the sensitivity of the search to $<$ 100 mCrab at the expense of time resolution. To find outbursts in the data, consecutive sliding average bins with a statistical significance greater than 3σ were joined together as a single transient event. The weighted average of each event

was calculated, and those with a statistical significance $> 7\sigma$ kept. For occasions when beginning/ending times for an outburst depended on the size of the sliding average bins, the period with the highest significance was selected. Next, the systematic errors listed in Table 2.1 were added in quadrature to the statistical errors to calculate the total significance with a threshold at 7σ. The systematic error for the 12-50 keV band was estimated using the same method outlined in 2.3.3 and found to be 2.7 mCrab. For each event the significance above the median flux of the source was computed to remove persistent sources and to look for outbursts from active sources. Transient events with significance $> 6\sigma$ were considered to be significant detections.

6.3 Results

The day ranges for transient events detected during the first 4 years of GBM analysis in the 12-50 keV, 50-100 keV, and 100-300 keV bands are listed in Table 6.1. The table contains 168 transient events from 65 sources with seven events detected above 50 keV, one event detected above 100 keV (XTE J1752-223), and no events detected above 300 keV. Three sources were found to have relatively short flares (< 10 days) that occurred during two A0535+262 flares (MJD 55165-55204 and 55930-55938) suggesting that the measured flux from these sources is biased by A0535+262. This conclusion is further supported by the lack of features during the corresponding times in the *Swift*/BAT data for these sources. These sources are marked by an asterisk.

Table 6.1: Transient Events Detected by GBM-EOT

Source Name	12-50 keV Day Range (MJD)	50-100 keV Day Range (MJD)	100-300 keV Day Range (MJD)
SMC X-1	55130-55147		
	55183-55208		
	55356-55368		
3A 0114+650	55746-55769		

Continued on next page

Table – *Continued from previous page*

Source Name	12-50 keV Day Range (MJD)	50-100 keV Day Range (MJD)	100-300 keV Day Range (MJD)
4U 0115+634	55737-55758		
PKS 0215+015	55985-55993		
GK Per	55258-55344		
V0332+53	54769-54791		
	55160-55172		
	55196-55207		
PKS 0347-211	55224-55234		
	56030-56040		
PKS 0420-01	55258-55267		
LS V +44 17	55285-55303		
LMC X-4	54974-55016		
A0535+262	54932-54946		
	55039-55067		
	55165-55204	55181-55189	
	55277-55311		
	55391-55422		
	55486-55497		
	55596-55640		
	55930-55938		
NGC 2110*	55190-55205		
HESS J0632+057*	55931-55938		
MXB 0656-072	54727-54752		
MG2 J071354+193	56069-56073		
PKS 0805-07*	55938-55951		
S4 0917+44	56015-56027		
4C +55.17	55136-55144		
GRO J1008-57	54913-54923		
	55161-55169		
	55657-55668		
	55909-55928		
TXS 1013+054	55982-55990		
Mrk 421	55236-55263		
A1118-61	54836-54857		

Continued on next page

Table – *Continued from previous page*

Source Name	12-50 keV Day Range (MJD)	50-100 keV Day Range (MJD)	100-300 keV Day Range (MJD)
Cen X-3	55113-55185		
	55186-55265		
	55420-55448		
	55474-55511		
	55816-55828		
	55829-55938		
NGC 3783	55983-55992		
1FGL J1227.9-4852	55148-55156		
PKS 1244-255	56024-56031		
GX 304-1	55281-55293		
	55417-55438		
	55539-55560		
	55684-55709		
	55805-55827		
	55932-55965		
	56069-56093		
NGC 5252	55559-55564		
IC 4329A	55390-55397		
MAXI J1409-619	55226-55233		
	55527-55548		
	55597-55604		
Circinus galaxy	55204-55212		
H1417-624	55148-55181		
Cir X-1	55323-55341		
	55584-55607		
	55747-55766		
	55901-55916		
SWIFT J1539.2-6227	54794-54805		
4U 1538-52*	55174-55182		
H1608-522	54951-54969		
	55644-55708		
	55738-55853		
IGR J16318-4848	54780-54807		

Continued on next page

Table – *Continued from previous page*

Source Name	12-50 keV Day Range (MJD)	50-100 keV Day Range (MJD)	100-300 keV Day Range (MJD)
4U 1630-472	55149-55169		
	55193-55235		
	55923-55929		
	56033-56086	56059-56086	
GX 340+0	54912-54985		
Her X-1	54692-54699		
	54720-54731		
	54754-54763		
	54788-54803		
	54825-54837		
	54860-54874		
	54932-54943		
	54966-54980		
	55000-55013		
	55036-55048		
	55071-55083		
	55105-55119		
	55141-55157		
	55176-55192		
	55212-55222		
	55246-55259		
	55281-55295		
	55316-55329		
	55351-55365		
	55388-55402		
	55423-55434		
	55457-55470		
	55493-55506		
	55526-55538		
	55562-55573		
	55598-55605		
	55630-55646		
	55665-55677		

Continued on next page

Table – *Continued from previous page*

Source Name	12-50 keV Day Range (MJD)	50-100 keV Day Range (MJD)	100-300 keV Day Range (MJD)
	55699-55711		
	55735-55747		
	55765-55784		
	55806-55818		
	55843-55851		
	55876-55886		
	55911-55923		
	55948-55958		
	55980-55993		
	56018-56027		
	56048-56059		
	56083-56096		
	56119-56128		
MAXI J1659-152	55467-55495		
GX 339-4	54895-54939	54890-54937	
	55218-55306	55212-55284	
4U 1702-429	56056-56089		
IGR J17091-3624	56081-56087		
GX 354-0	54699-54763		
	55212-55245		
	55373-55413		
	55485-55509		
	55803-55885		
GX 1+4	54999-55016		
	55103-55195		
	55315-55354		
	55364-55408		
	55510-55591	55519-55560	
	55696-55779	55699-55765	
IGR J17464-3213	54742-54757		
	55918-55944		
EXO 1745-248	55482-55506		
XTE J1752-223	55127-55219	55128-55217	55156-55181

Continued on next page

Table – *Continued from previous page*

Source Name	12-50 keV Day Range (MJD)	50-100 keV Day Range (MJD)	100-300 keV Day Range (MJD)
XTE J1810-189	54839-54853		
Ser X-1	54700-54709		
SWIFT J1842.5-1124	54699-54763		
SWIFT J1843.5-0343	55281-55289		
GS 1843+00	54893-54917		
SWIFT J1910.2-0546	56133-56148		
Aql X-1	54905-54918		
	55166-55245		
	55260-55272		
	55442-55453		
	55845-55889		
TXS 1920-211	56116-56142		
XTE J1946+274	55355-55407		
	55507-55566		
	55575-55586		
	55635-55688		
4U 1954+31	54768-54807		
PKS 1954-388	56125-56134		
EXO 2030+375	54737-54748		
	54830-54844		
	55059-55068		
	55101-55118		
	55200-55209		
	55289-55299		
	55426-55438		
	55517-55539		
	55610-55619		
	55748-55760		
	55841-55854		
	55888-55898		
	55979-55993		
	56072-56081		
PKS 2052-47	54756-54762		

Continued on next page

Table – *Continued from previous page*

Source Name	12-50 keV Day Range (MJD)	50-100 keV Day Range (MJD)	100-300 keV Day Range (MJD)
SAX J2103.5+4545	55480-55516		
GINGA 2138+56	54898-54918		
3C 454.3	55952-55961		
PKS 2255-282	55941-55948		

6.3.1 Comparison to GBM Flare Database

The transient search results can be compared to the GBM flare database, which is based on the BAT 15-50 keV data, as discussed in Sec 2.3.1. In the comparison, only flares lasting 5 days or longer in the flare database were considered. There were 280 transient events from 44 sources from the flare database that met this criteria. The large disparity in the number of transient events is predominately due to the periodic sources SMC X-1, LMC X-4, Her X-1, and EXO 2030+375, which account for > 100 of the missed detections. Both SMC X-1 and LMC X-4 are at very low declinations and thus are not occulted for much of a precession period resulting in large data gaps, which explains the four detections between them compared to the 72 detections in the flare database. There were 10 sources in the flare database that were not detected by the transient search. Of those 10 sources, only one source (X Per) was detected above 6σ above the median during the flaring period defined by the flare database.

Figs. 6.1 - 6.3 show examples of flaring activity detected by the transient search with the vertical lines marking the start and stop times for the event based on the transient search. Fig. 6.1 is the 4-year light curve for the cataclysmic variable GK Per. This flare was one of the faintest detected with an average flux of ~ 51 mCrab. The light curve for the recurrent black hole binary GX 339-4 is shown in Fig. 6.2 with two flares and significant emission above 50 keV, and Fig, 6.3 shows the light curve for XTE J1752-223, which is also a black

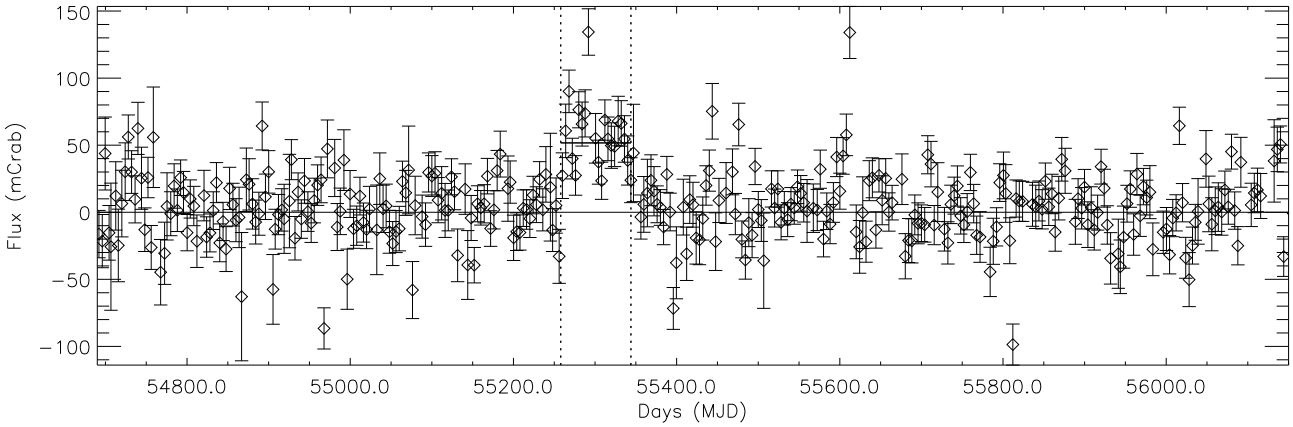

Figure 6.1: Flare from GK Per in the 12-50 keV energy band.

hole binary and the only source detected above 100 keV by the transient search.

6.3.2 GK Per

The source GK Per (Nova Persei 1901) is an intermediate polar system. Such systems consist of a white dwarf (WD) with a strong magnetic field accreting matter from typically a main-sequence companion star through Roche lobe overflow (Brunschweiger et al., 2009). The magnetic field directs the matter to the magnetic poles, and as the cool accreted matter slows down a shock is produced near the WD surface. The shock region is cooled by thermal bremsstrahlung radiation with a temperature

$$kT_e = \frac{3}{8}\frac{GM\mu m_p}{R} = 64\frac{M_1}{R_d}, \tag{6.1}$$

where R is the radius of the WD, μ the mean molecular mass of the accreting material, m_p the proton mass, $R_d = R/5 \times 10^8$ cm, and M_1 is the WD mass in solar mass units (Aizu , 1973; Fabian et al., 1976; Rothschild et al., 1981). If the WD mass and the radius fall in the region of Chanrasekhar mass-radius relation where $R_d \approx 1/M_1$ (Hamada & Salpeter, 1961), then

$$M_1 = \sqrt{\frac{kT_e}{64}}. \tag{6.2}$$

The spectrum can be fit to a blackbody model and the temperature from the fit used to estimate a lower limit for the WD mass (Suleimanov et al., 2005). A more complicated model is required to account for additional cooling methods (Frank, King, & Raine, 1992) and low energy absorption (Beardmore et al., 2000). The WD masses can be used in population studies of binary evolution (Brunschweiger et al., 2009). Fit results to BAT spectra give a mass estimate of $1.15 \pm 0.15 M_{\odot}$, which is consistent with results from Crampton et al. (1986) and Morales-Rueda et al. (2002) using alternative methods. Observations from GBM during the flaring period have an average flux of ~ 51 mCrab while BAT observation show an average 15-50 keV flux of ~ 37 flux. The difference is average fluxes is likely due to GBM covering energies down to 12 keV and a roughly 20 day gap of BAT data during the second half of the flare.

6.3.3 GX 339-4

The highly variable black hole binary GX 339-4 (Hynes et al., 2003) has been frequently observed by hard X-ray missions since the source was discovered (Markert et al., 1973). Since the launch of *CGRO* in 1991, emission above 100 keV has been detected from GX 339-4 by BATSE (Fishman et al., 1991), OSSE (Johnson et al., 1993), *RXTE* (Joinet et al., 2007; Del Santo et al., 2008), and *INTEGRAL* (Caballero-García et al., 2009; Cadolle Bel et al., 2011), with a marginal detection by GBM (Case et al., 2011). The brighter outburst in Fig. 6.2 was first seen on January 3, 2010 (MJD 55199) by *MAXI* (Yamaoka et al., 2010). When including the marginal detection, GBM observations from 12-300 keV are in good agreement with hard X-ray/soft γ-ray observations presented in Cadolle Bel et al. (2011). Broadband spectra from radio to soft γ-ray show GX 339-4 to have been in a hard spectral state during this period. In this state, the hard X-ray flux is high relative to the soft X-ray flux, and the spectrum can be modeled by a power law with a photon index ranging from

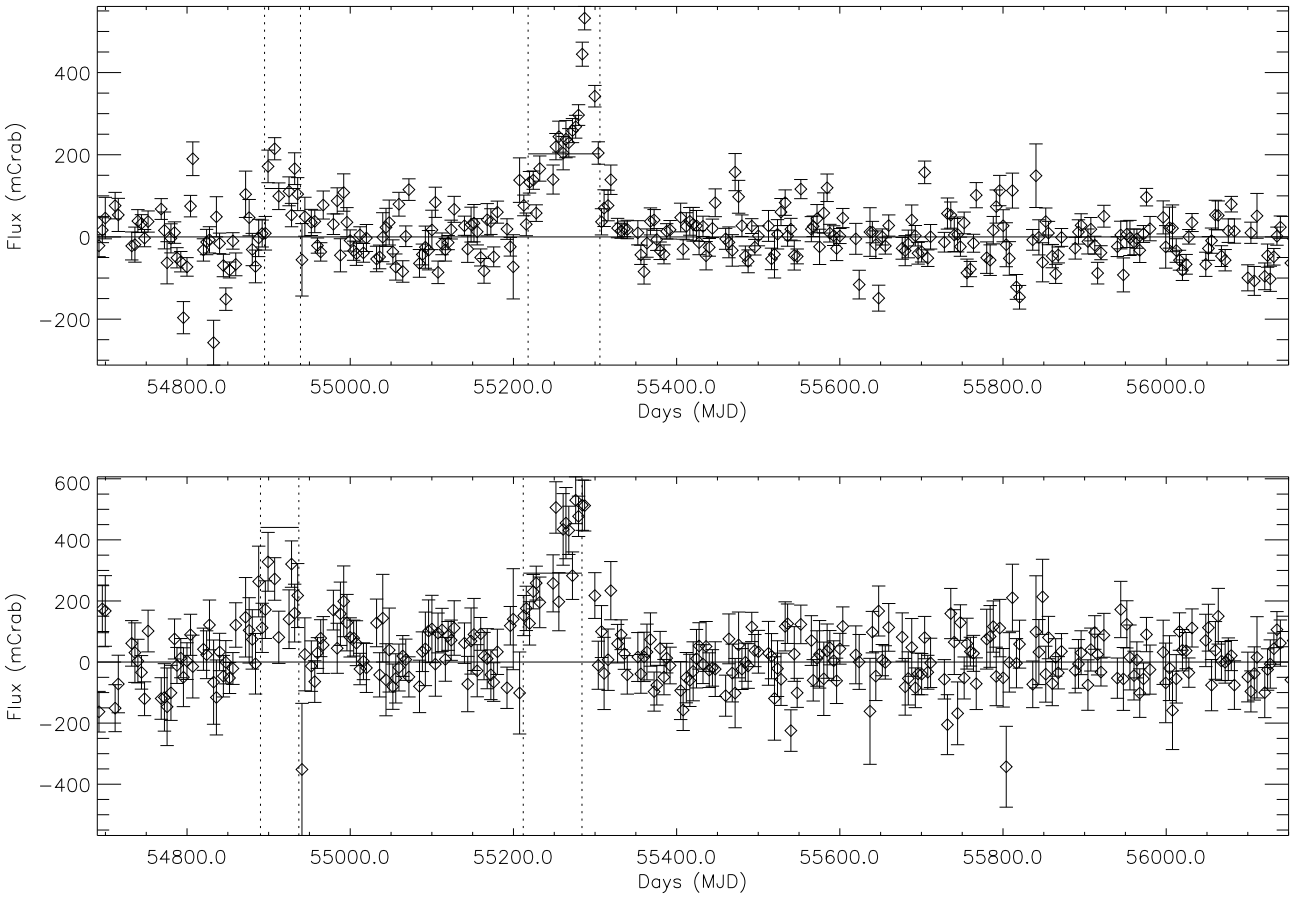

Figure 6.2: Flares from GX 339-4 in the: 12-50 keV band (*Top*) and 50-100 keV band (*Bottom*).

$\Gamma = 1.4 - 2.1$ and an exponential cutoff above 100 keV (Joinet et al., 2007), with the form

$$F(E) = NE^{-\Gamma}e^{-E/E_C}, \tag{6.3}$$

where F is the flux, E the photon energy, N is the normalization, Γ the photon index, and E_C the cutoff energy. The emission is predominately due to inverse Compton scattering of soft X-rays by the hot electron gas of the corona (Johnson et al., 1993; Cadolle Bel et al., 2011) or due to inverse Compton scattering from the base of a jet formed during the hard state (Markoff et al., 2005). Results from the corona and jet models diverge above the ~ 100 keV cutoff energy making high energy observations important in differentiating between

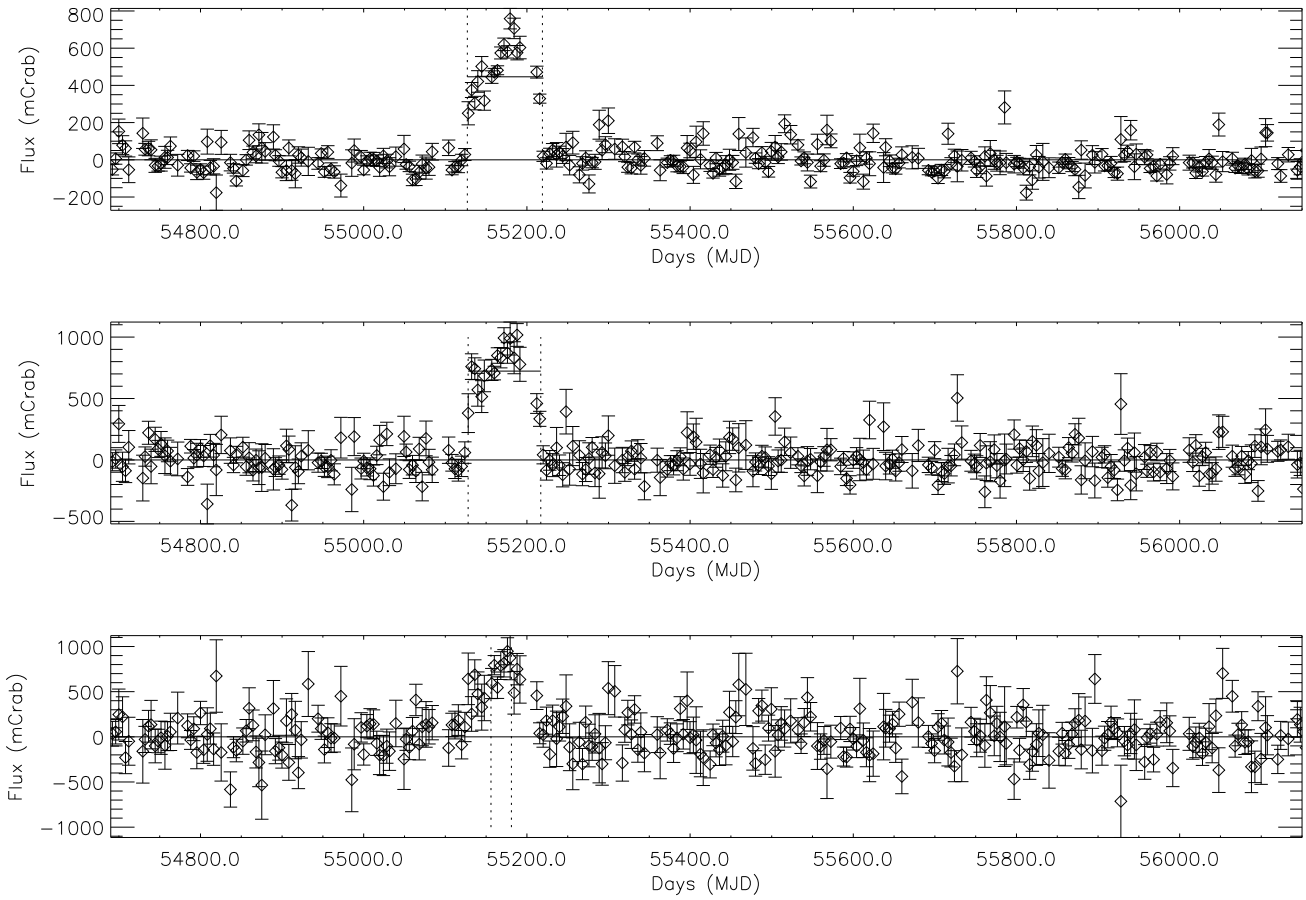

Figure 6.3: Flare from XTE J1752-223 in the: 12-50 keV band (*Top*), 50-100 keV band (*Middle*), and 100-300 keV band (*Bottom*).

the two models. Comparison of GBM observations spanning the duration of the flare are consistent with *INTEGRAL* observations (Cadolle Bel et al., 2011) between MJD 55259 and 55261. Cadolle Bel et al. (2011) report best fit parameters for a cutoff power law model with a photon index of $\Gamma = 1.69 \pm 0.04$ and a cutoff energy at $E_C = 328^{+94}_{-64}$ keV, which are consistent for black hole binaries in a hard spectral state.

6.3.4 XTE J1752-223

The black hole binary XTE J1752-223 (Shaposhnikov et al., 2010) was discovered in October 23, 2009 by *Swift*/BAT (Markwardt et al., 2009). GBM provides unique observations

covering the duration of the hard state. Because of solar avoidance constraints, *RXTE* was unable to observe for two months from MJD 55155 to 55215, and BAT was unable to observe for roughly a month (Shaposhnikov et al., 2010). These periods correspond to approximately the peak of the outburst in the hard X-rays. *RXTE* observations (Muños-Darias et al., 2010) shortly after the outburst began detected high energy emission above 100 keV from XTE J1752-223 with a high energy cutoff value consistent with those seen for outbursts from GX 339-4 (Motta et al., 2009; Muños-Darias et al., 2010).

Chapter 7
Conclusion

Because of the difficulty in focusing hard X-ray/soft γ-ray photons with traditional optics, alternative methods have been developed to observe sources in this energy range. One such approach is the Earth Occultation Technique (EOT) that was successfully applied to *CGRO*/BATSE (Harmon et al., 2004). These results motivated the use of the EOT with the *Fermi*/GBM since its launch in 2008 with multiple noteworthy results including: publicly available light curves for all sources, a catalog of high energy ($>$ 100 keV) sources (Case et al., 2011), a 3-year catalog of EOT results with source positions, fluxes, errors for all 209 sources in 4 broad energy bands (Wilson-Hodge et al., 2012), and detected variability of the Crab in the 15-100 keV energy range (Wilson-Hodge et al., 2011).

In addition to monitoring a catalog of predetermined sources, the imaging method Imaging with a Differential filter using the Earth Occultation Method (IDEOM) was developed with GBM to generate all-sky images to search for sources not in the GBM catalog. IDEOM was applied to $\sim$ 4 years of GBM CTIME data to produce all-sky broad band images in the 12-50 keV, 50-100 keV, and 100-300 keV energy ranges. Roughly 45 sources were identified through the IDEOM analysis, and 16 sources were added to the GBM catalog through cross-correlating features in images with sources in the *Swift*/BAT and *INTEGRAL* catalogs. Most of the calculated source positions were within $\sim 0.5^\circ$ of the known source position, which is near the minimum angular resolution as constrained by the Earth's atmosphere. No sources outside the GBM catalog were detected in the 100-300 keV band down to $\sim$ 20 mCrab suggesting that the discrepancies between the MSFC and JPL analyses are not due to

unaccounted-for sources and likely caused by inaccuracies in the EBOP background model.

Spectral analysis of the four persistent sources detected by GBM and LAT (NGC 1275, 3C 273, Cen A, and the Crab) was performed using GBM, COMPTEL (where available) and LAT data providing energy coverage from roughly 10 keV to 10 GeV. For NGC 1275, the extrapolation of the *Fermi*/LAT spectrum down to GBM energies shows results are consistent with those from the EOT. Also, models from von Montigny et al. (1997) and Reynoso et al. (2011) are in good agreement with presented results for 3C 273 and Cen A, respectively. The GBM model parameters for the Crab were extrapolated up to LAT energies and were shown to be in excellent agreement.

Also, a transient search algorithm was developed to determine times of flaring and outbursts from sources in the GBM catalog. The method was applied to 4 years of GBM EOT data searching the 12-50 keV, 50-100 keV, 100-300 keV, and 300-500 keV energy ranges. There were 168 transient events detected from 65 sources with seven events detected above 50 keV and one event detected above 100 keV (XTE J1752-223). The method has been shown the ability to detect outbursts with an average flux down to at least 50 mCrab. Also, GBM is not limited by solar constraints, unlike other instruments, and thus can provide important observations of transient events as shown in the case for XTE J1752-223. Finally, GBM's ability to observe above 100 keV allows for contributions in differentiating between the jet and corona models used in characterizing the hard spectral state in black hole binaries.

Bibliography

Abdo, A. A. et al. 2009, ApJ, 699, 31

Abdo, A. A. et al. 2010a, ApJ, 719, 1433

Abdo, A. A. et al. 2010b, ApJ, 708, 1254

Abdo, A. A. et al. 2011, Sci., 331, 739

Abraham, J., et al. 2009, arXiv 0906.2347

Aharonian, F. et al. 2009, ApJ, 695, L40

Aizu, K. 1973, Prog. Theoretical Phys., 49, 4

Atwood, W. B. et al. 2009, ApJ, 697, 1071

Barthelmy, S. et al. 2005, SSRv, 120, 143

Beardmore, A. P. et al. 2000, MNRAS, 315, 307

Beckmann, V. et al. 2011, A&A, 532, A70

National Institute of Standards and Technology 1998,http://www.nist.gov/pml/data/xcom/index.cfm

Bignami, G. F. et al. 1981, A&A, 93, 71

Bildsten, L. et al. 1997, Astrophysical Journal Supplement Series, 113, 367

Bowyer, S. et al. 1964, Science, 146, 912

Brunschweiger, J. et al. 2009, A&A, 496, 121

Caballero-García, M. D. et al. 2009, 692, 1339

Cadolle Bel, M. et al. 2011, A&A, 534, 119

Caroli, E. et al. 1987, Space Sci. Rev., 45, 349

Case, G. L. 2011, Astrophysical Journal, 729, 105

Chernyakova, M. et al. 2007, A&A, 465, 147

Collmar, W. et al. 2000, A&A, 465, 147

Cournoiser, T. J.-L. et al. 2003, A&A, 411. L343

Crampton, D. 1986, ApJ, 300, 788

Churazov, E. et al. 2003, ApJ, 590, 225

Davison, P. J.N. & Morrison, L. V. 1977, Monthly Notice of the Royal Astronomical Society, 178, 53

De Jager, O. C. et al. 1996, ApJ, 457, 253

Del Santo, M. et al. 2008, 390, 227

Eckert, D. & Paltani, S. 2009, A&A, 495, 415

Fabian, A. C. 1976, MNRAS, 175, 43

Fishman, G. J. et al. 1984, AIP Conference Proceedings, 115, 651

Fishman, G. et al. 1991, IAC Circ. 5237

Frank, J., King, A., & Raine, D. 1992 "Accretion Power in Astrophysics", 2nd edn (Cambridge University Press)

Giacconi, R. & Rossi, B. 1960, JGR, 65, 773

Grindlay, J. E. et al. "All-Sky X-Ray Observations in the Next Decade", 1998, 247

Hamada, T. & Salpeter, E. E. 1961, ApJ, 134, 683

Harmon, B. A. et al. 2002, ApJS, 138, 149

Harmon, B. A. et al. 2004, ApJS, 154, 585

Harrison et al. 2010, SPIE, 7732, 27

Hartman, R. C. et al. 1999, ApJS, 123, 79

Hynes, R. I. et al. 2003, ApJ, 583, 95

International Programme on Chemical Safety 2004, http://www.inchem.org/documents/icsc/icsc/eics1009.

Johnson, W. N. et al. 1993, A&AS, 97, 21

Johnson, W. N. et al. 1995, ApJ, 445, 182

Joinet, A. et al. 2007, 657, 400

Jones, T. W. et al. 1974, ApJ, 188, 353

Jourdain, E. & Roques, J. P. 2009, Astrophysical Journal, 704, 17

Kataoka, J. et al. 2010, ApJ, 715, 554

Kirsch, M. G. 2005, Proccedings SPIE, 5898, 22

Lightman, A. & Zdziarski, A. 1987, 319, 643

Linares, M., et al. 2012, Astrophysical Journal, 760, 133

Ling, J. C. et al. 2000 ApJS, 127,79

Ling, J. C. & Wheaton, W. A. 2003, ApJ 598, 334

Louisiana State University High Performance Computing 2012, http://www.hpc.lsu.edu/resources/hpc/system.php?system=Tezpur

Louisiana Optical Network Institute 2012, http://www.loni.org/systems/system.php?system=QueenBee

Mainardi, L. I. et al. 2010, A&A, 512, 57

Mannhnheim, K. 1993, Phys. Rev. D, 48, 6

Mannheim, K. & Biermann, P. L. 1992, 253, L21

Markert, T. H. et al. 1973, ApJ, 184, 67

Markoff, S. et al. 2005, ApJ, 635, 1203

Markwardt, C. B. et al. 2009, ATel, 2258

Meegan, C. et al. 2009, ApJ, 702, 791

Meyer, M. et al. 2010, Astronomy & Astrophysics, 523, 11

Migliari, S. et al. 2007, ApJ, 671, 706

Miyakai, S. 1996, PASJ, 48, 801

Morales-Rueda, L. et al. 2002, MNRAS, 329, 597

Motta, S. et al. 2009, MNRAS, 400, 1603

Muños-Darias, T. et al. 2010, MNRAS, 404, L94

Narayan, R. & Nityananda, R. 1986, Annual Review of Astronomy and Astrophysics, 24, 127

National Institute of Standards and Technology 1989, http://physics.nist.gov/PhysRefData/XrayMassCoef/ComTab/air.html

Nolan, P. L. et al. 2012, ApJS, 199, 31

Osako, C. Y. et al. 1994, ApJ, 435, 181

Pacciani, L. et al. 2009, A&A, 494, 49

Palmieri, T. M. 1975, Astrophysical Journal, 202, 494

Parsons, A. M. et al. 1998, Astrophysical Journal, 501, 608

Paizis, A. et al. 2005, A&A, 443, 559

Pottschmidt, K. et al. 2008, Proceedings of the 7th INTEGRAL Workshop, p.98

Primini, F. A. 1979, Nature, 278, 234

Primini, F. A. et al. 1981, ApJ, 243, L13

Reimer, O. et al. 2003, ApJ, 588, 155

Remillard, R. A. & McMlintock, J. E. 2006, Annual Review of Astrophysics, 44,49

Reynoso, M. M. et al. 2011, A&A, 531, A30

Rodi, J. C.et al. 2011, Fermi Symposium Proceedings - eConf C110509

Rothschild, R. E. et al. 1981, ApJ, 250, 723

Sanders, J. S. et al. 2005, MNRAS, 360, 133

Schönfelder, V. 1994, Astrophysical Journal Supplement Series, 92, 593

Schönfelder, V. et al. 2000, A&A, 143, 145S

Shaposhnikov, N. et al. 2010, ApJ, 723, 1817

Shaw, S. E. et al. 2004, A&A, 418, 1187

Soldi, S., Beckmann, V., and Turler, M. 2009, *Fermi* Symp. Proc. eConf C091122

Steinle, H. et al. 1998, A&A, 330, 97

Suleimanov, V. et al. 2005, A&A, 435, 191

Tarana et al. 2006, A&A, 448, 335

Toor, A. & Seward, F. D. 1974, AJ, 79, 995

Tueller, J. et al. 2008, Astrophysical Journal, 681, 113

Ulrich, M. et al. 1997, Annual Review of Astrophysics, 35, 445

U.S. Standard Atmosphere, 1976, U.S. Committee on Extension to the Standard Atmosphere. 1976, U.S. Standard Atmosphere, NOAA-S/T 76-1562 (Washington, DC: U.S. Govt Printing)

von Montigny, C. et al. 1997, ApJ, 483, 161

von Montigny, C. et al. 1995, ApJ, 440, 525

Watts, A. 2012, Annual Review of Astrophysics, 50, 609

Weisskopf, M. C. et al. 2010, Astrophysical Journal, 713, 912

Westmore, M. J. 2002, Ph.D. Thesis, Dept. of Physics & Astronomy, University of Southhampton, UK

Wheaton, W. A. 1996, A&AS, 120, 545

White, N. E. & Peacock, A. 1988, Societ Astronomica Italiana, Memorie, 59, 7

Wilson-Hodge, C. A. et al. 2011, Astrophysical Journal Letters, 727, L40

Wilson-Hodge, C. A. et al. 2012, Astrophysical Journal Supplement Series, 201, 33

Worrall, D. M. et al. 1979, ApJ, 232, 683

Yamaoka, K. et al. 2010, ATel, 2380

Zhang, S. N. et al. 1993, Nature, 366, 245

Zhang, S. N. et al. 1994, IEEE Transactions of Nuc. Sci, 41, 1313

Zhang, S. N. et al. 1995, Exper. Astro., 6, 57

Chapter A
Reprint Permission for Fig. 2.6

Request - 01/25/2013

To Whom It May Concern,

I would like permission to use Figure 4 from Three Years of Fermi GBM Earth Occultation Monitoring: Observations of Hard X-ray/Soft Gamma-ray Sources, citation ApJS 2012, 201, 33, for my dissertation. I am one of the original co-authors.

Thanks,

James Rodi

Permission - 01/28/2013

Dear James Rodi

Thank you very much for your permissions enquiry relating to material published previously in the journals of the American Astronomical Society.

On behalf of AAS, we are pleased to grant the necessary permission for your use of this material and we ask that the Society is acknowledged through the wording: "Reproduced by permission of the AAS". We note that you are one of the original authors of this material.

Thank you again for your interest in the AAS journals.

Yours sincerely

Jill Membrey

Managing Editor, Copyright and Permissions

Chapter B
Reprint Permission for Fig. 3.13

Request - 01/31/2013

Dear Dr. Meegan,

I would like to use a figure from "The Fermi Gamma-Ray Burst Monitor" paper from ApJ 2009, 702, 791 in my PhD. dissertation on hard X-ray/soft gamma-ray imaging with GBM. ApJ requires that I get permission from one of the authors. I would like to use Fig 12 showing the angular dependence of the NaI detector effective area. May I have your permission to use that figure?

Thanks,
James Rodi

Permission - 01/28/2013

Dear James,

You have my permission to use this figure, as well as any others that you wish. Good luck with your dissertation.

Best regards,
Charles Meegan

Permission - 02/08/2013

Dear Dr Rodi

Thank you very much for your permissions enquiry relating to material published previously in the journals of the American Astronomical Society.

On behalf of AAS, we are pleased to grant the necessary permission for your use of this material and we ask that the Society is acknowledged through the wording: "Reproduced by permission of the AAS". We note that you have already obtained the approval of the original authors for your planned reuse of their material.

Thank you again for your interest in the AAS journals.

Yours sincerely

Jill Membrey
Managing Editor, Copyright and Permissions

Vita

James Craig Rodi was born in Baton Rouge, Louisiana in April 1984 where he was also raised. In 2002 he began his undergraduate studies at Louisiana State University, earning a Bachelor of Science degree in 2006. He then began his graduate career in Fall 2006 at Louisiana State University and plans to receive his Doctor of Philosophy in Physics & Astronomy in 2013 under the supervision of Dr. Michael L. Cherry.